PERFORMANCE EVALUATION AND SIMULATION OF A COMPOUND PARABOLIC CONCENTRATOR (CPC) TROUGH SOLAR THERMAL POWER PLANT IN PUERTO RICO UNDER SOLAR TRANSIENT CONDITIONS

by

Luisa I. Feliciano-Cruz

A thesis submitted in partial fulfillment
of the requirements for the degree of

MASTER OF SCIENCE

in

ELECTRICAL ENGINEERING

University of Puerto Rico
Mayagüez Campus

2010

Approved by:

Lionel Orama-Exclusa, Ph.D. Member, Graduate Committee	Date
Gustavo Gutiérrez, Ph.D. Member, Graduate Committee	Date
Eduardo I. Ortiz-Rivera, Ph.D. President, Graduate Committee	Date
Noel Artiles-León, Ph.D. Representative of Graduate Studies	Date
Hamed Parsiani, Ph.D. Department Chairperson	Date

ABSTRACT

The increasing fossil fuel costs as well as the need to move in a somewhat sustainable future has led the world in a quest for exploiting the free and naturally available energy from the Sun to produce electric power, and Puerto Rico is no exception. This thesis proposes the design of a simulation model for the analysis and performance evaluation of a Solar Thermal Power Plant in Puerto Rico and suggests the use of the Compound Parabolic Concentrator as the solar collector of choice. Optical and thermal analysis of such collectors will be made using local solar radiation data for determining the viability of this proposed project in terms of the electric power produced and its cost.

RESUMEN

El incremento en los costos de combustible, así como la necesidad de moverse hacia un futuro sustentable, ha encaminado al mundo en la búsqueda de poder explotar la energía gratis del Sol para producir electricidad y Puerto Rico no es la excepción. Este trabajo de tesis propone el diseño de un modelo de simulación para el análisis y evaluación de la operación de una Planta Solar de Potencia Eléctrica en Puerto Rico y sugiere el uso del Concentrador Compuesto Parabólico como colector. Se realizarán análisis óptico y termal a estos colectores utilizando data local de irradiación solar para determinar la viabilidad del proyecto propuesto en términos de su producción eléctrica y su costo.

ACKNOWLEDGEMENTS

Above all, I would like to thank God for giving me the opportunity of being here, at this precise time and moment, and allowing me to be so happy with my life ...

I want to sincerely thank Dr. Eduardo I. Ortiz Rivera, president of my Graduate Committee, for giving me the opportunity of working under his guidance. It has been my dream, for several years, to be able to contribute in the renewable energy field for the benefit of Puerto Rico. I also want to express my gratitude to Dr. Gustavo Gutiérrez for sharing his vast knowledge with me and to Dr. Lionel Orama Exclusa for his support throughout the years and for being an excellent role model of a human being. And last, but certainly not least, I want to thank Dr. Fernando Plá. This work is today a reality, thanks to his unconditional help and guidance. I will be forever grateful.

I would also like to acknowledge the constructive criticism and helpful suggestions of Dr. Noel Artiles León, Representative of Graduate Studies, during the exam, which provided noteworthy improvements to the thesis document.

I want to thank my fellow graduate friends for their good wishes and for always being there as an encouraging force: Carla Joan, Joy and Arlene. I thank you from the bottom of my heart!

I want to dedicate this work to my parents Benita & Arquelio, to my brothers Junior & Victor, and to those who are no longer with me: To my brother Renis & my sister Liz who have been my guardian angels and my inspiration throughout the years. I love you, guys!

I also want to dedicate this work to my new family! To my precious daughters: Arianna Isabelle & Gianna Nicole, and to Ricky, I love you, baby!

Contents

List of Tables

List of Figures

Chapter 1

INTRODUCTION

1.1 Motivation

The increasing energy demand, as well as the dependency on depleting fossil fuels, and the need to address global warming has inevitably triggered the need to seek alternate methods of electric power generation. There are many renewable energy systems in use that harness the energy of the sun as a means to produce electricity. The most widely used are photovoltaic panels (PV), which convert the sun's radiation energy into electricity. The ones that are not so common rely on the fact that the energy coming from the sun can be collected and concentrated by imaging concentrators to heat up a working fluid to produce steam, which is used to propel a steam turbine or motor. The movement in turn, acts as the mechanical power input to a generator. These renewable energy systems are referred to as *Solar Thermal Power Plants* (STPP).

Several STPPs were developed and implemented as prototypes by local utilities in different parts of the United States during the 80's. STPPs have not been exploited to their full potential due to the fact that they are not commercially available and

therefore, have to be custom built. Because of this, production costs have remained somewhat high, forcing STTPs to be constructed in the MW utility range. Most STPPs currently employ parabolic-shaped mirror concentrator troughs catalogued as imaging collectors which attain very high operating temperatures, in the range of $350 - 400\,^{\circ}\mathrm{C}$. Although this is desirable, their main disadvantage lies in the fact that because of their imaging nature, they tend to concentrate solar rays in a single focal point. Thus, continuous tracking of the sun is necessary for adequate operation. System efficiency declines fast with small deviations in the tracking angle so, sophisticated and costly control systems are required. Another disadvantage is that they can only concentrate direct (or beam) solar radiation. Radiation data, which is usually measured as global (or total), needs to be manipulated in order to separate its direct and diffuse components for accurately predicting system adequacy and performance. *Compound Parabolic Concentrator* (CPC) troughs, on the other hand, do not need continuous tracking of the sun and can concentrate both direct and diffuse radiation due to their non-imaging properties. They can be installed in a fixed position, giving it reliability and sturdiness, while maintaining high concentration ratios, acceptable efficiency and a considerable reduction in costs.

This work focuses on the various aspects regarding the design, operation, optimization and viability of a CPC trough project of this nature in Puerto Rico, taking into account local solar radiation data. This data will be converted into a solar insolation map by means of numerical analysis and computer software, estimating solar radiation anywhere in Puerto Rico. This in turn will provide information on where would a STPP (or any other solar system, such as PV) be more effectively constructed and operated in terms of solar radiation. Therefore, an innovative renewable energy system is proposed for Puerto Rico with the main objective being: the determination of the electricity that

can be produced and its cost per kilowatt-hour.

1.2 Objectives

During the development of this work, the following specific objectives were considered:

- Analyze solar radiation data for the development of a solar insolation map for Puerto Rico.
- Study the different compound parabolic concentrator (CPC) configurations according to optics and geometry.
- Identify the main components in a STPP and analyze the most appropriate ones in terms of the factors mentioned above, such as: thermal and optical properties, materials, efficiency, cost, etc.
- Construct a model for simulation of the proposed system that can provide a means for determining the system's viability in terms of the electric power that can be produced.
- Employ the levelized electricity cost analysis for determining the system cost per kilowatt-hour.
- Analyze and discuss the model's results.

The work is divided in three phases. *Phase I:* The creation of a Solar Insolation Map for Puerto Rico. *Phase II:* Theoretical approach to a STPP design. *Phase III:* Analysis of the viability of a STPP in Puerto Rico through a simulation model, taking solar transient conditions into account.

Phase I: Creation of a Solar Insolation Map for Puerto Rico: Using available or processed radiation data, MATLAB® and Microsoft Excel® to produce a solar radiation surface delimited by the latitudes and longitudes of Puerto Rico. This can aid in determining the most appropriate areas where a STPP could be located.

Phase II: Theoretical approach to a STPP design: Taking into consideration aspects such as solar and materials engineering, optics and heat & mass transfer basics and fluid mechanics. This analysis was conducted in Microsoft Excel® and MATLAB® to provide the opportunity of altering or changing system components, or doing sensitivity analysis.

Phase III: Analysis of the viability of a STPP in Puerto Rico through a simulation model, taking into consideration solar transient conditions. The model will include modules for the optical and thermal characteristics of the solar collection system, heat transfer mechanisms and power block.

1.3 Chapter Summary

This thesis consists of 9 chapters which are briefly summarized below:

Chapter 1: Serves as an introduction to the investigation.

Chapter 2: Presents an overview of the solar energy available, as well as means of: measuring, analyzing and estimating it. It also discusses important aspects in solar energy such as: variability and uncertainty.

Chapter 3: Provides a means of presenting the solar resource available in Puerto Rico as well as a map of the available resource.

Chapter 4: Discusses in essence what a Solar Thermal Power Plant is, and which are its main components.

Chapter 5: Depicts the CPC collector, its geometry and its optical analysis.

Chapter 6: Presents all the relevant energy balance calculations necessary for analyzing the technical feasibility of the system.

Chapter 7: Discusses the proposed STPP for Puerto Rico.

Chapter 8: Presents a simulation model for proving the viability of a STPP during solar transient conditions and its relation to the electric power produced, as well as an estimate of system cost.

Chapter 9: Makes final remarks regarding the study and proposes several ideas for future work.

Chapter 2

SOLAR RESOURCE OVERVIEW

2.1 Introduction

Aside from supporting virtually all life on Earth, the Sun is the energy source that drives the climate and weather patterns on the entire planet. The heat and light that reaches Earth from the Sun account for over 99.9 percent of the available renewable energy used today, including solar-based resources such as: wind and wave power, hydroelectricity and biomass [5].

The sun is an average-sized star of average age and brightness. To astronomers, it is a main sequence star of spectral class G with an apparent surface temperature of around 6,000K. It is presumed that at the center of the sun, hydrogen nuclei are combining in a thermonuclear fusion process to form helium nuclei. Most of the electromagnetic radiation reaching the earth emanates from the photosphere, an outer shell of hot dense gas. Further outside from the sun, beyond the photosphere are the chromosphere and the corona, as shown in Figure 2.1. These regions are characterized by low-density gases, higher temperatures, and variations in energy.

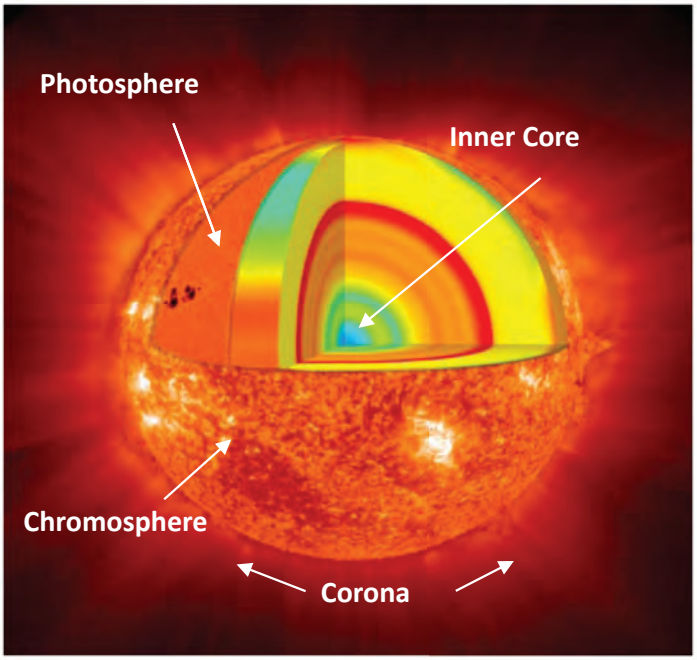

Figure 2.1: Layers of the sun (NASA)

To better understand the solar resource as a means of harvesting it for energy production, several of the Sun's characteristics must be studied, such as: geometry, the energy available (radiation), resource estimation and variability. Acknowledging these characteristics provide a basis for understanding, using and predicting solar radiation data [10].

2.2 Solar Geometry

There are several geometrical relationships between the Sun and the plane where solar radiation is of interest. The most relevant are:

- n, day of the year.
- Latitude φ, angular location north or south of the equator, being north positive.

- Declination δ, angular position of the sun at solar noon with respect to the equator's plane, being north positive.

$$\delta = 23.45 \sin \frac{360(284 + n)}{365} \tag{2.1}$$

- Hour angle ω, angular displacement of the Sun east or west of the local meridian at 15 °C. per hour, being positive in the morning.

- Zenith angle θ_z, angle between the vertical and the line to the Sun or angle of incidence of beam radiation on a horizontal surface.

$$\theta_z = \cos^{-1} \left[\cos \varphi \cos \delta \cos \omega + \sin \varphi \sin \delta\right] \tag{2.2}$$

- Solar altitude angle α_s, angle between the horizontal and the line to the Sun.

$$\alpha_s = \sin^{-1} \left[\cos \varphi \cos \delta \cos \omega + \sin \varphi \sin \delta\right] \tag{2.3}$$

- Solar azimuth angle γ_s, angular displacement from south of the projection of beam radiation on the horizontal plane, being west of south, positive.

$$\gamma_{\mathrm{s}} = sign(\omega) \left| \cos^{-1} \left[\frac{\cos \theta_z \sin \varphi - \sin \delta}{\sin \theta_z \cos \varphi} \right] \right| \tag{2.4}$$

Some of these are shown in Figure 2.2.

The energy received from the Sun can be measured just outside the atmosphere or on a plane at Earth's surface. The solar constant is the amount of power that the Sun deposits per unit area exposed to sunlight and is equal to approximately 1,370

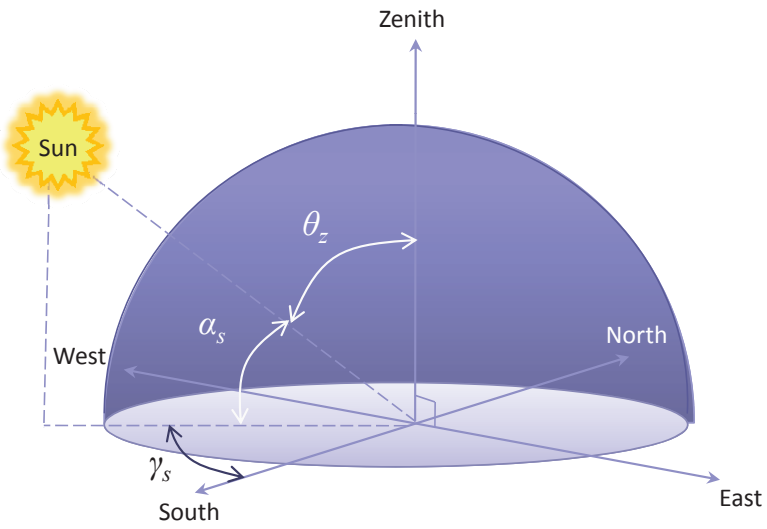

Figure 2.2: Solar geometry angle relationships

W/m^2 just outside Earth's atmosphere. Sunlight on Earth's surface is attenuated by the atmosphere to around 1,000 W/m^2 in clear sky conditions when the Sun is near the zenith. The extraterrestrial radiation, however, is the one that would be received in the absence of Earth's atmosphere [10].

On Earth's surface, radiation can be categorized as being beam, diffuse or global. Beam or direct radiation refers to the radiation received from the Sun without having been scattered by the atmosphere. Diffuse radiation is the one whose direction has been changed by scattering in the atmosphere due to clouds, water vapor, trees, particles, or other objects. Global or total radiation is the sum of these two.

2.3 Available Solar Energy

2.3.1 Solar Measurements

It is important to recognize that there are two common methods which characterize solar radiation: the solar radiance (radiation), and solar insolation. Solar radiation is an instantaneous power density in units of kW/m^2. The solar radiance varies throughout the day from 0 kW/m^2 at night to a maximum of about 1 kW/m^2. The solar radiance is strongly dependant on location and local weather. Solar radiance measurements consist of global radiation measurements taken periodically throughout the day. The measurements are taken using either a pyranometer, which is an instrument capable of measuring global radiation (See Figure 2.3), or a pyrheliometer, which measures beam radiation.

Figure 2.3: Measuring station located in Isabela, P.R.

Solar insolation, however, is the most commonly measured solar data. The solar insolation is the total amount of solar energy received at a particular location during a specified time period, in kWh/m^2 day. While the units of solar insolation and solar irradiance are both a power density, solar insolation is different than the solar irradiance as the solar insolation is the instantaneous solar irradiance averaged over a given

time period. Solar insolation data is commonly used for simple system design while solar radiance is used in more complicated systems to calculate its performance at each point in the day. Solar insolation can also be expressed in units of MJ/m^2 per year [10].

As was stated before, radiation data is usually measured with pyranometers capturing the global insolation. Several models have been developed to separate the beam and diffuse components of global insolation. The one adopted for the purpose of this investigation is the one presented in *Solar Engineering of Thermal Processes* by Duffie [10].

These calculations are often done using the ratio of monthly (measured) available radiation $\overline{H}$ to the theoretically possible (monthly extraterrestrial radiation) $\overline{H}_0$. This ratio is known as $\overline{K}_T$, or the average clearness index.

$$\overline{K}_T = \frac{\overline{H}}{\overline{H}_0} \tag{2.5}$$

The monthly extraterrestrial radiation is calculated as follows:

$$\overline{H}_0 = \frac{24(3600)G_{SC}}{\pi} \times \left(1 + 0.033\cos\frac{360n}{365}\right) \times \left(\cos\varphi\cos\delta\sin\omega_s + \frac{\pi\omega_s}{180}\sin\varphi\sin\delta\right) \tag{2.6}$$

where G_{SC} is the solar constant, n is the average day of the month, φ is the latitude, δ is the declination angle and ω_s is the sunset hour angle. After calculating $\overline{K}_T$, the diffuse and beam components can be calculated according to the average diffuse fraction given by:

$$\frac{\overline{H}_d}{\overline{H}} = 1.311 - 3.022\overline{K}_T + 3.42\overline{K}_T^2 - 1.821\overline{K}_T^3 for \omega_s > 81.4^\circ \tag{2.7}$$

where $\bar{H}_d$ is the monthly average daily diffuse radiation calculated by:

$$\overline{H}_d = \overline{H}(1.311 - 3.022\overline{K}_T + 3.42\overline{K}_T^2 - 1.821\overline{K}_T^3) \tag{2.8}$$

Thus, the monthly average daily beam radiation is:

$$\overline{H}_b = \overline{H} - \overline{H}_d \tag{2.9}$$

2.3.2 Resource Estimation

There have been several proposed methodologies for estimating solar radiation in the past. These take into account factors such as: hours of bright sunshine, hours of cloudiness, atmospheric attenuation of solar radiation by scattering or absorption, average clear-sky daily radiation and empirical constants dependent on location, to name a few. Under partly cloudy skies, due to the random and unknown location of the clouds, no model can accurately estimate the solar radiation incident on the earth's surface at any given time and location. These models, far from being useful, provide means for ambiguity according to some experts due to the fact that sunshine or cloudiness data are usually based on visual observations and there is uncertainty as to what constitutes a partly or mostly cloudy day [11].

One of the most used methods for estimating solar radiation is the meteorological-statistical (METSTAT) solar radiation model developed by the National Solar Radiation Database (NSRDB) [11]. It is used to estimate solar radiation when measured data is not available, reproducing the statistical and stochastic characteristics of multi year solar radiation data sets. This sacrifices accuracy for specific hours so, modeled values for individual hours may differ greatly from measured values if they had been

made. According to NSRDB, it is important that simulated data sets accurately represent the following statistical and stochastic characteristics of measured data: monthly moments (such as: mean, variance, skewness, kurtosis), monthly cumulative frequency distributions (cfds), diurnal and seasonal patterns, hourly and daily autocorrelations, cross-correlations between elements (global horizontal, diffuse horizontal, direct normal) and persistence.

Several features incorporated in the METSTAT model are: hourly calculations using hourly total and opaque cloud cover, hourly precipitable water vapor, daily aerosol optical depth, and daily albedo input data. Figure 2.4 is a representation of the NSRDB algorithms.

These produce representative diurnal and seasonal patterns, daily autocorrelations, and persistence. Placing the statistical algorithms between the input data and the deterministic algorithms leads to proper cross-correlations between the direct normal, diffuse horizontal and global horizontal components. Even though these methods are available for resource estimation, the best estimation that can be done is using available measured data from a location near the point of interest.

2.3.3 Uncertainty and Variability of Solar Data

Solar variations are changes in the amount of radiant energy emitted by the Sun. These variations have been typically attributed to two main factors: the eleven-year solar cycle and the Earth's atmosphere [12]. The total solar irradiance (TSI) is the amount of solar radiative energy impinging on the Earth's upper atmosphere. It is observed to vary in phase with the solar cycle, with yearly averages going from 1365.5 W/m^2 at solar minimum, up to of 1366.6 at solar maximum, with fluctuations about

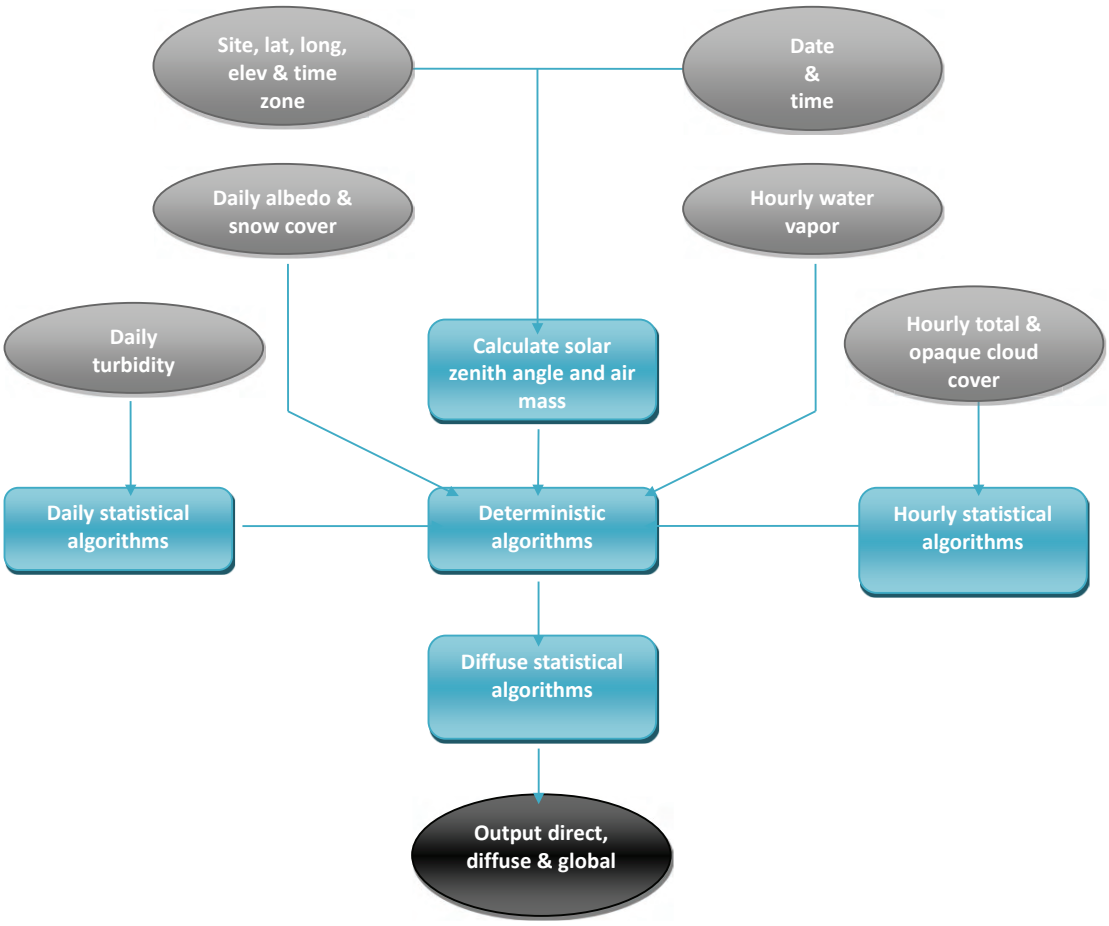

Figure 2.4: NSRDB algorithm for solar resource estimation(NSRDB)

the means of about +/- 1 W/m^2 on timescales of a few days. Variation at the 0.1% level is far too small to affect Earth's climate, but it is worth keeping in mind that continuous reliable measurements of the TSI are only available since 1978; the minimum and maximum levels of solar activity have remained roughly the same from then until now [11]. The eleven-year solar cycle is a fundamental aspect of the sun's behavior and is associated with variations in total output and activity.

Solar variability also occurs due to: changes in extraterrestrial radiation, atmospheric scattering (by air, water and dust) or atmospheric absorption (by ozone, water and carbon dioxide). There is some evidence that sunshine at the Earth's surface has been decreasing during the last 50 years possibly due to an increase in atmospheric pollution. The atmosphere causes a reduction of the extraterrestrial solar input by about 30 percent on a very clear day to nearly 90 percent on a very cloudy day [5]. Figure 2.5 gives an indication of the absorption and scattering caused by different components of the atmosphere.

As with the use of any measuring device, there is always a level of uncertainty as to whether the data being measured can be considered accurate. The most significant measurement errors with pyranometers and pyrheliometers are associated with the properties of these instruments, their calibration, and their data acquisition systems. Errors introduced by the instruments include: deviations from cosine law response to incident radiation, ambient temperature effects on response to radiation, nonlinear response to incident radiation, non-uniform response across the solar spectrum and errors associated with the use of shadow bands for measuring diffuse radiation. Errors introduced by calibration include: uncertainty in the definition of the international scale of solar radiation, errors in the transfer of the World Radiometric Reference to the

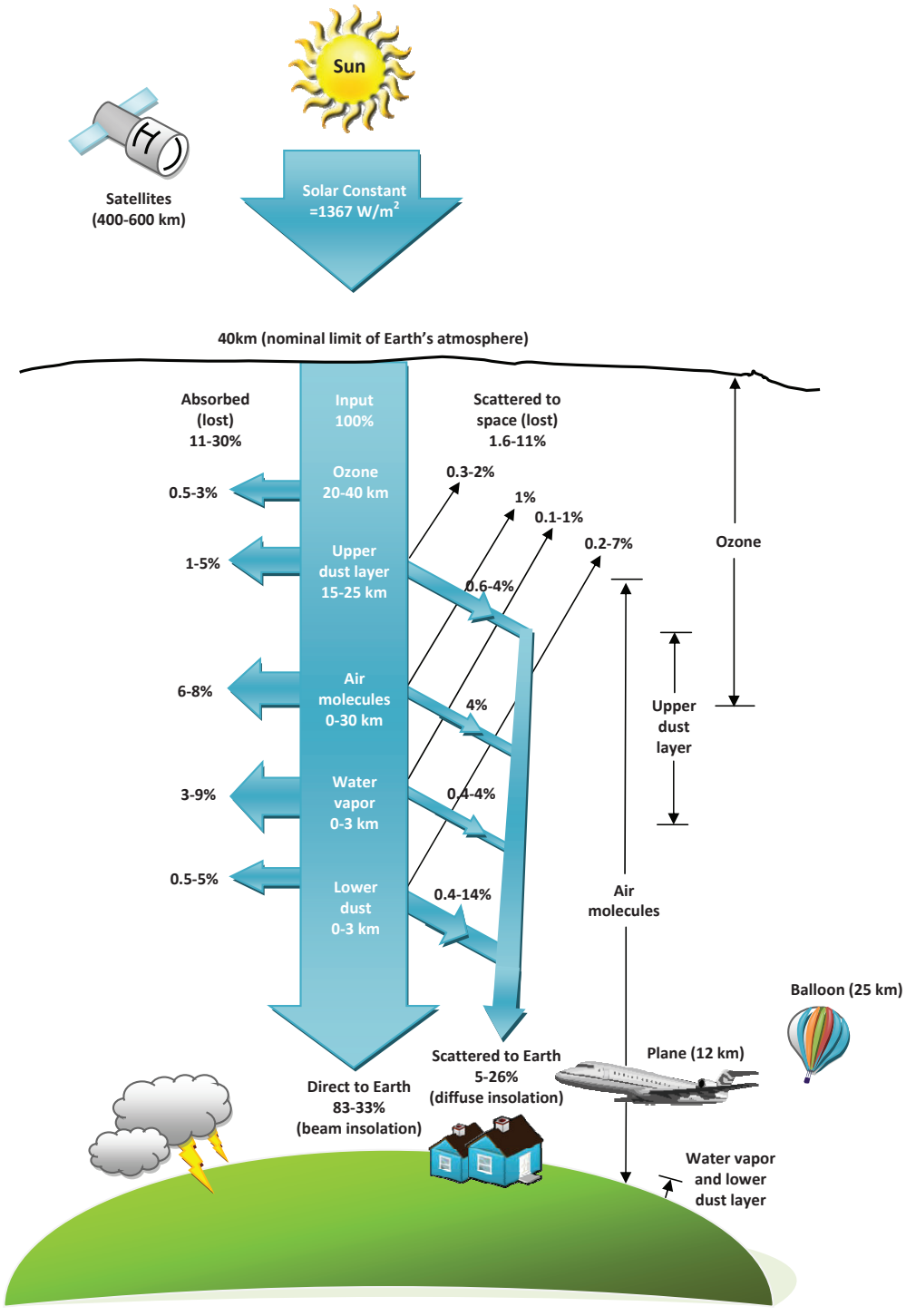

Figure 2.5: Atmospheric scattering and absorption, redrawn from [5]

secondary reference instruments and errors in the calibration of individual instruments. The results of the work of Myers, Emery, and Stoffel [11] yielded the following levels of uncertainty: global horizontal 5%, direct normal 3% and diffuse horizontal 7%.

Chapter 3

CLIMATE AND SOLAR RESOURCE IN PUERTO RICO

3.1 Climate in Puerto Rico

Puerto Rico is an island in the Caribbean Sea bounded by latitudes 17.9 °N to 18.5 °N, and by longitudes 65.6 °W to 67.25 °W. Although small, measuring 110 by 37 miles, Puerto Rico is topographically diverse [13]. It is divided into three major regions: the central mountainous region (including the Cordillera Central, Sierra de Luquillo Mountains, Sierra de Cayey and Sierra Bermeja), the coastal plains, and a karst region to the north. Temperatures are moderate all year long, ranging from 21 to 32 °C (70 to 90 °F). The rainy season extends from April to November [14].

Aside from high radiation levels, there is another factor that plays an important role in STPP system operation and siting: Climate. Acording to the The Köppen Climate Classification System, Puerto Rico falls into the tropical A climate type with three specific seasonal characteristics of precipitation: f, m and w.

The Köppen Climate Classification System is the most widely used for classifying the world's climates and was devised by the Russian-German climatologist Wladimir Köppen. It divides the Earth's surface into climatic regions that generally coincide with world patterns of vegetation and soils [6, 15]. It recognizes five major climate types based on the annual and monthly averages of temperature and precipitation. Each type is designated by a capital letter.

Region A: Equatorial, Moist Tropical Climates are known for their high temperatures year-round and for their large amount of year-round rain.

Region B: Dry Climates are characterized by little rain and a huge daily temperature range.

Region C: Humid Middle Latitude Climates have warm, dry summers and cool, wet winters.

Region D: Continental Climates can be found in the interior regions of large land masses. Total precipitation is not very high and seasonal temperatures vary widely.

Region E: Cold Climates are part of areas where permanent ice and tundra are always present. Only about four months of the year have above freezing temperatures.

Further subgroups are designated by a second letter distinguishing specific seasonal precipitation characteristics.

Precipitation W: Arid or desert.

Precipitation S: Semiarid or steppe.

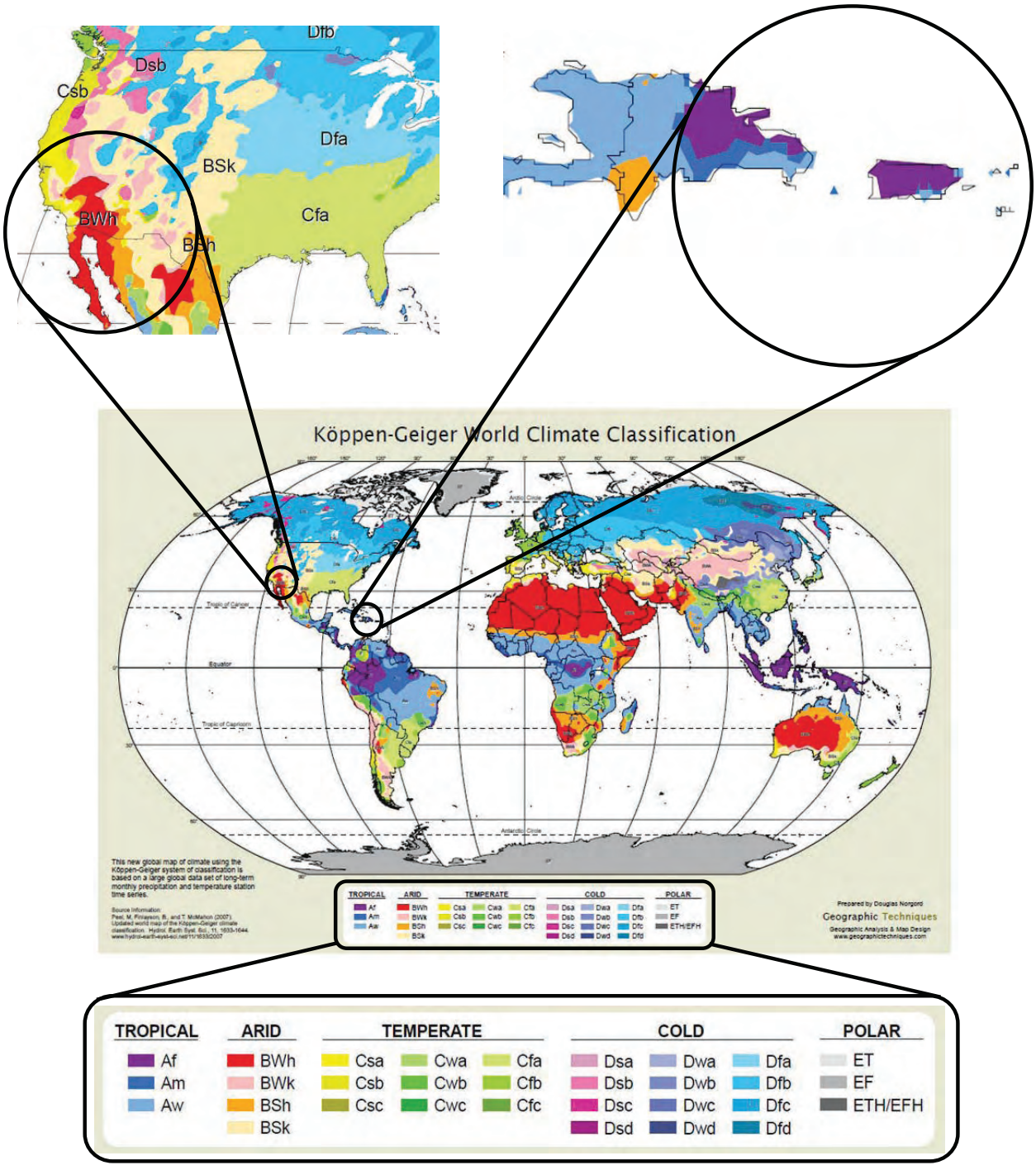

Figure 3.1: The Köppen-Geiger Climate Classification [6]. Puerto Rico and California comparison

Precipitation f: Moist with adequate precipitation in all months and no dry season. This letter usually accompanies the A, C, and D climates.

Precipitation m: Rainforest climate in spite of short, dry season in monsoon type cycle. This letter only applies to A climates.

Precipitation s: There is a dry season in the summer of the respective hemisphere.

Precipitation w: There is a dry season in the winter of the respective hemisphere.

To further denote variations in climate, a third letter was added to the system to account for temperature.

Temperature a: Hot summer where the warmest month is over 22 °C (72 °F). These can be found in C and D climates.

Temperature b: Warm summer with the warmest month below 22 °C (72 °F). These can also be found in C and D climates.

Temperature c: Cool summer with less than four months over 10 °C (50 °F) in the C and D climates.

Temperature d: Cold winter with the coldest month below −38 °C (−36 °F) in the D climate only.

Temperature h: Hot-arid with a mean annual temperature over 18 °C (64 °F) in B climates only.

Temperature k: Cold-arid with a mean annual temperature under 18 °C (64 °F) in B climates only.

Temperature F: Polar frost where all twelve months have average temperatures below 0 °C (32 °F).

Temperature T: Polar tundra where the warmest month has an average temperature between 0 °C (32 °F) and 10 °C (50 °F).

As can be observed in figure 3.1, Puerto Rico gathers three different subgroups within the Moist Tropical Climate type zone, namely f, m and w; meaning that most of it is an area with adequate precipitation in all months and no dry season, with some smaller areas where there are short dry periods, usually in the winter.

By analyzing the data collected in terms of radiation, temperature, and precipitation, it can be said that the climate in Puerto Rico is well represented by the Köppen System.

3.2 Data Availability

Solar data was gathered from four sources which account for 16 different sites in Puerto Rico. The main data source was obtained from the previously published work of A.M. López and K.G. Soderstrom [16]. This data collection project was conducted by the Center for Energy and Environment Research (CEER) in the University of Puerto Rico at Mayagüez and supported in part by the U.S. Department of Energy (DOE). The data was measured with a pyranometer on a horizontal plane between 1976 and 1981 for the municipalities of: Mayagüez, San Juan, Ponce, Cabo Rojo, Cataño and Manatí. This data is presented in Table 3.1.

Radiation data was also obtained through the U.S. Department of Agriculture Forest Service, Institute of Tropical Forestry in San Juan, P.R. This project conducted by C.B. Briscoe [17] aimed at studying weather patterns in and near the Luquillo Mountains of Puerto Rico, better known as El Yunque Rainforest. Thirteen sites were selected to be

studied and data was collected regarding temperature, humidity, wind, and rain. Solar radiation data was measured in only three of these sites: Fajardo, Río Grande and Gurabo. Data appears in Table 3.2. Mean hourly insolation measurements were made between 1966 and 1967, in Langleys. These were averaged by month and converted to MJ/m^2 (1 Langley = 0.041868 MJ/m^2).

Table 3.1: Average daily global insolation on a horizontal plane (MJ/m^2) for Mayagüez, San Juan, Ponce, Cabo Rojo, Cataño and Manatí

Month	Mayagüez	San Juan	Ponce	Cabo Rojo	Cataño	Manatí
January	14.2	14.8	16.5	16.5	16	15.2
February	15.5	16.2	18.9	19.1	22.2	16.5
March	17.1	18	21.5	22.2	19	21.7
April	18	17.5	21.7	19.4	20.3	22
May	17.1	15.3	19.2	23.1	16.6	19.1
June	17.6	18.4	20	23.6	16.8	23.5
July	16.5	20.3	22.4	22.3	24.6	20.8
August	17.2	18.9	22	20.5	21	19
September	16.3	16.4	20.4	21.7	17.9	17.7
October	15.2	16	18.3	18.9	17	17.4
November	14.7	14.6	16.4	17.7	16.1	16.3
December	13.1	13	14.8	14.2	14.8	13.6

Data for: Juana Díaz was obtained from the Natural Resources Conservation Service (NRCS) website. This was raw data in ASCII format collected every hour from 2000 to 2002. This data was then averaged to obtain monthly and yearly insolation and is presented in Table 3.2.

Aguadilla, Ceiba and Carolina data was obtained from NREL's (National Renewable Energy Laboratory) National Solar Radiation Database. This data was collected and averaged hourly from 2002-2003 and was processed to produce monthly and yearly averages. This data appears in Table 3.3.

Table 3.2: Average daily global insolation on a horizontal plane (MJ/m^2) for Fajardo, Río Grande, Gurabo (USDA), and Juana Díaz (NRCS).

Month	Fajardo	Río Grande	Gurabo	Juana Díaz
January	15.9	10	17	17.9
February	20	12.1	19.5	20.5
March	20.6	13.7	13.4	23.4
April	19.8	9.1	21.4	21
May	25.1	12.1	22.3	22.6
June	12.6	12.1	21.2	20.9
July	24.3	12.5	19.6	21.1
August	11.4	13.8	18.5	18.4
September	21.1	13.2	13.5	20.9
October	8.8	10.3	11.8	19.5
November	17.1	6.2	23.9	18
December	12.7	6.4	12.6	15.2

Table 3.3: Average daily global insolation on a horizontal plane (MJ/m^2) for Aguadilla, Ceiba and Carolina (NREL), also Guilarte, Bosque Seco, and Maricao (NRCS)

Month	Aguadilla	Ceiba	Carolina	Guilarte	Bosque Seco	Maricao
January	14.8	13.2	14.6	5.4	13.9	10.1
February	17.2	15.3	16.9	7.4	16.6	12
March	19.2	18.2	20.3	6.6	19.8	10
April	18.4	16.1	20.6	6.3	18.6	9.6
May	20.6	18.4	21.7	6	19.9	7.5
June	19.8	17.1	21.3	6.4	20.2	8.3
July	20.9	18.3	20.9	6	20.5	10.9
August	19.5	17.5	20.7	6.2	19.5	8.6
September	19.1	16.8	19.6	7	17.4	11.1
October	17	15.4	17.4	6.3	19.3	10.2
November	14.5	12.9	13.8	5.5	15.3	11.6
December	13.5	12.3	12.6	5.2	16.5	10

3.3 Beam and Diffuse Components of Radiation

Using the model described, the extraterrestrial radiation and $\overline{K}_T$, the beam and diffuse components of radiation were calculated and are presented below.

Table 3.4: Beam Radiation Data for Ponce, Cabo Rojo, Mayagüez, Manatí, Cataño, San Juan, Fajardo, Río Grande and Gurabo (MJ/m^2)

Month	Ponce	Cabo Rojo	Mayagüez	Manatí	Cataño	San Juan	Fajardo	Río Grande	Gurabo
January	10.8	10.8	8.2	9.3	10.3	8.9	10.1	4.2	11.4
February	12.5	12.7	8.7	9.8	16.8	9.5	13.9	5.4	13.3
March	14.4	15.3	9.5	14.7	11.5	10.5	13.3	6.2	6
April	13.8	11.3	9.8	14.2	12.2	9.3	11.7	2.2	13.5
May	10.8	15.1	8.7	10.7	8.2	7	17.5	4.2	14.2
June	11.6	15.7	9.2	15.5	8.4	9.9	4.6	4.2	12.9
July	14.3	14.2	8.1	12.5	16.9	12	16.6	4.6	11.2
August	14.1	12.4	9	10.8	13	10.7	3.8	5.8	10.3
September	12.9	14.4	8.5	10	10.2	8.6	13.7	5.6	5.9
October	11.5	12.2	8.2	10.5	10.1	9.1	2.6	3.7	5
November	10.4	12	8.6	10.4	10.1	8.5	11.3	1.3	4.1
December	9.1	8.5	7.3	7.9	9.2	7.3	7	1.5	6.8
Annual Average	12.2	12.9	8.7	11.4	11.4	9.3	10.5	4.1	9.5

Table 3.5: Beam Radiation Data for Juana Díaz, Aguadilla, Ceiba, Guilarte, Carolina, Guánica and Maricao (MJ/m^2)

Month	Juana Díaz	Aguadilla	Ceiba	Guilarte	Carolina	Guánica	Maricao
January	12.5	8.9	7.2	0.8	8.7	7.8	4.2
February	14.5	10.6	8.5	1.8	10.3	9.8	5.4
March	16.8	11.8	10.7	1	13	12.5	3.1
April	13	10.2	8	0.7	12.6	10.4	2.6
May	14.5	12.3	9.9	0.5	13.5	11.6	1.2
June	12.6	11.4	8.7	0.6	13.1	11.9	1.6
July	12.9	12.7	9.9	0.5	12.6	12.2	3.4
August	10.2	11.4	9.3	0.6	12.6	11.3	1.8
September	13.4	11.5	9	1.1	11.9	9.7	3.8
October	12.9	10.1	8.4	1	10.6	12.7	3.6
November	12.3	8.4	6.7	0.9	7.7	9.2	5.4
December	9.6	7.8	6.6	0.8	6.9	11.1	4.3
Annual Average	12.9	10.6	8.6	0.8	11.1	10.8	3.4

Table 3.6: Diffuse Radiation Data for Ponce, Cabo Rojo, Mayagüez, Manatí, Cataño, San Juan, Fajardo, Río Grande and Gurabo (MJ/m^2)

Month	Ponce	Cabo Rojo	Mayagüez	Manatí	Cataño	San Juan	Fajardo	Río Grande	Gurabo
January	5.7	5.7	6	5.9	5.7	5.9	5.8	5.8	5.6
February	6.4	6.4	6.8	6.7	5.4	6.7	6.1	6.7	6.2
March	7.1	6.9	7.6	7	7.5	7.5	7.3	7.5	7.5
April	7.9	8.1	8.2	7.8	8.1	8.2	8.1	6.9	7.9
May	8.4	8	8.4	8.4	8.4	8.3	7.6	7.9	8.1
June	8.4	7.9	8.4	8	8.4	8.5	8	7.9	8.3
July	8.1	8.1	8.4	8.3	7.7	8.3	7.7	7.9	8.4
August	7.9	8.1	8.2	8.2	8	8.2	7.6	8	8.2
September	7.5	7.3	7.8	7.7	7.7	7.8	7.4	7.6	7.6
October	6.8	6.7	7	6.9	6.9	7	6.2	6.6	6.8
November	6	5.7	6.1	5.9	6	6.1	5.8	5	6
December	5.7	5.7	5.8	5.7	5.6	5.7	5.8	4.9	5.8
Annual Average	7.2	7.1	7.4	7.2	7.1	7.3	6.9	6.9	7.2

Table 3.7: Diffuse Radiation Data for Juana Díaz, Aguadilla, Ceiba, Guilarte, Carolina, Guánica and Maricao (MJ/m^2)

Month	Juana Díaz	Aguadilla	Ceiba	Guilarte	Carolina	Guánica	Maricao
January	12.5	8.9	7.2	0.8	8.7	7.8	4.2
February	14.5	10.6	8.5	1.8	10.3	9.8	5.4
March	16.8	11.8	10.7	1	13	12.5	3.1
April	13	10.2	8	0.7	12.6	10.4	2.6
May	14.5	12.3	9.9	0.5	13.5	11.6	1.2
June	12.6	11.4	8.7	0.6	13.1	11.9	1.6
July	12.9	12.7	9.9	0.5	12.6	12.2	3.4
August	10.2	11.4	9.3	0.6	12.6	11.3	1.8
September	13.4	11.5	9	1.1	11.9	9.7	3.8
October	12.9	10.1	8.4	1	10.6	12.7	3.6
November	12.3	8.4	6.7	0.9	7.7	9.2	5.4
December	9.6	7.8	6.6	0.8	6.9	11.1	4.3
Annual Average	12.9	10.6	8.6	0.8	11.1	10.8	3.4

3.4 Graphical Representation of Data

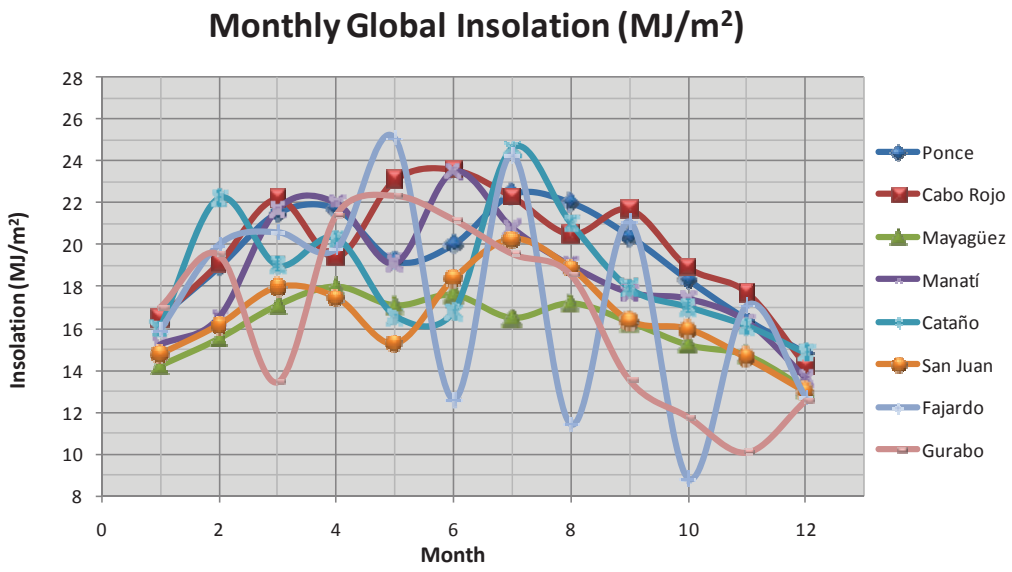

Figure 3.2: Monthly Global Insolation (MJ/m^2)

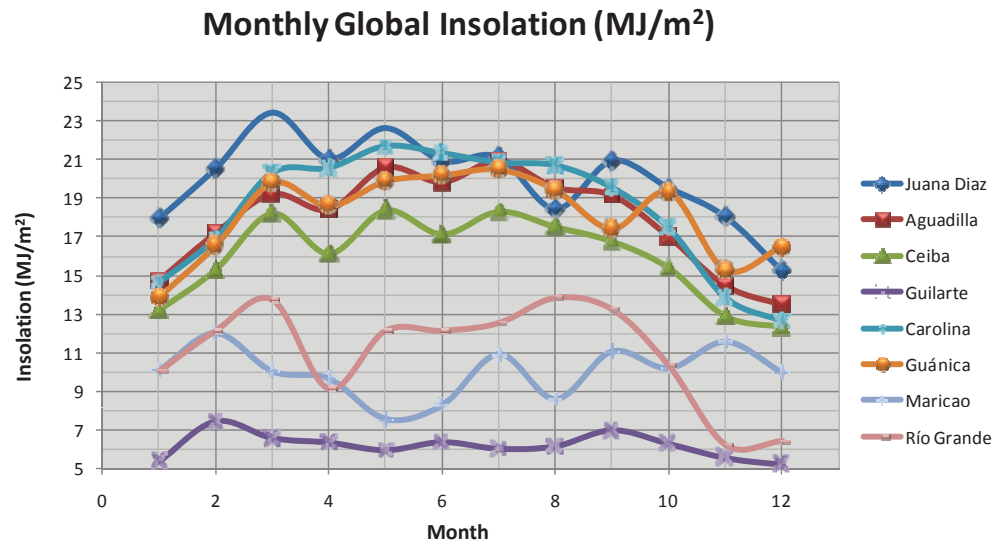

Figure 3.3: Monthly Global Insolation (MJ/m^2)

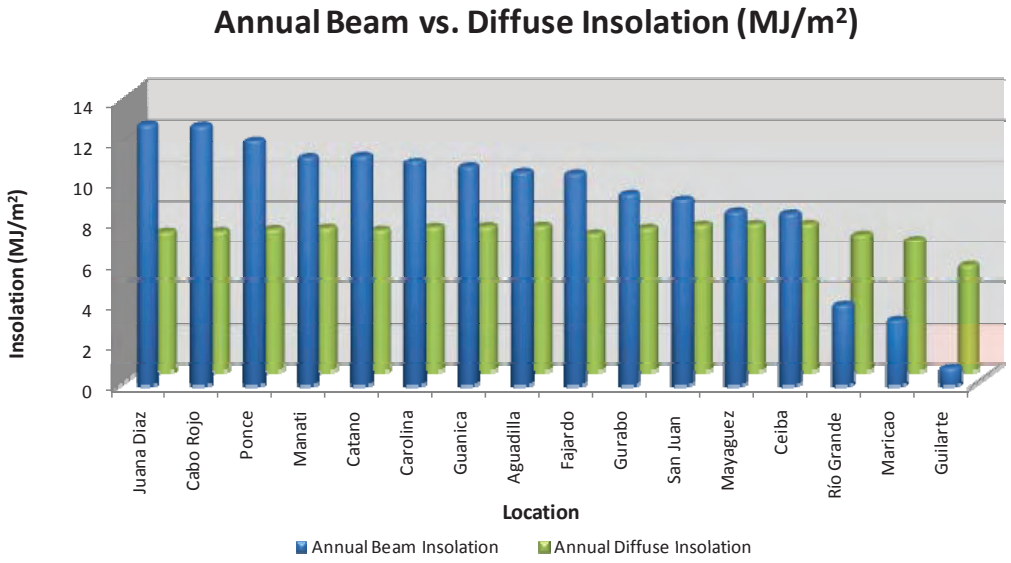

Figure 3.4: Annual Beam vs. Diffuse Insolation (MJ/m^2)

3.5 Solar Insolation Map for Puerto Rico

3.5.1 Reference

The next step after having compiled radiation data for the sixteen mentioned sites is creating an insolation map for Puerto Rico. Latitude and longitude information for each site was obtained from Google Earth®. López presents one such map in his study [7]. Since he only had radiation data for six different locations, he calculated the ratio of average yearly radiation to average yearly extraterrestrial radiation ($\overline{K}_T$) for these six locations and utilized linear regression to correlate it with the amount of annual rainfall in those locations. With the equation that resulted from the linear regression analysis, López calculated the average yearly radiation of other municipalities in Puerto Rico taking into account the average annual rainfall. Rainfall to $\overline{K}_T$ correlated by 94%. Figure 3.5 shows the insolation map produced by López.

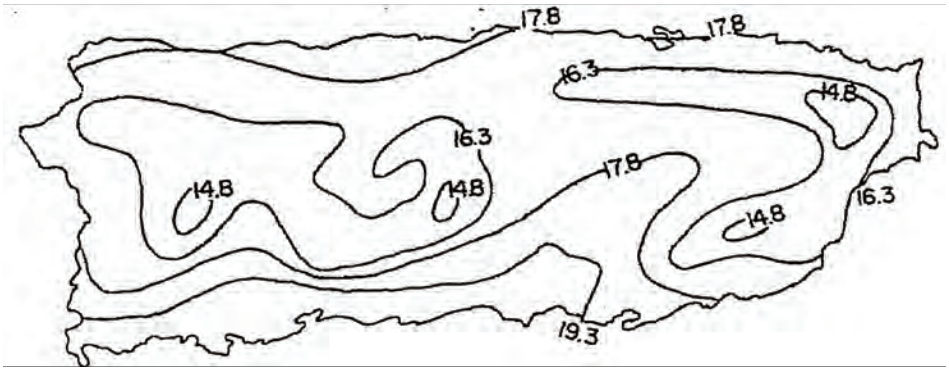

Figure 3.5: Average daily insolation map for Puerto Rico using $\overline{K_T}$ and rainfall correlation by López (MJ/m^2), adapted from [7]

A rather different approach was carried out to generate an insolation map for Puerto Rico. Interpolation seemed like a suitable method for generating an insolation matrix that could provide the data necessary for constructing the proposed insolation map.

The data collected should not be interpolated linearly with respect to latitude, since there are very distinct climatic and geographical differences when moving from east to west along Puerto Rico. If longitude is to be considered, along with latitude, some sort of numerical analysis method is needed. The most frequent problem in modeling physical phenomenon is the scattered data interpolation problem. Data is usually collected at certain points that are scattered in space with no special structure. This type of problem normally contains two or more dimensions, that is, two or more independent variables. Examples of these are: interpolation of altimeter data, geoids, temperature, fluid dynamics, and image processing [18]. There are well known straight-forward methods for solving one-dimensional problems, such as: linear, piecewise linear, polynomial or cubic interpolation. For greater dimension problems, some of these methods could be used, but are not so straight-forward and require extensive algebraic manipulation, thus producing far larger systems of equations to be solved.

3.5.2 Methodology

MATLAB® provides a function for solving this type of problem, giving the user the choice of several interpolation methods to be used: bilinear, bicubic, nearest or biharmonic (or bicubic) spline interpolation. All these methods were tested on the radiation data processed, being the biharmonic spline interpolation method the only one that gave reasonable results. The main problem with the other methods is that the function might return points on, or very near the convex hull of the data as NaNs (Not a Number, usually division by zero). This is because roundoffs in the computations make it difficult to determine if a point near the boundary is in the convex hull. The "linear" and "nearest" methods also have discontinuities in the first and zero'th derivatives, respectively. All methods, except biharmonic spline, are based on a Delaunay triangulation of the data. The usefulness of the bicubic method lies in the fact that the interpolated surface is continuous everywhere and also continuous in the first derivative in all directions.

`griddata`, the MATLAB® function employed, requires several inputs which in the solar radiation case are: vectors for the data collected in terms of latitude, longitude, and radiation. It also requires uniform grid vectors for the independent variables (latitude and longitude) for it to construct a 'grid' in which the radiation data can be interpolated. Figure 3.6 presents the resulting solar insolation map.

After having prepared the insolation map, the most suitable locations for any type of solar system development lie in the south and in the extreme south-western tip of Puerto Rico. The south is a somewhat dry and desert-like zone, less populated than the rest of the island and can serve as a potentially favorable area for the development of solar systems. Data from Gilarte and Maricao were not included in the analysis for

constructing the insolation map.

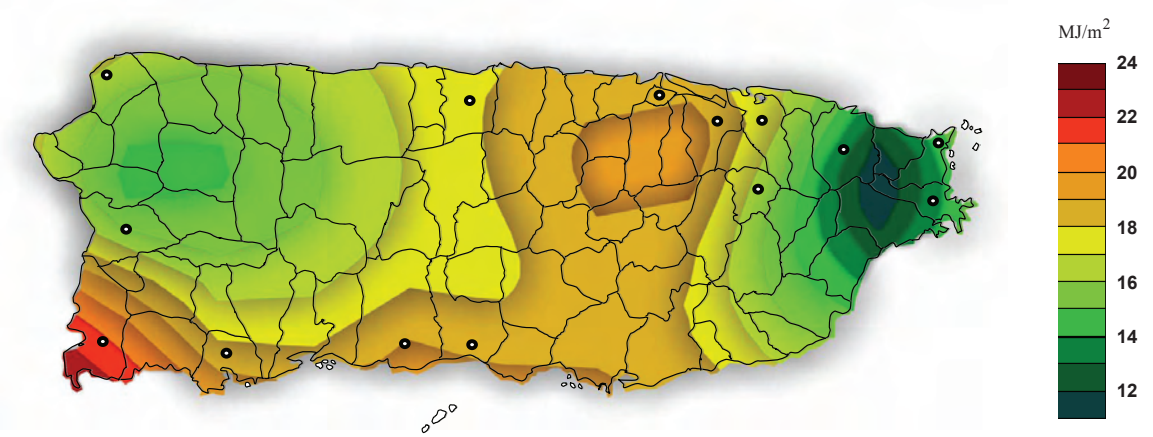

Figure 3.6: Insolation Map for Puerto Rico

3.5.3 Map Validation

The correlation approached by López [7] was then utilized as a means to validate the accuracy of the insolation map generated and the interpolation method used. Using the data collected, $\overline{K}_T$ was computed for each of the fourteen locations, and was correlated with their respective annual rainfall shown in Figure 3.8.

The regression analysis conducted correlated $\overline{K}_T$ and rainfall with an 89.7%. This data appears in Table 3.8 and Figure 3.7.

Table 3.8: Data used for the linear regression analysis. Rainfall data was obtained from NOAA [1]

Location	Annual Rainfall (in.)	Annual Rainfall (cm.)	K_T
Ponce	35.48	90.12	0.564
Cabo Rojo	45.01	114.33	0.581
Mayagüez	68.66	174.4	0.47
Manatí	56.88	144.48	0.541
Cataño	60	152.4	0.544
San Juan	68.97	175.18	0.487
Fajardo	62	157.48	0.511
Río Grande	130	330.2	0.318
Gurabo	62.08	157.68	0.526
Juana Díaz	39.74	100.94	0.584
Aguadilla	55.53	141.05	0.522
Ceiba	52.24	132.69	0.465
Guánica	31.47	79.93	0.53
Carolina	50.76	128.93	0.533

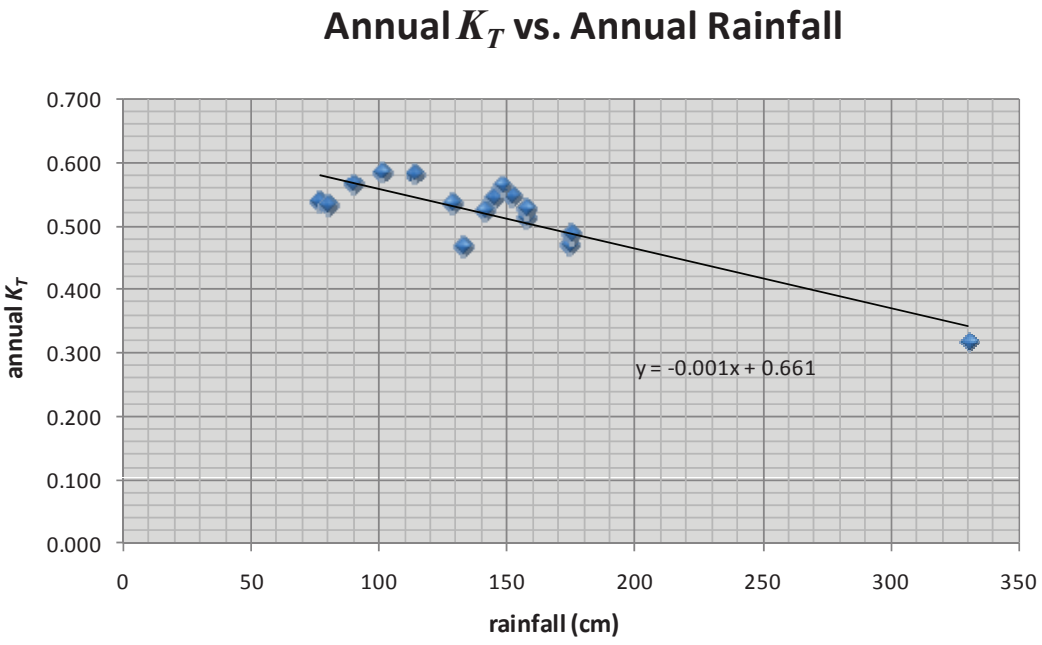

Figure 3.7: Linear fit output from Microsoft Excel

The equation produced by the regression analysis was then used to validate the accuracy of the insolation map produced by the MATLAB® Biharmonic Spline Interpolation Method. The locations validated are presented in Table 3.9. Most of the percent differences remain low, proving that the map is reasonable.

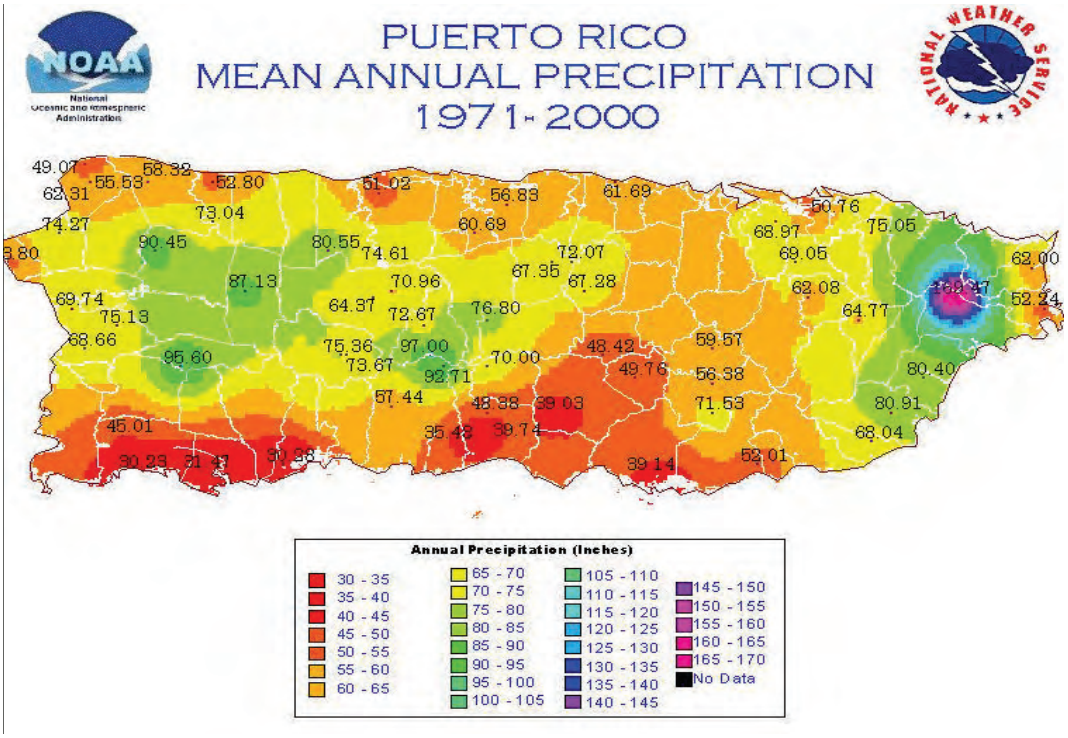

Figure 3.8: Mean annual precipitation data used for the regression analysis (NOAA)

Table 3.9: Test data for testing the generated insolation map obtained from linear regression

Municipality	Rainfall (cm)	$\overline{K_T}$ Predicted	Radiation Predicted (MJ/m^2)	Map Average Radiation (MJ/m^2)	% Difference
Utuado	180.2	0.481	16.5	16.5	0
Barranquitas	123	0.538	18.47	18.5	0.2
Ponce	90	0.571	19.6	19.5	0.5
Manati	154.2	0.507	17.4	17.5	0.6
Mayaguez	177.1	0.484	16.61	16.5	0.7
Aibonito	126.4	0.535	18.35	18.5	0.8
Yabucoa	205.5	0.455	15.64	15.5	0.9
Salinas	99.4	0.562	19.28	19.5	1.1
Gurabo	157.7	0.503	17.28	17.5	1.3
Maunabo	172.8	0.488	16.76	16.5	1.6
Aguada	188.6	0.472	16.22	16.5	1.7
Guayama	132.1	0.529	18.16	18.5	1.9
San Sebastian	229.7	0.431	14.8	14.5	2.1
Canovanas	190.6	0.47	16.15	16.5	2.2
Guanica	79.9	0.581	19.95	19.5	2.3
Lares	221.5	0.44	15.09	15.5	2.7
Guayanilla	77.2	0.584	20.04	19.5	2.7
Lajas	76.8	0.584	20.06	19.5	2.8
Juana Diaz	100.9	0.56	19.23	18.5	3.9
Cayey	143.2	0.518	17.78	18.5	4
Arecibo	129.6	0.531	18.24	17.5	4.2
Carolina	128.9	0.532	18.27	17.5	4.3
Trujillo Alto	175.4	0.486	16.67	17.5	4.9
Aguadilla	124.6	0.536	18.41	17.5	5.1
Quebradillas	185.5	0.475	16.32	15.5	5.2
Cidra	151.3	0.51	17.5	18.5	5.6
Isabela	148.1	0.513	17.61	16.5	6.5
Dorado	156.7	0.504	17.31	18.5	6.6
Jayuya	184.6	0.476	16.35	17.5	6.8
Maricao	242.8	0.418	14.36	15.5	7.7
Humacao	204.2	0.457	15.68	14.5	7.8
Orocovis	195.1	0.466	15.99	17.5	9
Corozal	170.9	0.49	16.82	18.5	9.5
Juncos	164.5	0.496	17.04	15.5	9.5
Morovis	171.1	0.49	16.82	18.5	9.5
Fajardo	157.5	0.504	17.29	15.5	10.9
San Juan	175.2	0.486	16.68	19	13
Ceiba	132.7	0.528	18.14	15.5	15.7
Naguabo	430.5	0.231	7.91	11	32.6

3.5.4 Map Limitations

There are, however, some limitations to the map due mainly to the fact that the data collected represents only sixteen municipalities in Puerto Rico that lie mainly in the coastal areas, meaning that locations in the interior part of the island are not represented. There is also a biasing factor in the data because several of the locations are considered forest areas. There is obviously a much lower radiation level if there are significant amounts of rainfall. Some of these locations are: Río Grande (Yunque), Gurabo, Guilarte and Maricao. Some of the insolation data from these locations was not considered when generating the insolation map for deeming them too low. Measurements could also be made in the central, as well as, in the southeastern part of Puerto Rico. There is also the uncertainty of data accuracy, instrument calibration, and data processing. If all these factors are carefully taken into consideration, there is no doubt that it will contribute to a more accurate insolation map for Puerto Rico in the future. This will surely benefit the development of solar technologies in Puerto Rico.

3.5.5 Solar Data for Representing Transient Operation

The preceding solar data proves useful for making preliminary analyses of solar systems. By using average yearly or monthly solar radiation values, system performance can be estimated, but not very accurately. Since radiation in Puerto Rico is mainly diffuse due to the island's geographic location in a tropical region, daily solar data taken at hourly intervals is most useful for studying in detail the system's performance throughout an entire day. That way, annual output can be estimated by identifying clear or cloudy days in a year. A radiation calendar is usually useful for predicting system behavior and performance throughout a defined period of time. Figure 3.9

presents one such calendar for Juana Díaz, during the month of June 2003.

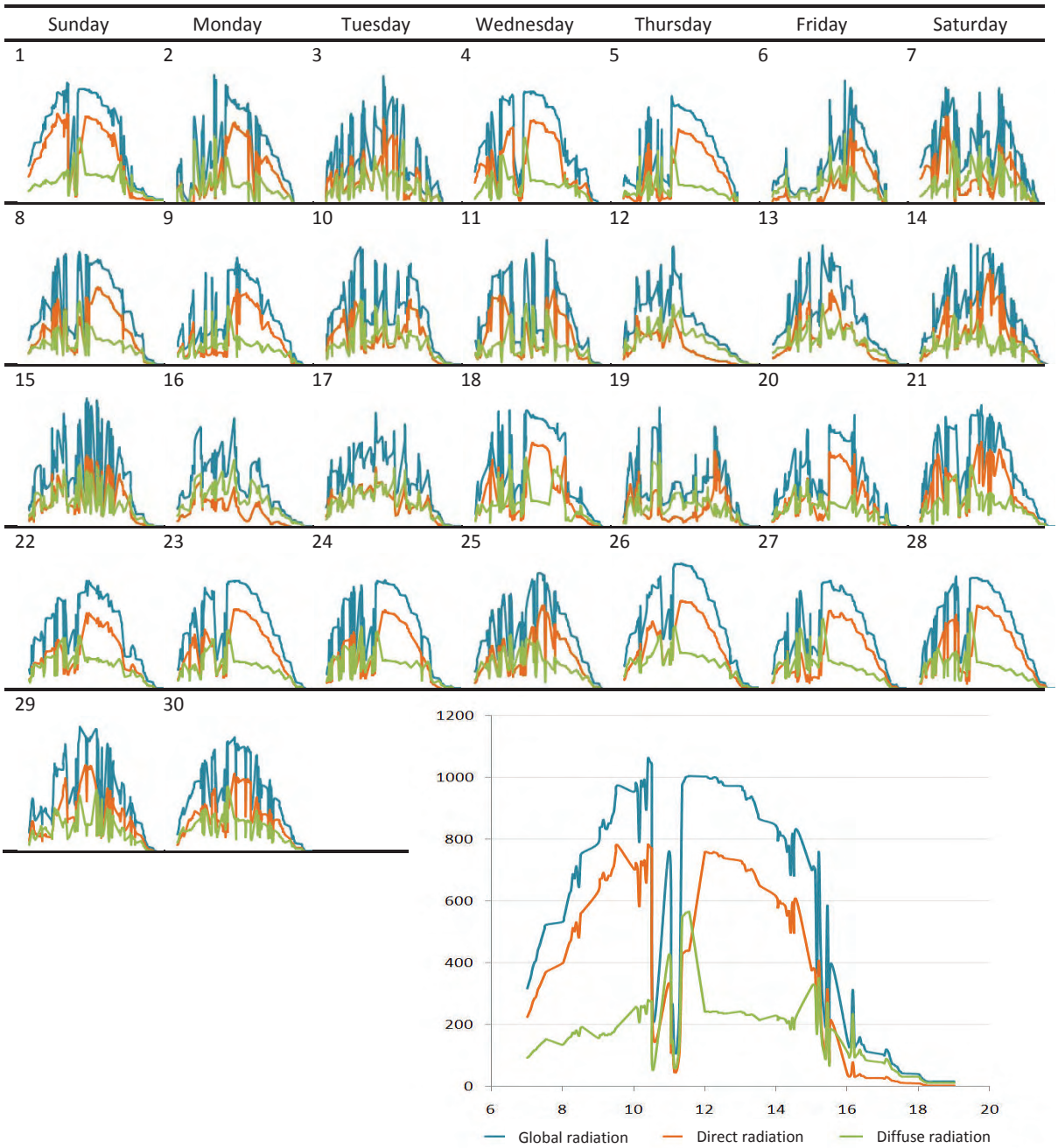

Figure 3.9: Radiation calendar for June 2003

3.6 Climate and Solar Resource Comparison

Since the proposed system can be compared up to a certain point with the SEGS in California, climatic conditions should be compared as well. Climatic data was obtained from the NASA Langley Research Center, Atmospheric Science Data Center.

Table 3.10: Climatologic data for Barstow, California

Month	Insolation, $kWh/m^2/day$	Clearness, 0 - 1	Temperature, °C	Wind, m/s	Rain, mm	Wet days, d
January	2.84	0.57	5.12	5.21	16	4.2
February	3.64	0.57	7.11	5.2	12	4
March	5.04	0.61	11.16	5.14	10	4.6
April	6.41	0.65	15.28	5.06	7	2.6
May	7.48	0.68	20.62	5.23	3	1.1
June	7.96	0.69	24.86	5.21	1	0.5
July	7.33	0.65	28.23	4.76	5	0.7
August	6.31	0.61	27.53	4.35	8	1.2
September	5.22	0.59	23.33	4.63	6	1.5
October	4.09	0.58	16.83	4.65	4	1.6
November	3.05	0.57	9.09	5.15	10	2.8
December	2.6	0.57	4.8	5.22	12	3.5

If insolation levels are compared, it appears that Juana Díaz has a more adequate solar resource. It remains high and rather constant throughout the year as opposed to Barstow, which has a higher insolation during the summer months but, it is greatly reduced during the fall and winter months. Even though Puerto Rico has a decent solar resource, there is another factor that plays an important role in system performance: Precipitation. From the preceding tables, on average, Barstow has only 28 wet days a year whereas, Juana Díaz has 208.

Table 3.11: Climatologic data for Juana Díaz, Puerto Rico

Month	Insolation, kWh/m^2/day	Clearness, 0 - 1	Temperature, °C	Wind, m/s	Rain, mm	Wet days, d
January	4.66	0.61	24.92	7.78	57	19.6
February	5.31	0.61	24.7	7.32	56	14.8
March	6.13	0.63	24.78	6.95	63	14.8
April	6.57	0.63	25.19	5.86	118	13.7
May	6.43	0.6	25.81	6.31	188	15.5
June	6.58	0.61	26.28	6.97	120	16.5
July	6.61	0.61	26.38	7.49	137	18.7
August	6.49	0.62	26.5	6.97	197	19.3
September	5.81	0.58	26.44	6.16	243	17.6
October	5.34	0.59	26.27	5.57	231	18.1
November	4.5	0.57	26.05	7.11	148	18.9
December	4.23	0.57	25.44	7.31	78	20.8

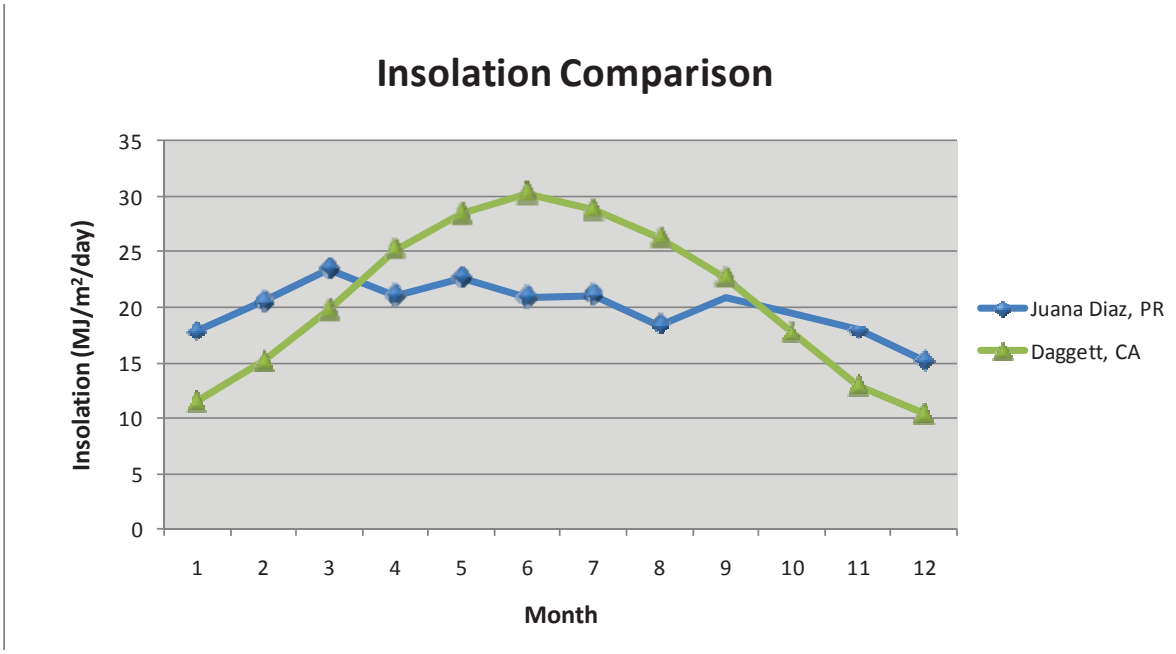

Figure 3.10: Insolation Comparison for Juana Díaz, Puerto Rico and Barstow, California

Chapter 4

SOLAR THERMAL POWER PLANTS (STPPs)

4.1 Introduction

A *Solar Thermal Power Plant* (STPP) works like a conventional thermal power plant, but uses solar energy instead of a fossil fuel as a heat source for producing steam. Even though it is free, solar energy has three noteworthy disadvantages: energy density, availability, and conversion [5]. The energy density incident on Earth's surface is low, around 1 kW/m^2. The lack of availability due to the day-night cycle poses yet another problem for solar thermal systems. These two, however, can be alleviated by optical concentration and thermal storage. Energy conversion remains expensive due to the low efficiencies encountered in many of these systems.

There are several different ways in which a STPP can be designed, constructed, and operated. It is usually the system components that dictate such designs. There can be variations, but the typical STPP with linear geometry contains the following

components: collector array & solar tracking system, absorber, heat transfer fluid or HTF, heat transfer mechanisms such as heat exchangers and condensers, electromechanical devices such as generators, and an energy storage system or hybridization for attending solar transients.

4.2 Solar Energy Collection and Concentration

The solar collector array can be categorized as: reflecting or refracting, concentrating or non-concentrating, imaging or non-imaging, tracking or fixed, linear, focal or central, etc. Collectors can be further described in terms of: their concentration ratio, thermal and optical performance, heat transfer capability, and overall efficiency [19, 20, 9]. Solar tracking of the collector array is needed if there is a significant drop in system performance [12]. This is usually encountered in imaging-type concentrators. Several collector geometries will be discussed. There have been several new developments in materials concerning collector manufacturing. NREL [21] recently conducted a study regarding different collector materials. The objective of this research was to identify new, cost-effective, advanced reflector materials that will be durable with weathering. Among these were: thick and thin glass mirrors, aluminized mirrors and silvered polymers.

4.3 Solar Collectors

Solar collectors are mechanical devices which capture the radiant solar energy and convert it to useful thermal energy. Depending on the different applications (water or space heating, steam production or electricity generation), there are different requirements as to the temperature the collector system can achieve [5]. This fact usually determines if the collector must be concentrating (for attaining higher temperatures)

or non-concentrating (for lower temperature applications). The most relevant classification concerning this study lies on whether the collector is in fact imaging or non-imaging. Concentrating collectors for electricity production available today are of the imaging type.

The science of non-imaging optics is concerned mainly with the optimal transfer of light radiation between a source and a target, not in forming an image of the source, like imaging optics. Non-imaging optic systems are particularly better at concentrating and illuminating than their imaging counterparts [9].

The flux at the surface of the Sun is approximately 63,000 kW/m^2. It decays with the square of the distance from the Sun to the Earth to a value of 1.370 kW/m^2 just above the Earth's atmosphere, and typically to 0.8 - 1 kW/m^2 at the ground. In principle, the Second Law of Thermodynamics permits an optical device to concentrate the solar flux to obtain temperatures at the Earth's surface not exceeding the Sun's surface temperature. In practice, conventional means for flux concentration fall short of this maximum because imaging optical designs are inefficient at delivering maximum concentration [9]. Non-imaging light-gathering devices can improve on focusing designs by a factor of four or more, and approach the thermodynamic limit. Gleckman [19] has been able to use a non-imaging design to concentrate terrestrial sunlight by a factor of 56,000, producing an irradiance that could exceed that of the solar surface.

4.3.1 Flat-Plate

Flat-plates are the most commonly used solar collectors, and can be categorized as non-concentrating and non-imaging. They can operate at temperatures up to about 90 °C, making them suitable for hot water and space heating applications. This type

of collector has several advantages which include: the lack of moving parts, durability, and capability of collecting both direct and diffuse radiation [22].

4.3.2 Evacuated-Tube

The typical evacuated-tube is in fact a flat plate collector embedded in a vacuum envelope that eliminates both convection and conduction losses. Since a vacuum would cause a typical flat-plate collector to collapse, a tubular design is used instead [22]. Because evacuated-tube collectors lose less heat to the environment than flat-plate collectors do, they: can operate at higher temperatures around 175 °C, can collect both direct and diffuse solar radiation, do not require tracking, can operate at somewhat lower insolation levels by collecting more energy on cloudy days or in colder climates, and are less susceptible to wind-induced losses due to its geometry. Both non concentrating and concentrating geometries are shown in Figures 4.1 and 4.2, respectively.

4.3.3 Parabolic Trough

A parabolic trough collector can be categorized as a tracking, concentrating, imaging collector with a linear geometry suitable for medium temperature applications up to 400 °C. Both spherical and parabolic geometries are represented in solar thermal concentrators. Parabolic Trough systems will be discussed in some detail, provided that these systems are the most similarly commercially available technology that can be compared to the proposed CPC system in this work.

Parabolic troughs are commonly used to produce steam for a Rankine Cycle. They are currently the most proven electricity generating technology by solar means. There are nine large commercial-scale solar power plants that have been operating in the California Mojave Desert since 1984. These nine *Solar Energy Generating Systems* (SEGS)

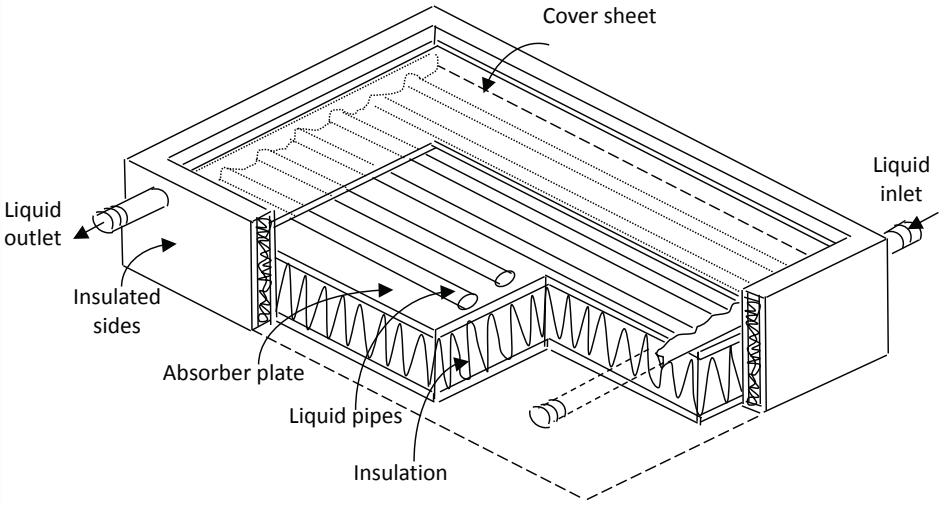

(a) Flat-plate collector

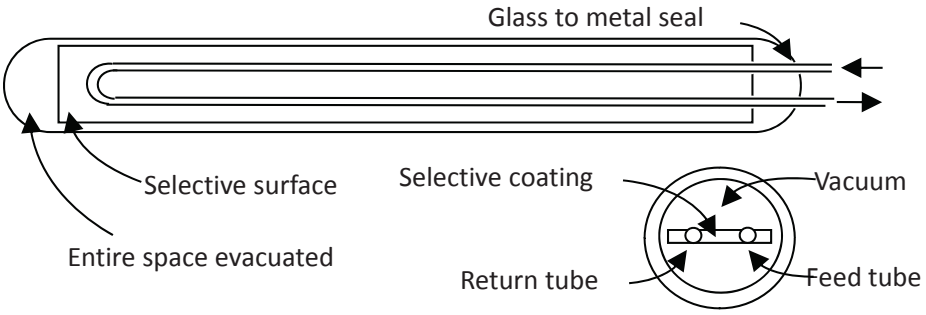

(b) Evacuated-tube collector

Figure 4.1: Non concentrating collectors, redrawn from [5]

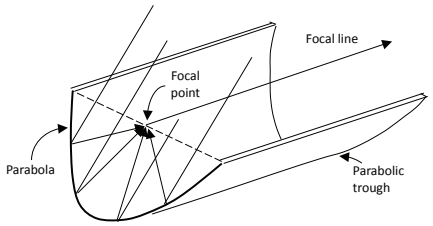

(a) Parabolic trough

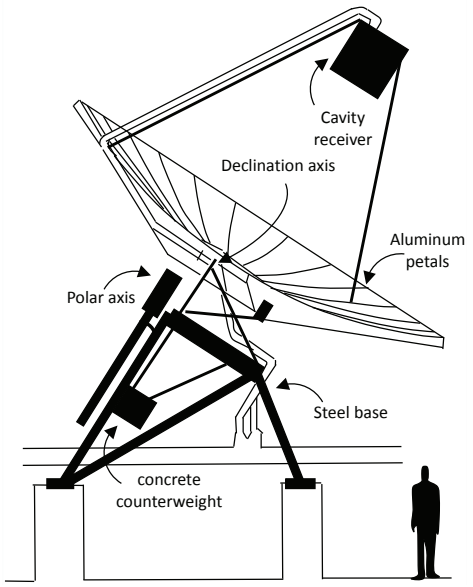

(b) Dish

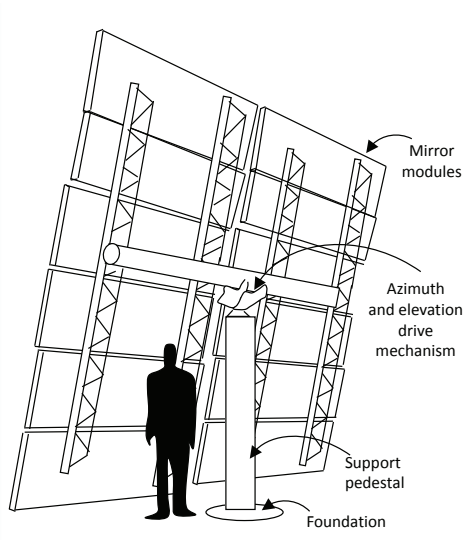

(c) Heliostat

Figure 4.2: Concentrating collectors, redrawn from [5]

are the largest solar energy generating facility in the world and range in power outputs from 14 to 80 MW, totaling 354 MW of installed capacity. They are located in California's Mojave Desert, where insolation is among the best in the U.S. The facilities have a total of 936,384 mirrors and cover more than 1,600 acres. It has been said that the SEGS plants displace 3,800 tons of pollution per year, power 232,500 homes, and displaces 815,000 barrels of oil annually. The plants use parabolic trough solar thermal technology along with natural gas to generate electricity. 90% of the electricity is produced by sunlight and the other 10% is produced by natural gas [23, 24].

The sun reflects off the mirrors and is directed to a linear pipe filled with synthetic oil, Therminol VP-1, which heats to almost 400 °C. The synthetic oil transfers its heat to water, which boils and drives the Rankine cycle steam turbine, thereby generating electricity. The SEGS power plants were built by Luz Industries and commissioned between 1984 and 1991 [10, 12].

Figure 4.3: Collectors and absorber in a parabolic trough plant (NREL)

Parabolic troughs are usually installed so that their axes of rotation are oriented either north-south, or east-west. However, any orientation is suitable. The orientation

of the troughs usually depends on the orientation of the land areas on which they will be installed. Seasonal variations in collector output for north-south oriented troughs can be large. Usually, three to four times more energy is delivered daily during average summer months than during average winter months, depending on the latitude and site weather patterns. Seasonal variations are, however, much smaller for an east-west orientation, typically less than 50%, and are caused primarily by seasonal variations in the amount of available insolation [5].

Figure 4.4 depicts a parabolic trough power plant schematic. A Parabolic Trough STPP comprises hundreds of trough-shaped parabolic mirrors, which are continuously adjusted to face the sun. They have the ability to concentrate the sun's rays on receivers located along its focal line [5]. The absorbed solar radiation warms up the heat transfer fluid (Therminol VP-1) flowing through the absorber tube. It is conducted along a heat exchanger to produce steam that propels a steam turbine. The turbine is mechanically coupled to a generator to produce electric power.

4.3.4 Parabolic Dish

The parabolic or solar dish is in fact a paraboloid of revolution. It can be categorized as a two-axis tracking, imaging concentrator of focal geometry that uses a mirror array to reflect and concentrate incoming radiation to a receiver, in order to achieve the temperatures required to efficiently convert heat to work. The receiver of choice is a Stirling Engine located at the focal point of the parabolic dish. These systems have the ability and advantage of producing electric power without the complications of trough systems. Dish systems are also characterized by high efficiency, modularity, autonomous operation, hybrid capability and the highest solar-to-electric conversion efficiency of all solar thermal systems [22].

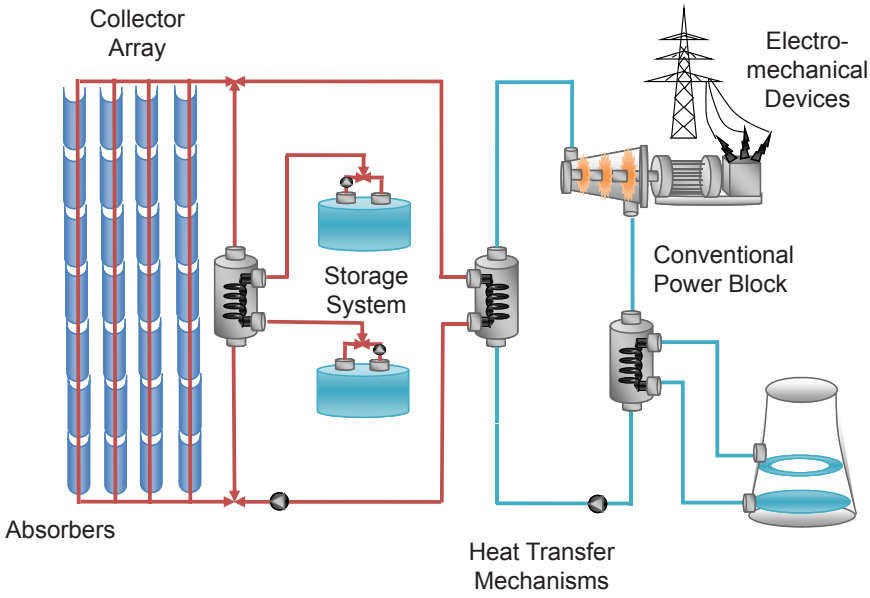

Figure 4.4: Parabolic trough schematic

4.3.5 Central Receiver

A central receiver or power tower consists of a receiver located on a tower surrounded by a field of individually aimed, imaging reflectors or heliostats that track the sun in two axes. Since all of the energy is transmitted to a central receiver in the form of light, there are no piping losses. Molten salts are the HTF of choice. This HTF is heated in the receiver cavity to produce steam through heat exchangers for power generation. These systems can achieve very high energy concentrations and temperatures. There are, however, several drawbacks as to this type of system including: tower support costs, highly accurate heliostat optics, and exclusive use of direct insolation [19, 25].

4.3.6 Compound Parabolic Concentrator (CPC) Trough

The Compound Parabolic Concentrator Trough can be classified as a non-imaging, stationary concentrating collector with linear geometry. This collector configuration

can attain almost the maximum theoretical concentration ratio. Since it is the collector of choice for this work, it will be discussed further in the next chapter.

4.4 Absorber

The radiating solar energy is directed to the receiver, absorber, or heat collection element (HCE) by the collector array, heating the HTF. Absorbers can differ geometrically, upon desired application, taking into consideration: radiation characteristic of materials, absorbed radiation, and heat losses. Even though there are several companies producing receivers for STPPs, the typical receiver (as seen in Figure 4.5) consists of a specially coated steel absorber tube embedded in an evacuated glass envelope. This tube must be capable of absorbing lots of solar radiation without emitting significant amounts of heat, usually with an absorption rate of around 95%.

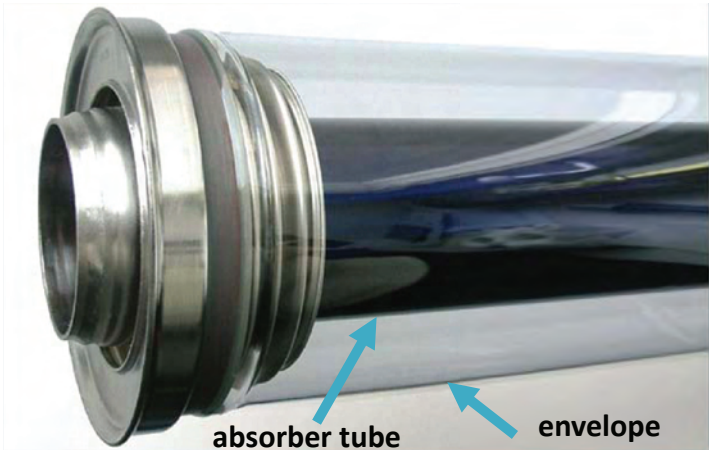

Figure 4.5: Parabolic trough absorber or receiver (NREL)

The glass envelope tube, however, is usually made of a coated, highly-transparent and robust borosilicate glass, usually allowing more than 95-96% of the available solar radiation to penetrate. The vacuum is able to successfully suppress conductive and convective losses, thereby improving receiver performance. Substantial testing and

studies must be done to improve receiver technology in order to achieve higher operating temperatures in solar systems [26].

4.5 Heat Transfer Fluid (HTF)

The HTF can be one of the following: water, water-glycol mixtures, silicone compounds, fluorocarbons, inorganic salt mixtures, hydrocarbons, or liquid metals [23, 3]. If other than water is used, it is conducted through a heat exchanger to produce superheated steam to propel a turbine or heat engine. Oils are often used as a HTF, but water and molten salts are gaining special attention in the STPP realm.

4.5.1 Water

Water is nontoxic, nonflammable, inexpensive, and has excellent heat transfer characteristics. Direct Steam Generation (DSG) systems are currently under study. Several projects are underway in Plataforma Solar de Almería (PSA) in Spain.

Their insights [27, 28]: there is a smaller environmental risk because oil is replaced by water, higher steam temperatures can be attained (maximum steam temperature with oil, 380 °C), and overall plant configuration is more simple, lower investment and O&M costs and higher plant efficiency. They also point out several disadvantages that merit further study: difficult solar field control under solar radiation transients, instability of the two-phase flow inside the receiver tubes, temperature gradients at the receiver pipes, and thermal storage. PSA is currently studying several collector configurations for solving the above mentioned disadvantages. These configurations are depicted in Figure 4.6 and are briefly described below:

Once-through mode: The water fed to the collector will be preheated, evaporated,

and superheated in a single loop. This mode represents the highest cost reduction but, the most challenging in terms of stability and controllability.

Injection Mode: Liquid water is injected to control the vapor phase during evaporation. This scheme involves a control scheme, which increases investment costs.

Recirculation Mode: This mode employs a steam separator when water is present in both vapor and liquid form. Vapor is fed back to the collector array for superheating and the liquid is recirculated to the inlet. Even though there are no known stability or control problems, this scheme produces the highest system cost.

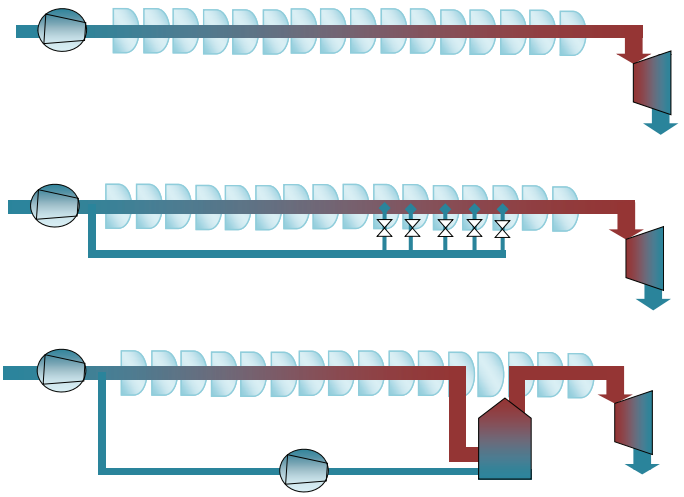

Figure 4.6: Collector configurations for direct steam generation. In order from top to bottom: once-through, injection and recirculation modes

Even though DSG was considered for this investigation, it was not viable due to the downfall of not having any proven *Thermal Energy Storage* (TES) medium for storing water vapor. Hence, a heat exchanger would ultimately be needed to couple the HTF and the TES loops.

4.5.2 Molten Salts

Molten salts, on the other hand, are being seriously considered as HTF for future plants. The main advantage in using molten salts as HTF is that they can also be used as the TES medium [29]. Molten salts are compositions of different types of salts usually used to transport and store heat. These salts are becoming better HTFs as opposed to the oils currently in use in solar thermal power plants with linear geometry, such as the SEGS troughs. As its name implies, molten salts are basically salts that have been melted into liquids. The resulting liquid is stable, with a volumetric heat capacity similar to water and flows much like water does [3]. The main advantages of a molten salt versus water lie in its higher operating temperatures ($450 - 500\,^{\circ}\mathrm{C}$) and the fact that it contracts, as opposed to expanding, like water does, while freezing. The current HTF (VP-1 oil from Therminol) can only provide a solar field temperature of $393\,^{\circ}\mathrm{C}$ before it becomes unstable. Molten salt is also more economical and more environmentally friendly than the current HTF [30].

Several questions remain regarding molten salt implementation as a HTF in the solar field, such as: what is the practical upper temperature limit; will O&M be feasible working with salts in a trough field, especially freeze protection?; will materials, O&M, performance and other factors make capital costs too high?, or will costs be reduced by using molten salts? [29]. By a means to answer some of these questions, evaluations were carried out comparing performance and several economic aspects of trough plants using oil and molten salt as HTFs. The findings are summarized in Table 9, proving that a system with storage and molten salt as the HTF is a feasible and much more economically viable alternative.

There are also several challenges regarding the use of molten salts as HTF. The

main challenge is due to the salt's high freezing point at about $120 - 220\,^{\circ}\mathrm{C}$, for different types of salts. This introduces the need of freeze protection in the solar field. The oil currently used freezes at about $15\,^{\circ}\mathrm{C}$, so, it does not pose a problem in the current systems. There are also other disadvantages regarding material costs. Since higher temperatures can be achieved, several system components such as: pipes, heat exchangers and even receivers will have to be modified accordingly [3, 29].

4.6 Power Block and Balance of Plant

The power block, system which converts mechanical energy into electricity, includes the steam turbine and generator, steam turbine and generator auxiliaries, feedwater, and condensate systems. Balance-of-plant includes any other equipment not contemplated in the solar collection system, Thermal Storage System (TES) or power block, such as: general balance-of-plant equipment, condenser and cooling tower system, water treatment system, fire protection, piping, compressed air systems, closed cooling water system, plant control system, electrical equipment, cranes and hoists [31, 32]. Since so many components are considered, they are usually lumped to facilitate analysis.

4.7 Heat Exchanger (HX)

The heat exchanger (HX) provides a means for transferring heat from the hot HTF to the cold fluid, usually water, that will propel the turbine. It usually involves convection in each fluid and conduction through the wall that separates the two fluids. These effects are taken into consideration by a HX overall heat transfer coefficient, U_{HX}, which depends on the individual resistances due to convection and conduction through the pipes and wall, and on the heat exchanger geometry itself. There are usually several stages in the heat exchanging process [5, 33]. These processes can be seen in Figure

4.7.

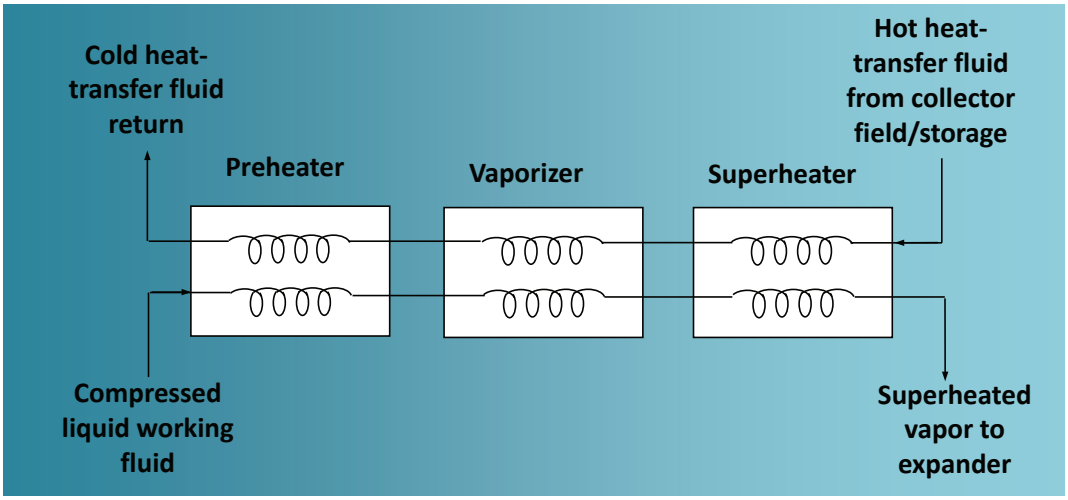

Figure 4.7: Heat exchanging steps from the hot to the cold fluid

There are many different types of heat exchangers and are categorized according to its flow arrangement, construction, and the required application. Some of the most common configurations are: concentric tubes, the compact, shell-and-tube, the plate, and the regenerative HX [34, 35, 36]. The most commonly encountered in solar thermal applications is the sell-and-tube HX [23, 29]. It contains a large number of tubes or pipes packed in a shell with their axes parallel to it. It provides a comparatively large ratio of heat transfer area to volume and weight, it is relatively easy to construct in a wide range of sizes, and is mechanically rugged enough to withstand normal shop fabrication stresses, shipping and field erection stresses, and normal operating conditions.

4.7.1 HX Energy Balance

The basic heat exchanger equations can be obtained by analyzing Figure 4.8 and the mechanisms of heat exchange, namely, conduction and convection. Heat is transferred from the hot fluid to the inside of the wall by convection, through it by conduction, and then from the outside of the wall to the cold fluid by convection [2, 35].

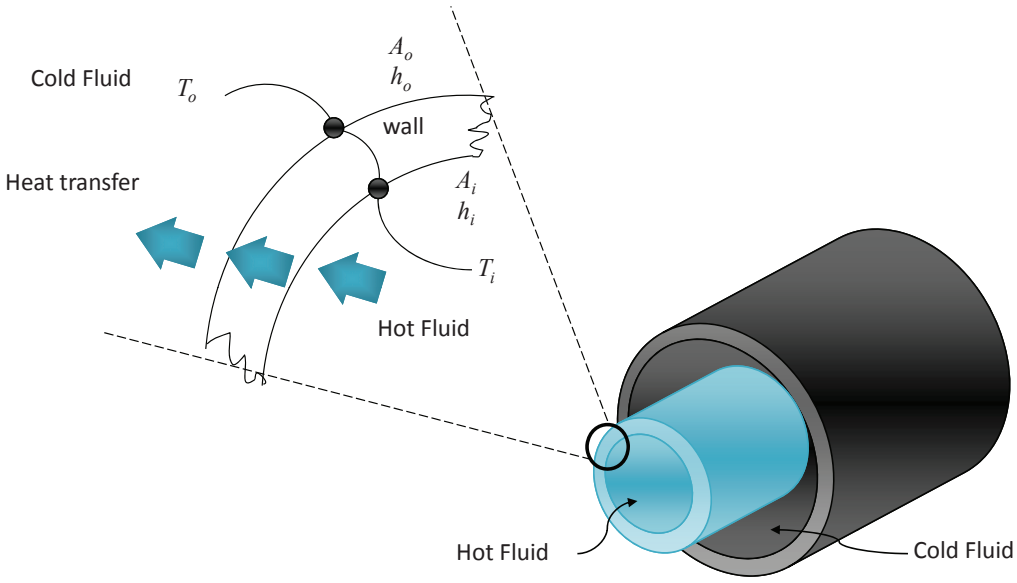

Figure 4.8: Mechanisms of heat exchange through the walls of a HX

The thermal resistance network can then by described by the following equation:

$$R_{total} = R_i + R_{wall} + R_o = \frac{1}{h_i A_i} + \frac{\ln(D_o/D_i)}{2\pi k L} + \frac{1}{h_o A_o} \tag{4.1}$$

where the subscripts i, o and $wall$ refer to the inner, outer and wall resistances, respectively. It is useful to express the rate of heat transfer between the two fluids as:

$$\dot{Q} = \frac{\Delta T}{R_{total}} = U_{HX} A \Delta T = U_i A_i \Delta T = U_o A_o \Delta T \tag{4.2}$$

where U_{HX} is the HX overall heat transfer coefficient.

The inner and outer rate of heat transfer exists because the HX has two surface areas which are not usually equal to one another. If lacking design constraints such as diameters and length, HX overall heat transfer coefficients can be found in tables [36].

There are two methods of HX analysis for obtaining the HX's heat transfer rate, which are: the log-mean-temperature-difference and the effectiveness-NTU method. They both rely on the following assumptions: HXs are steady-flow devices, so kinetic and potential energy changes are negligible, the fluid's specific heat is taken as an average constant value in a specified temperature range and the HX is assumed to be perfectly insulated, so there is no heat loss to the surroundings [2]. Based on these assumptions and on the 1st Law of Thermodynamics, it can be said that the rate of heat transfer from the hot fluid be equal to the rate of heat transfer to the cold one:

$$\dot{Q} = \dot{m}_c C_{pc}(T_{c,out} - T_{c,in}) = \dot{m}_h C_{ph}(T_{h,in} - T_{h,out}) \tag{4.3}$$

where the subscripts c and h stand for cold and hot fluids, respectively.

The heat capacity rate, $\dot{C}$, which is the product of the fluid's mass flow rate and its specific heat, represents the rate of heat transfer needed to change the temperature of the fluid stream by 1 degree C as it flows through the HX.

$$\begin{aligned} \dot{C}_c &= \dot{m}_c C_{pc} \\ \dot{C}_h &= \dot{m}_h C_{ph} \end{aligned} \tag{4.4}$$

4.7.2 Log-Mean-Temperature-Difference Method

Since the average temperature difference between the two fluids is logarithmic, rather than linear, the log-mean-temperature-difference (LMTD) proves useful. As a requirement, inlet and outlet temperatures from both the hot and cold fluids must be known or be part of the design parameters. The heat transfer rate in the LMTD method can be calculated as [2]:

$$\dot{Q} = U_{HX} A_s \Delta T_{lm} = U_{HX} A_s \frac{\Delta T_1 - \Delta T_2}{\ln(\Delta T_1 / \Delta T_2)} \tag{4.5}$$

where,

$$\begin{aligned} \Delta T_1 &= T_{h,in} - T_{c,out} \\ \Delta T_2 &= T_{h,out} - T_{c,in} \end{aligned} \tag{4.6}$$

The procedure for using the LMTD method is as follows:

- Select the most suitable type of HX for the desired application.
- Determine unknown inlet or outlet temperatures and the heat transfer rate by means of an energy balance analysis.
- Calculate the LMTD, T_{lm}, and correction factor, F.
- Obtain or calculate the HX overall heat transfer coefficient, U_{HX}.
- Calculate the heat transfer surface area A_s.

The task is completed by selecting a HX with a surface area equal or greater than A_s.

4.7.3 Effectiveness-NTU Method

On the other hand, the Effectiveness-NTU method is used when outlet temperatures are not specified. This method is much more complex than the LMTD and is highly dependent on HX geometry and flow arrangement. It is based on the heat transfer effectiveness ε, defined as [2]:

$$\varepsilon = \frac{\dot{Q}}{\dot{Q}_{\max}} = \frac{\text{Actualheattransferrate}}{\text{Maximumpossibleheattransferrate}} \tag{4.7}$$

The actual heat transfer rate can be determined from the energy balance described above. The maximum possible heat transfer rate depends on the maximum temperature difference that can be achieved in a HX,

$$\Delta T_{\max} = T_{h,in} - T_{c,in} \tag{4.8}$$

therefore, the maximum heat transfer rate is:

$$\dot{Q}_{\max} = \dot{C}_{\min} \Delta T_{\max} \tag{4.9}$$

where $\dot{C}_{min}$ is the smallest heat capacitance rate.

Effectiveness relations involve the dimensionless number of transfer units, or NTU. It is expressed as:

$$NTU = \frac{UA_s}{C_{\min}} = \frac{UA_s}{(\dot{m}C_p)_{\min}} \tag{4.10}$$

Another useful dimensionless quantity is the capacity ratio:

$$c = \frac{C_{\min}}{C_{\max}} \tag{4.11}$$

Since the effectiveness-NTU method relies heavily on HX geometry and flow arrangement, several relationships have been developed for determining these quantities and are tabulated below.

There are several factors that need to be taken into account when designing or selecting a suitable HX for a particular application. Some of these are: cost, pumping power, size, weight, type, materials, safety, reliability, and ease of service, among others

[37].

Table 4.1: Effectiveness-NTU relation for several HX types [2]

Heat Exchanger Type	Effectiveness Relation	NTU Relation
1.Double-Pipe		
Parallel Flow	$\varepsilon = \frac{1-e^{-NTU(1+c)}}{1+c}$	$NTU = -\frac{\ln[1-\varepsilon(1+c)]}{1+c}$
Counter Flow	$\varepsilon = \frac{1-e^{-NTU(1-c)}}{1-ce^{-NTU(1-c)}}$	$NTU = \frac{1}{c-1}\ln\left(\frac{\varepsilon-1}{\varepsilon c-1}\right)$
2.Shell-and-tube		
(one shell/even tubes)	$\varepsilon = \frac{2}{\left[1+c+\sqrt{1+c^2}\frac{1+e^{-NTU\sqrt{1+c^2}}}{1-e^{-NTU\sqrt{1+c^2}}}\right]}$	$NTU = -\frac{1}{\sqrt{1+c^2}}\ln\left(\frac{\frac{2}{\varepsilon}-1-c-\sqrt{1+c^2}}{\frac{2}{\varepsilon}-1-c+\sqrt{1+c^2}}\right)$
3.Cross-flow (single)		
C_{max} mixed, C_{min} unmixed	$\varepsilon = \frac{1}{c}\left(1-e^{-c\left(1-e^{-NTU}\right)}\right)$	$NTU = -\ln\left(1+\frac{\ln(1-\varepsilon c)}{c}\right)$
C_{min} mixed, C_{max} unmixed	$\varepsilon = 1-e^{-\frac{1}{c}\left(1-e^{-cNTU}\right)}$	$NTU = -\frac{\ln[c\ln(1-\varepsilon)+1]}{c}$
4.All Heat Exchangers, $c = 0$	$\varepsilon = 1-e^{-NTU}$	$NTU = -\ln(1-\varepsilon)$

4.8 The Thermodynamic Cycle

Upon knowing the outlet temperature of the working fluid, a suitable thermodynamic cycle and electromechanical device can be selected for producing electrical energy. The proposed system is for a 30 MWe output. The Rankine cycle is the most commonly used cycle for electricity generation. The Rankine cycle has been proven to be the ideal cycle for vapor power plants [36, 37]. Since the components of a Rankine cycle (pump, boiler, turbine and condenser) are all steady-flow devices, the cycle can be analyzed through steady-flow equations per unit mass of steam.

Figure 4.9 graphically describes the four processes taking place in a Rankine cy-

cle including: schematic, process description and a Ts curve.

The boiler and condenser do not require or produce any work, and if the pump and turbine are assumed to be isentropic, then the conservation of energy relation yields [35]:

$$w_{pump,in} = h_2 - h_1 = v\,(P_2 - P_1) \tag{4.12}$$

$$q_{in} = h_3 - h_2 \tag{4.13}$$

$$w_{turb,out} = h_3 - h_4 \tag{4.14}$$

$$q_{out} = h_4 - h_1 \tag{4.15}$$

where w stands for the work needed (in) or produced (out) by the pump or turbine. h refers to the enthalpy in each process and, q represents the energy that enters (in) and exits (out) a process.

The thermal efficiency, η_{th}, of the Rankine cycle can be determined from the ratio of net work and the energy that enters the system, namely:

$$\eta_{th} = \frac{w_{net}}{q_{in}} = 1 - \frac{q_{out}}{q_{in}} \tag{4.16}$$

where,

$$w_{net} = q_{in} - q_{out} = w_{turb,out} - w_{pump,in} \tag{4.17}$$

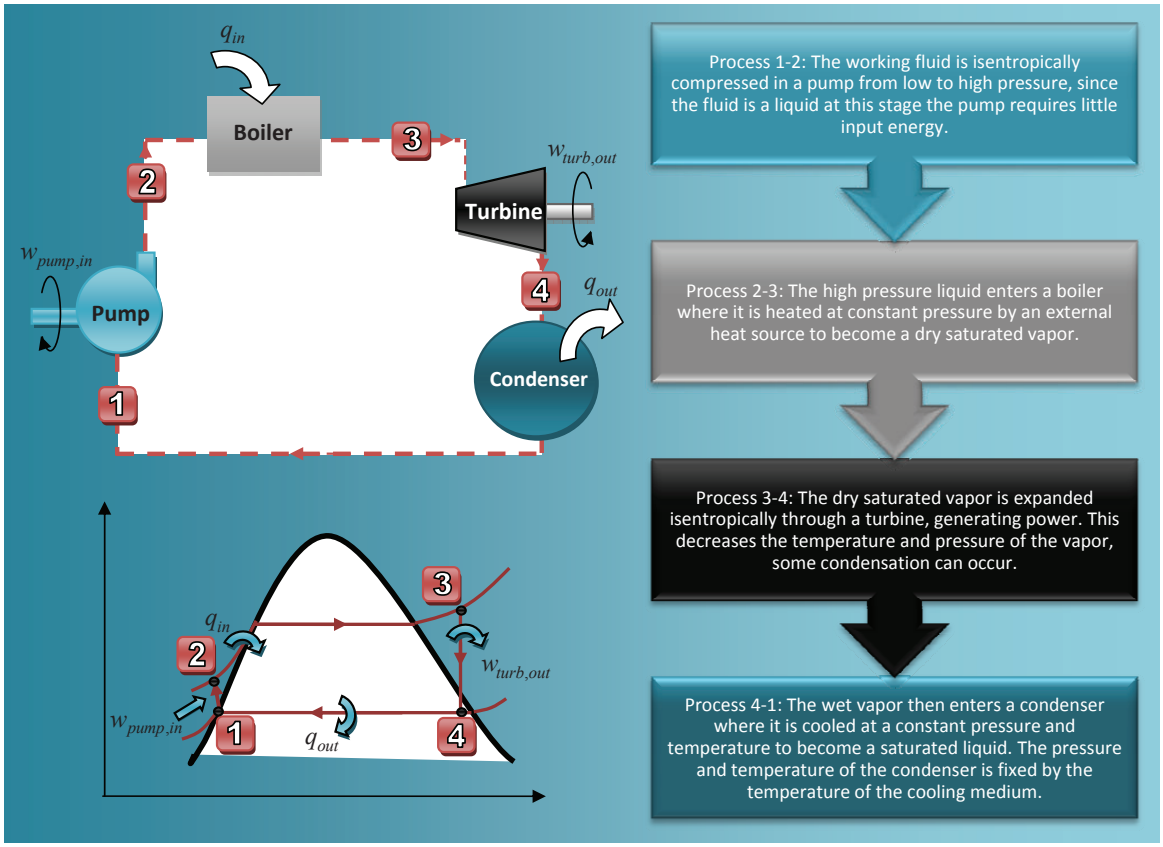

Figure 4.9: Rankine cycle: schematic, process description and Ts diagram

4.9 Thermal Energy Storage (TES) Mediums

Storage and/or hybridization provides the system with the ability of dispatching reliable power at times where solar radiation is low or at night, thus improving the system efficiency and reliability. Storage technology for DSG is currently under study. Some preliminary studies have shown the effectiveness of phase-change materials and molten salts as storage mediums [38, 39]. Hybridization provides the flexibility of attending solar transients during cloudy periods and for extending the operating time of a STPP. Conventional boilers for steam generation or gas turbines are the most widely used hybridization methods.

Since solar thermal power plants suffer the limitation of most renewable technologies, an unpredictable operating profile due to weather variations, they need to overcome two main challenges: how to store the energy collected during the day so it can be used through the night and/or periods of low solar radiation; and how to dispatch this energy when needed. Both of these problems may be solved by coupling a thermal energy storage system with the concentrating solar power segment of the plant [29, 40, 41].

Thermal storage systems aim to: serve as buffers during transient weather conditions, provide dispatchability or time-shifting, increase annual capacity factor and, achieve full load operation of the steam cycle at high efficiency [40].

Storage systems require: high energy density in storage material, good heat transfer between heat transfer fluid and storage medium, mechanical and chemical stability of storage material, and a large number of charging/discharging cycles, low thermal losses, and ease of control [8].

There are several thermal storage technologies that have been proven effective, but not all are suitable for large-scale, solar thermal power applications. Some of the most common ones and their properties are presented in Table 11. The most relevant ones include: chemical storage, battery storage, phase change materials (PCM), and molten salts [10, 12]. Chemical storage has not been used in practical applications, therefore, many questions remain unanswered as to its technical and economic feasibility. Electrical or battery storage, although proven and technically feasible, remains quite expensive. Figure 4.10 summarizes the cost per kWh of the different components required for several storage mediums.

PCMs and Molten salts seem to be the most promising technologies for solar thermal applications and will be described in further detail.

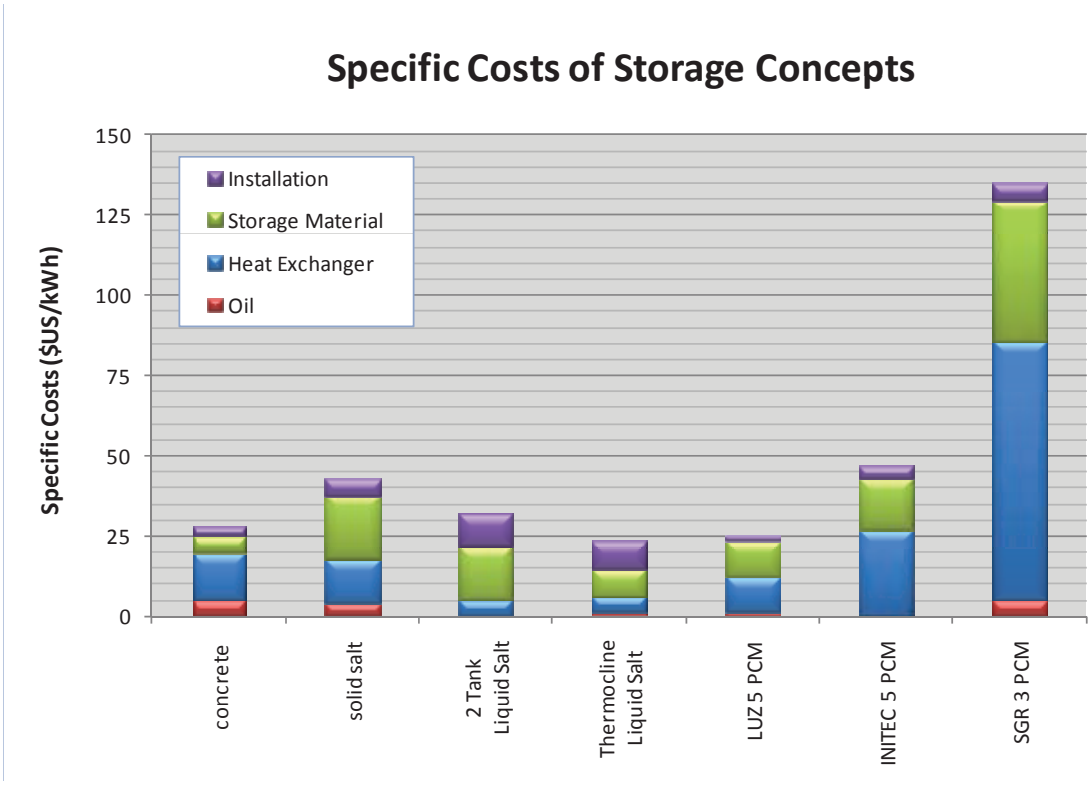

Figure 4.10: Specific costs for different TES Mediums and their components, adapted from [8]

4.9.1 Phase Change Materials (PCMs)

A *phase change material* (PCM) or a "latent" energy storage material is a substance with a high heat of fusion which, if melted and solidified at a certain temperature, is capable of storing and releasing energy. PCMs are also classified as latent heat storage (LHS) units. Latent heat storage can be achieved through solid/solid, solid/liquid, solid/gas and liquid/gas phase change, but the only practical phase change used is the solid/liquid change. Even though liquid/gas phase changes have a higher heat of transformation than solid/liquid transitions, they are not practical due to the large volumes

and high pressures encountered when storing gasses. Solid/solid phase changes are typically very slow and have a rather low heat of transformation [8, 42].

The heat storage process remains in the sensible heat range until the material reaches the temperature at which it changes phase, or its melting point. From there on, it absorbs large amounts of heat at an almost constant temperature until all the material is transformed into liquid. When the temperature around a liquid material drops, it solidifies, releasing stored latent heat. PCMs are available in any temperature, ranging from -5 up to 190 °C. They usually store more heat, per unit volume, than conventional storage materials. PCMs can be classified into two categories: organic and inorganic. Organic phase change materials are rarely used. They are expensive and have average latent heat per unit volume and low density. Most organic PCMs are combustible in nature and have a wider range of melting point. Examples are: paraffin and fatty acids [42].

The main advantages of organic PCMs are: large temperature range availability, they freeze without much supercooling, ability to melt congruently, are self-nucleating, are compatible with conventional construction materials, are chemically stable, have a high heat of fusion, most are safe, non-reactive, and recyclable. Even though they have many advantages, organic PCMs have several noteworthy disadvantages that need to be considered depending on the application [43]. Organic PCMs: have low thermal conductivity in their solid state, require high heat transfer rates during the freezing cycle, their volumetric latent heat storage capacity is low, and are flammable.

Inorganic phase change materials are generally hydrated salt-based materials [44]. They have high volumetric latent heat storage capacity, low cost, and are easily avail-

able. They also have a sharp melting point, high thermal conductivity, high heat of fusion, low volume change, and are non-flammable. On the other hand, their volume change is very high, supercooling poses a problem in solid-liquid transition and nucleating agents are needed after repeated cycling.

An appropriate PCM can be selected based on several criteria involving its thermodynamic, kinetic, and chemical properties, as well as, economic factors. In terms of thermodynamic properties, the PCM should possess: a melting temperature in the desired range of operating temperature, a high latent heat of fusion per unit volume, and also a high specific heat, density, and thermal conductivity. In terms of its kinetic properties, it should have: a high nucleation rate to avoid supercooling and a high rate of crystal growth for heat recovery. The PCM should also be chemically stable, have a reversible freeze/melt cycle, show no degradation after a large number of cycles and be non-corrosive, non-toxic, non-flammable and non-explosive. It should have a low cost and have large-scale availability. Since some PCMs are flammable, they must be selected and applied very carefully, in accordance with fire and building codes and sound engineering practices to avoid the risk of fire or explosion and/or liability, should an accident occur [42, 45, 46].

It is important to acknowledge that even though PCMs are gaining popularity as thermal energy storage mediums, there is not any full-scale working prototype or commercially available PCM TES (Thermal Energy Storage) system. Most of the results available in literature come from small scale experimentation with these substances. The findings assure that PCMs would be a suitable, technically feasible, and economical way to store heat for solar thermal power plants in the near future. Table 4.2 shows PCM materials specific for solar thermal power applications.

Table 4.2: Most commonly used PCMs for Solar Thermal Power Applications. Relative cost based on NaCl at 0.05 $/kg and NaOH at 0.35 $/kg, the resulting storage capacity cost is 2.7 $/kWh [42]

Temp (C)	Composition (mole%)	Tf (C)	Heat of Fusion (kJ/kg)	Relative Cost
367	NaOH, NaCl (20)	370	370	1.001
	KOH	360	167	4.39
347	KNO_3, KBr (10), KCl (10)	342	140	4.04
	NaCl, KCl (24), LiCl (43)	346	281	5.44
328	KNO_3	337	116	3.8
	KNO_3, KCl (6)	320	150	3.33
	NaOH	318	158	2.78
		286-299	3162	1.2
308	NaCl, NaOH (93.7)	314	-	-
	$NaNO_3$	310	174	1.35
	NaF, $NaNO_3$ (96.5)	304	-	-
	LiOH, KOH (60)	314	341	3.57
289	Na_2SO_4, NaCl (8.4), $NaNO_3$ (86.3)	287	176	1.3
	$NaNO_3$, NaCl (6.4)	284	171	1.2
	KNO_3, $Ba(NO_3)_2$ (87)	290	124	2.85
	$NaNO_2$	282	212	3.33
	$NaNO_2$, KNO_3 (45.2)	285	152	3.61
	NaOH, NaCl (7.8), Na_2CO_3 (6.4)	282	316	2.9

4.9.2 Molten Salts

Several studies have been conducted and most conclude that the most advanced thermal energy storage for solar thermal power plants is a two-tank storage system where the heat transfer fluid (HTF) also serves as the storage medium. There is also the option of utilizing a single, thermocline molten salt system, where the hot and cold fluids are separated by a thermal gradient, but requires a much more complex design and operation than the two-tank molten salt TES. The two-tank concept was successfully demonstrated in a commercial trough plant (the 13.8 MWe SEGS I plant with a 120 MWh_t storage capacity) and a demonstration power tower plant (the 10 MWe Solar Two with 105 MWh_t storage capacity) [25, 30]. Because the HTF used in parabolic trough power plants (Therminol VP-1) is expensive, thereby increasing the cost of a HTF storage system, studies were carried out to evaluate an alternative and

less expensive HTF and TES medium. The studies concluded that the specific cost for a two-tank molten salt storage would be in the range of \$30 to \$40/kWh_t depending on storage size [30].

Table 4.3: Oil and molten salt TES systems comparison [3]

	Without Storage	With 2-Tank Thermal Storage		
Case ID	VP-1	VP-1	Salt 450 C	Salt 500 C
Solar Field Size [m^2]	270,320	427,280	425,100	425,100
Invesment Cost [M\$]	110,291	175,251	171,405	164,583
Thermal Storage Cost [M\$]	0	21,330	19,674	14,141
Annual O&M Cost(k\$/year]	3,583	4,088	4,282	4,282
Net Electric [GWh]	107.5	169.2	183.9	185.7
Mean Solar to Electric Efficiency	0.15	14.58	15.92	16.08%
LEC [\$/MWh]	139.7	131.5	119.9	115.1
LEC Reduction	-	5.9	14.2	17.60%
Thermal Storage Cost [\$/kWh_e]	0	64.6	59.6	42.9
Thermal Storage Cost [\$/kWh_t]	0	23.7	23.6	17.4

Table 4.3 summarizes some of the results obtained in regards to a molten salt TES, as opposed to a VP-1 TES, the most important parameter being the Levelized Electricity Cost (LEC), the ratio of capital costs to the plant's energy output.

The following operation strategy is applied to most salt TES systems [41]: The turbine operation will always come before storage charging. This means that only if the thermal energy collected by the solar field exceeds the design value of the steam generator of the Rankine cycle, then the surplus energy is fed into the TES. On the other hand, if additional energy is needed, it will be extracted from the available energy in the TES system. That way, the turbine can be operated at full load with high efficiency even under low radiation conditions. Usually there is no specific operation or discharge profile for the TES system since it would be highly dependent on the system's dynamic behavior. The storage is used in a way that the turbine can be operated at full load as much as possible.

The storage model studied also considered heat losses of the cold and hot storage tanks. Heat loss measurements of the salt storage tanks were done at Solar Two. The study investigated the effects on the storage system if it would be out of operation for several weeks in the winter. The calculation was done with meteorological data from Barstow, CA, using the first 6 weeks of the year. The result: After 6 weeks without charging or discharging the storage, its temperature dropped from around 280 to 250 °C, keeping the salt from reaching its freezing point. This proves the high efficiency of a two-tank molten salt thermal energy storage [41].

Chapter 5

COMPOUND PARABOLIC CONCENTRATOR (CPC) ANALYSIS

5.1 Introduction

The *Compound Parabolic Concentrator* (CPC) was conceived by Prof. Roland Winston in 1966. The technology was developed at the University of Chicago. It is based on his research in the field of non-imaging optics. He came to call it the ideal concentrator and presented the geometrical and mathematical reasons for his claim, in optical terms. Later on, he presented its geometric design and different collector configurations. It was not until 1976 that Ari Rabl [47] presented a detailed heat transfer analysis through a CPC and provided means for evaluating its performance as collector. He was also able to: establish, mathematically, how to determine the effects of truncation, determine the average number of reflections for radiation passing through a 2D CPC, and compared its performance to other types of collectors [48].

The CPC makes use of the fact that when a parabola is tilted at an angle not equal to the direction of the beam radiation, the rays no longer concentrate on its focus; instead, they are reflected in an area above and below the focus, as can be seen in Figure 5.1. If the half parabola that reflects above the focus is discarded and replaced with a similarly shaped parabola reflecting below the focus, the result is a CPC; a concentrator that reflects (traps or funnels) all incoming rays from any angle between the focal line of the two parabola segments [5].

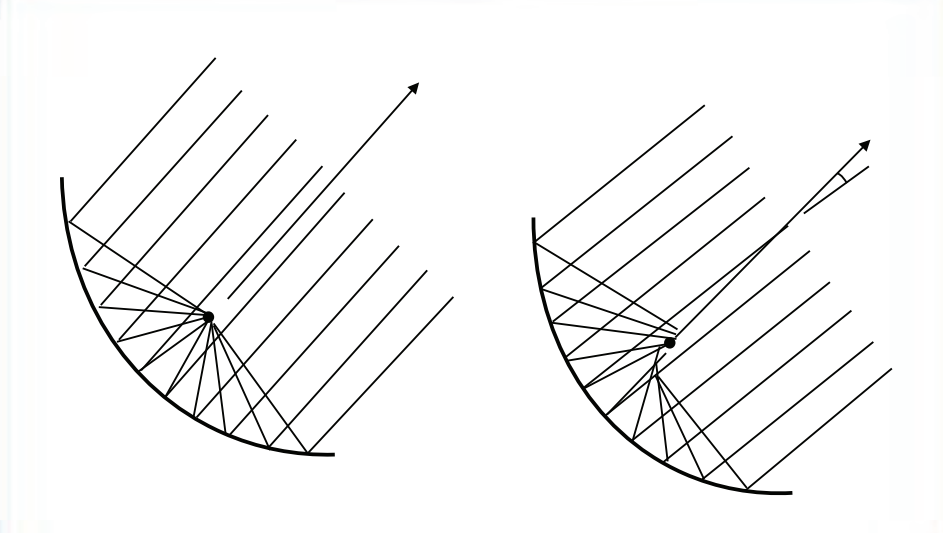

Figure 5.1: Left: Parabola intercepting solar radiation parallel to its axis. Right: Parabola intercepting rays not parallel to its axis

The basic shape of the CPC is illustrated in Figure 5.2. The name derives from the fact that the CPC is formed by two parabolic segments with different focal points. The focal point for parabola A lies on parabola B, and vice versa. The two parabolic surfaces are symmetrical with respect to the reflection through the axis of the CPC. The angle that the axes of the parabola A and B make with axis of the CPC defines the acceptance angle θ of the CPC.

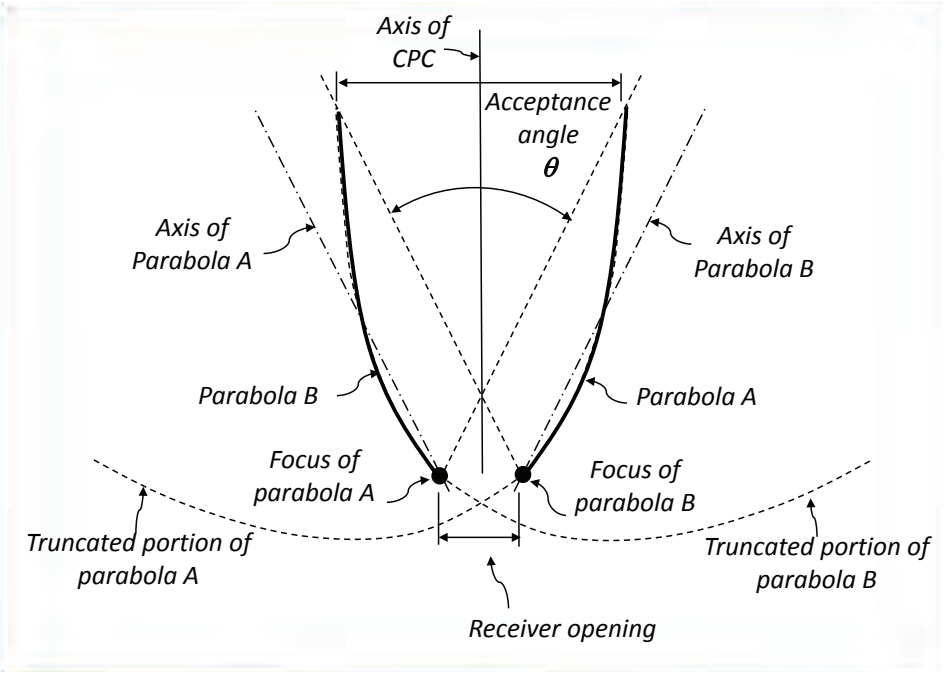

Figure 5.2: Basic shape of a CPC, adapted from [9]

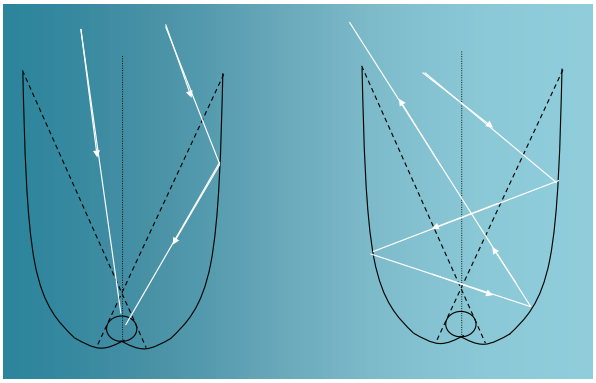

Figure 5.3: Reflection through a CPC, adapted from [9]

A useful term in CPC analysis is the acceptance half-angle, $\theta_{1/2}$, which is the angle between the axis of the CPC and the line connecting the focus of one of the parabolas with the opposite edge of the aperture, or more easily, the acceptance angle divided by two. Radiation with an incidence angle less than the acceptance half-angle will be reflected through the receiver opening, and that with an incidence angle greater than the acceptance half-angle will not be reflected to the receiver opening and will eventually be reflected back out through the aperture of the CPC (Figure 5.3).

Since the incident radiation is no longer concentrated to a single point, the CPC

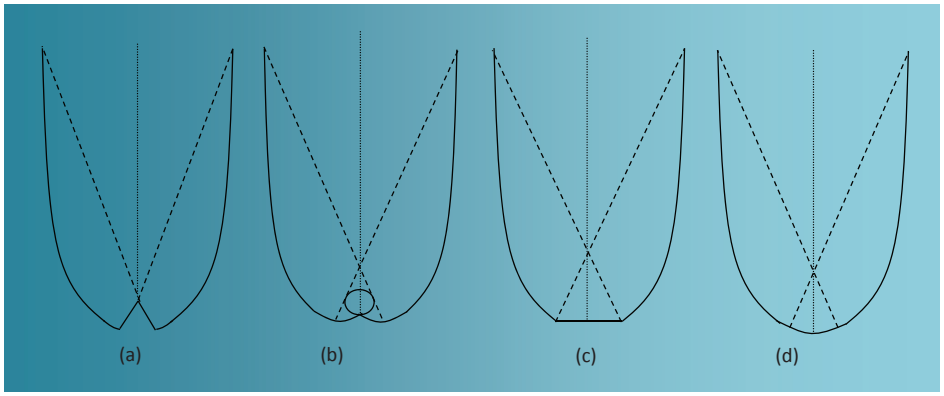

Figure 5.4: Different receiver geometries: (a) wedge, (b) cylindrical, (c) flat and (d) fin, adapted from [9]

can be called a non-imaging concentrator. A receiver placed in the region below the focus produces a concentrator that will accept sun rays coming from any angle between the focal lines of the two parabola segments. Receivers can be of any geometry, as can be seen in Figure 5.4. Flat plates or cylindrical tubes are often used as receivers at the base of the intersection of the two parabolas.

Solargenix Energy has patented a 'Winston Series CPC collector'. It is a collector that focuses sunlight onto a high efficiency absorber tube. The CPC collector is a flat plate, non-evacuated, single pane/glazed panel that measures 4 x 7 feet, mainly used for residential and industrial hot water and space heating applications. This is, so far, the only commercially available product that uses a CPC for solar energy collection. Even though the above mentioned studies discuss the geometry and performance of the CPC in detail, not a single study was encountered that employed this concentrator for power generation. This investigation proposes the use of the CPC trough geometry for electricity production in a solar field, in the same way that a Parabolic Trough is used.

Figure 5.5: CPC troughs (top) and CPC flat-plate collectors (bottom), used with permission, Solargenix

The main advantages for using this non-imaging collector lie on the fact that: it is able to collect both direct and diffuse radiation, it eliminates the need of costly tracking systems (thus reducing parasitic energy consumption), and materials for its construction are less expensive than those used for imaging systems. Before undergoing an optical and thermal analysis of a CPC collector, it must be described mathematically with a coordinate system [47]. Cartesian or polar coordinates can be employed in describing a CPC. The following discussion is based on Cartesian coordinates and in Figure 5.6.

The right branch of the CPC in the coordinate system shown satisfies the equation [47]:

$$y = \frac{x^2}{2s(1 + \sin\theta_{1/2})} \tag{5.1}$$

where s refers to the absorber. Its end points are:

$$x_S = s\cos\theta_{1/2}; y_S = \frac{s}{2}(1 - \sin\theta_{1/2}) \tag{5.2}$$

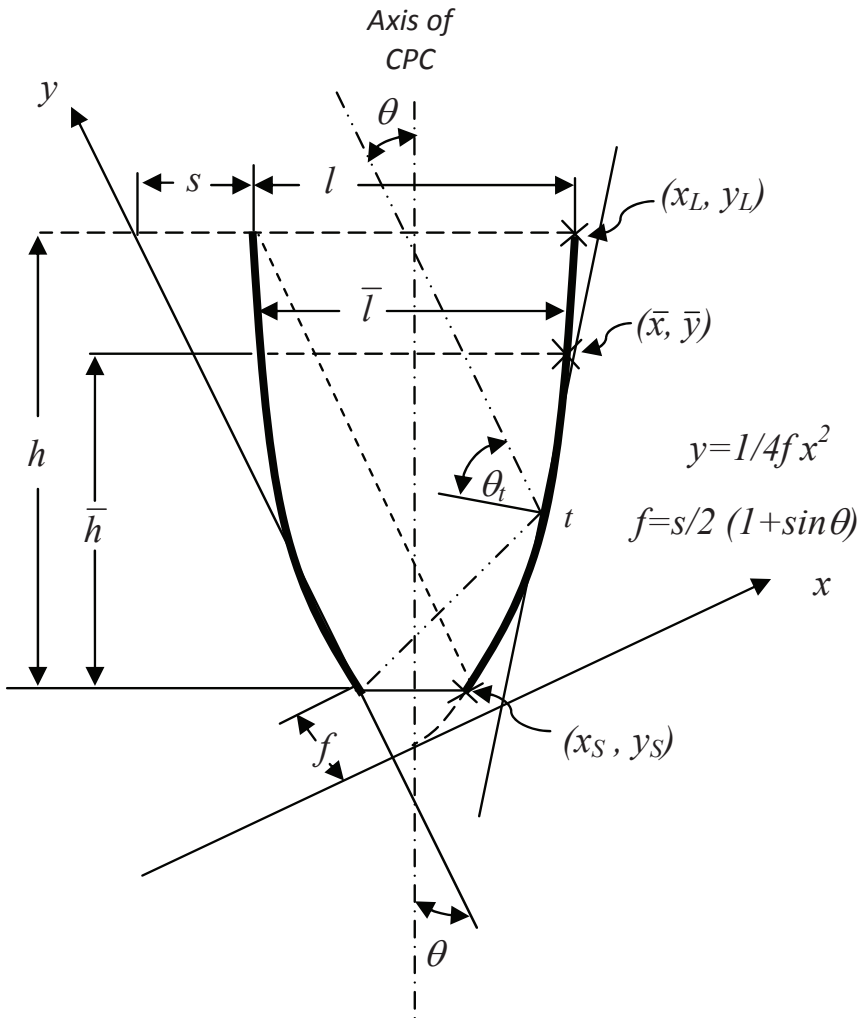

Figure 5.6: A CPC with relation to a Cartesian coordinate system; barred variables correspond to truncated values, adapted from [47]

and

$$x_L = (s+l)\cos\theta_{1/2}; y_L = \frac{s}{2}(1-\sin\theta_{1/2})\left(1+\frac{1}{\sin\theta_{1/2}}\right)^2 \tag{5.3}$$

where l is the aperture width.

If the arc length along the curve is measured by the parameter t, then the reflector area per unit trough length is

$$A_{ref} = 2\int_{t_{receiver}}^{t_{aper}} dt \tag{5.4}$$

with

$$dt = \sqrt{1+\left(\frac{x}{s(1+\sin\theta_{1/2})}\right)^2} \tag{5.5}$$

which on integration yields:

$$A_{ref} = A_{receiver}\left(1+\sin\theta_{1/2}\right)\left(\begin{array}{l}\dfrac{\cos\theta_{1/2}}{\sin^2\theta_{1/2}} + \ln\dfrac{\left(1+\sin\theta_{1/2}\right)\left(1+\cos\theta_{1/2}\right)}{\sin\theta_{1/2}\left(\cos\theta_{1/2}+\sqrt{2\left(1+\sin\theta_{1/2}\right)}\right)} \\ -\dfrac{\sqrt{2}\cos\theta_{1/2}}{\left(1+\sin\theta_{1/2}\right)^{3/2}}\end{array}\right) \tag{5.6}$$

where $A_{receiver}$ is the receiver or absorber area.

5.2 Optical Characteristics and Performance Analysis of CPC Collectors

Since the density of solar radiation incident on the Earth's surface is rather low, the only means to harvest it for electricity generation is through concentration. The concentration ratio (CR) of a collector can be stated as the ratio of the input aperture

area A_{aper} (top area of the concentrator that intercepts solar radiation), to the exit aperture area $A_{receiver}$ (area where the reflecting surface of the concentrator collects or focuses radiation).

$$CR = \frac{A_{aper}}{A_{receiver}} \tag{5.7}$$

The problem strives in what could be the maximum attainable concentration ratio that can be obtained theoretically. Winston [20] analyzed this problem, and based on the Second Law of Thermodynamics found that:

$$CR = \frac{n_{ref}}{\sin\theta_{1/2}} \tag{5.8}$$

where n_{ref} is the index of refraction that can be approximated to 1 for air as a medium. For a derivation of this result see Duffie [10].

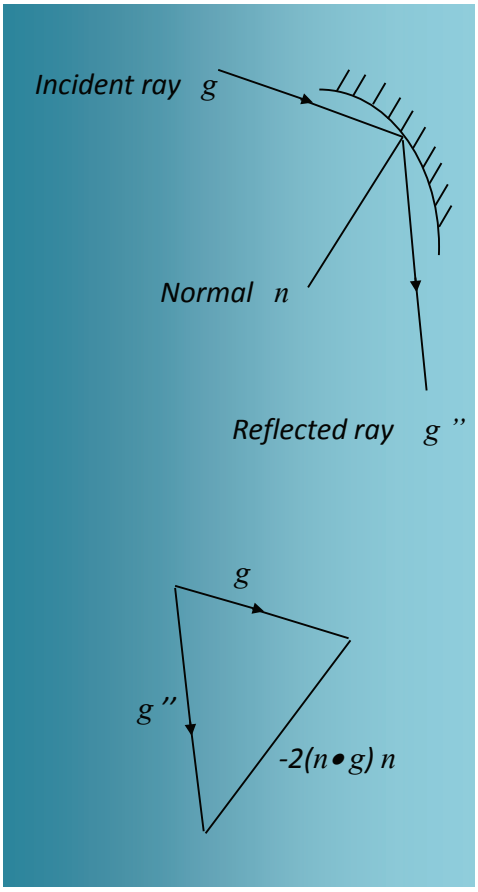

Figure 5.7: Snell's Law of reflection and refraction

The optical performance of a CPC depends on whether the incident solar radiation is within the acceptance half-angle, as stated before. This is best understood through the use of ray-tracing diagrams. The ray tracing procedure is based on the Snell's Law principle of incidence and reflection. This is basically a problem of geometry. To ray-trace a reflecting surface one must know the direction of the incoming ray and identify its point of incidence on the surface. Once the normal of the surface at the point of incidence is determined, the angle it makes with the incoming

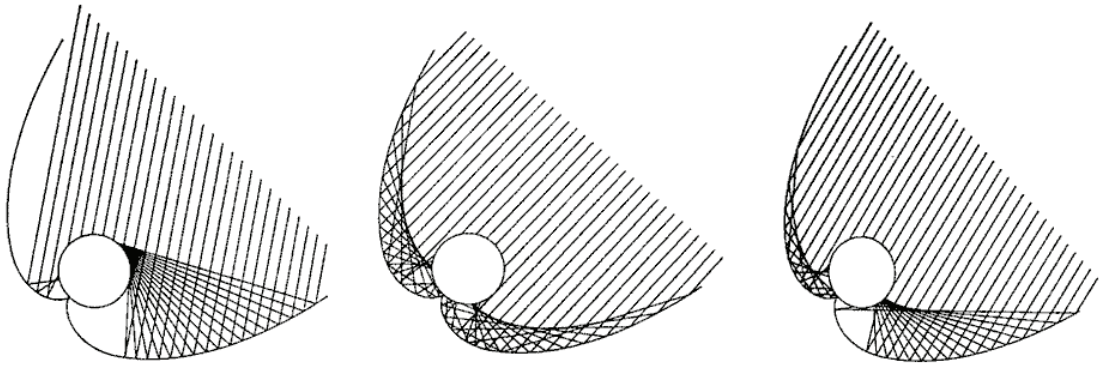

Figure 5.8: CPC ray-tracing diagrams, adapted from [10]

ray will be the same at which the reflected ray will leave the surface, as can be seen in Figure 5.7. This process is repeated if several reflections are to be considered [5].

It can also be stated in vector form as:

$$\mathrm{g}'' = \mathrm{g} - 2(n \cdot \mathrm{g})n \tag{5.9}$$

where g , g$''$ and n are the incident ray, reflected ray and the normal, respectively.

A CPC's optical efficiency can be found by calculating the average number of reflections, $\langle n \rangle_i$, that radiation undergoes between the input aperture and the absorber or exit aperture, whichever is the case [47]. The average number of reflections can be obtained by studying how the radiation that arrives at the collector travels between the absorber, reflector walls, and if outside the acceptance angle, the radiation that comes back out of the CPC without being absorbed. Going back to Figure 5.3, it can be seen that normally incident radiation in the central region of the entrance aperture will undergo no reflections between the entrance aperture and absorber. If however, radiation enters near the edges of the inlet aperture, it undergoes one or more reflec-

tions. The average number of reflections is an important parameter and is defined as the average taken over all radiation entering the entrance aperture. The attenuation of radiation then corresponds to $\rho_{CPC}^{\langle n \rangle_i}$, where ρ_{CPC} is the specular CPC surface reflectance.

The average number of reflections is dependent on the CPC's acceptance half-angle, reflector area, absorber area, and the fraction of the radiation emitted by the reflector that reaches the absorber, E_d. This fraction can be determined from Figure 5.6 as:

$$\begin{aligned} E_d &= \frac{2}{A_{ref}} \int_{t_{receiver}}^{t_{aper}} \frac{1}{2} \left(1 - \sin\theta_{1/2}\right) dt \\ &= \frac{1}{2} \left(1 - \frac{A_{aper}}{A_{ref}} \frac{\left(1 - \sin\theta_{1/2}\right)\left(1 + 2\sin\theta_{1/2}\right)}{\sin\theta_{1/2}} \right) \end{aligned} \tag{5.10}$$

where the subscripts $aper$, ref and $receiver$ denote aperture, reflector, and absorber, respectively. Conversely, the fraction of the radiation emitted by the reflector wall that does not reach the absorber and escapes the concentrator through the aperture, E_o, is defined as:

$$E_o = \frac{A_{aper}}{A_{ref}} \left(\frac{\left(1 - \sin\theta_{1/2}\right)\left(1 + 2\sin\theta_{1/2}\right)}{\sin\theta_{1/2}} \right) \tag{5.11}$$

These quantities can be related to the average number of reflections for the radiation passing through a CPC inside and outside of its acceptance angle. In most studies, the variation of $\langle n \rangle_i$ is neglected for most engineering designs and is given a value of one. This approach greatly reduces the CPC's optical efficiency since it depends on the reflectance elevated to the power of $\langle n \rangle_i$. Rabl [47] defines the average number of reflections inside the acceptance angle of the CPC as:

$$\langle n \rangle_i = \frac{A_{ref}}{A_{receiver}} E_d \tag{5.12}$$

and for that outside,

$$\langle n \rangle_o = \frac{A_{ref}}{A_{aper} - A_{receiver}} E_o \tag{5.13}$$

By algebraically manipulating the relationships that lead to the average number of reflections inside and outside, it can be shown that they only depend on the CPC's acceptance half-angle.

$$\langle n \rangle_i = \frac{1}{2}\left(1 + \sin\theta_{1/2}\right)\left(\frac{\cos\theta_{1/2}}{\sin^2\theta_{1/2}} + \ln\frac{\left(1+\sin\theta_{1/2}\right)\left(1+\cos\theta_{1/2}\right)}{\sin\theta_{1/2}\left(\cos\theta_{1/2} + \sqrt{2\left(1+\sin\theta_{1/2}\right)}\right)} - \frac{\sqrt{2}\cos\theta_{1/2}}{\left(1+\sin\theta_{1/2}\right)^{3/2}}\right) - \frac{\left(1-\sin\theta_{1/2}\right)\left(1+2\sin\theta_{1/2}\right)}{2\sin^2\theta_{1/2}} \tag{5.14}$$

$$\langle n \rangle_o = \frac{A_{ref}}{A_{aper} - A_{receiver}} E_o \langle n \rangle_o = 2 + \frac{1}{\sin\theta_{1/2}} \tag{5.15}$$

Thus, the optical efficiency of a CPC collector can be defined as:

$$\eta_o = \tau_{CPC}\tau_r\alpha_r\varphi \tag{5.16}$$

where τ_r and α_r are the receiver transmittance and absorptivity, respectively, where:

$$\tau_{CPC} = \rho_{CPC}^{\langle n \rangle_i} \tag{5.17}$$

$$\varphi = \frac{I_b + I_d CR}{I_t} \tag{5.18}$$

I represents hourly radiation, and the subscripts b, d, and t refer to beam, diffuse, and total, respectively.

5.3 Truncation Analysis of CPC Collectors

The only considerable disadvantage of a CPC is that it is too deep compared to a simple parabola. It requires a rather large reflector area for a given aperture. However, a large portion of the top of a CPC can be cut off or truncated with almost no loss in its concentration ratio [9, 47]. In practical applications, a CPC will almost always be truncated for economic reasons. Truncation is, therefore, of great importance when designing CPC collectors because it reduces collector area and the average number of reflections, thereby improving their optical efficiency and reducing costs.

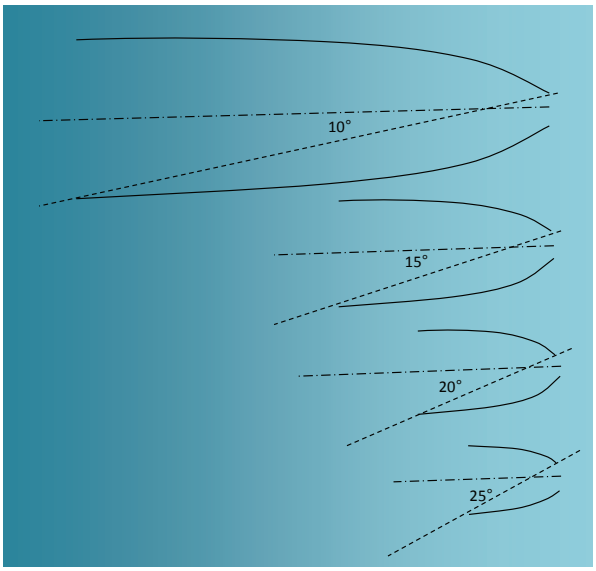

Figure 5.9: CPCs with different acceptance angles. The drawings are to scale with the exit apertures all equal in diameter, redrawn from [10]

Truncation in a CPC is best explained by basing the analysis on a Cartesian coordinate system as that presented in Figure 5.6. The barred quantities represent truncated values or measurements. The CPC is said to be truncated if the right half of the CPC ends at point $(\bar{x}, \bar{y})$, instead of the endpoint (x_L, y_L). The left side is also truncated to maintain symmetry, but the absorber width, s, is kept fixed. Figure 5.9 shows some CPCs with different acceptance angles that have the same exit apertures. The depth increases with a decrease in acceptance angle.

For solar applications, the acceptance angles must be small enough to obtain higher concentration ratios, resulting in deeper CPCs with large reflector areas. Rabl [47] derived several equations for all the parameters of interest in CPC truncation. The

barred values indicate a truncated CPC. The length of the aperture can be given by :

$$\bar{l} = 2\bar{x}\cos\theta_{1/2} - \frac{\bar{x}^2}{s\left(1+\sin\theta_{1/2}\right)}\sin\theta_{1/2} + s\left(\sin\theta_{1/2} - \cos^2\theta_{1/2}\right) \tag{5.19}$$

where s is the absorber width, and $\theta_{1/2}$ is the acceptance half angle of the full CPC. The depth or the distance from absorber to aperture is:

$$\bar{h} = \bar{x}\sin\theta_{1/2} - \frac{\bar{x}^2\cos\theta_{1/2}}{2s\left(1+\sin\theta_{1/2}\right)} - \frac{s}{2}\cos\theta_{1/2}\left(1+\sin\theta_{1/2}\right) \tag{5.20}$$

The height can be stated as a fraction of the original height:

$$h = \frac{s}{2}\left(1+\frac{1}{\sin\theta_{1/2}}\right)\cot\theta_{1/2} \tag{5.21}$$

and equation 5.20 can be solved for:

$$\bar{x} = s\frac{\left(1+\sin\theta_{1/2}\right)}{\cos\theta_{1/2}}\left[-\sin\theta_{1/2} + \left(1+\frac{\bar{h}}{h}\cot^2\theta_{1/2}\right)^{1/2}\right] \tag{5.22}$$

Thus, the result for the truncated reflector area is:

$$\begin{aligned}\frac{\bar{A}_{ref}}{A_{receiver}} = \left(1+\sin\theta_{1/2}\right)\ln\left[\frac{\frac{\bar{x}}{s}+\sqrt{\left(1+\sin\theta_{1/2}\right)^2+\left(\frac{\bar{x}}{s}\right)^2}}{\cos\theta_{1/2}+\sqrt{2\left(1+\sin\theta_{1/2}\right)}}\right] + \\ \frac{\bar{x}}{s}\sqrt{1+\left(\frac{\bar{x}}{s\left(1+\sin\theta_{1/2}\right)}\right)^2} \\ -\frac{\sqrt{2}\cos\theta_{1/2}}{\sqrt{1+\sin\theta_{1/2}}}\end{aligned} \tag{5.23}$$

These equations must be solved simultaneously.

The average number of reflections inside the acceptance angle for a truncated CPC

is:

$$\langle \bar{n} \rangle_i = \frac{\bar{A}_{ref}}{A_{receiver}} \bar{E}_i \tag{5.24}$$

where,

$$\bar{E}_i = \frac{1}{2} - \frac{1}{\bar{A}_{ref}} \frac{\bar{x}^2 - x_S^2}{2s\left(1 + \sin\theta_{1/2}\right)} \tag{5.25}$$

The average number of reflections outside the acceptance angle is:

$$\langle \bar{n} \rangle_o = 1 - \sin\theta_{1/2} \left(\frac{\bar{A}_{ref}}{\bar{A}_{aper}} \left(1 - \bar{E}_i\right) - \langle \bar{n} \rangle_i \right) + \langle \bar{n} \rangle_i \tag{5.26}$$

Rabl [47] created charts for calculating the different parameters involving CPC truncation for some common acceptance half-angles used. The problem strives in that the graphics are somewhat difficult to read with a high degree of accuracy. For accurate values, the system of equations must be solved and graphed.

After having studied all the pertinent factors regarding the optical performance of a CPC collector, its absorbed radiation per unit area of collector aperture, S, can be estimated as [10, 49]:

$$S = A_{aper} \tau_{CPC} \alpha_{CPC} \left(I_{b,CPC} + I_{d,CPC} \right) \tag{5.27}$$

where,

$$I_{b,CPC} = F I_{bn} \cos\theta_{1/2} \tag{5.28}$$

$$I_{d,CPC} = \begin{cases} \frac{I_d}{CR} & if(\beta + \theta_{1/2}) < 90^\circ \\ \frac{I_d}{2}\left(\frac{1}{CR} + \cos\beta\right) & if(\beta + \theta_{1/2}) > 90^\circ \end{cases} \tag{5.29}$$

$$I_{g,CPC} = \begin{cases} 0 & if(\beta + \theta_{1/2}) < 90° \\ \frac{I_d}{2}\left(\frac{1}{CR} - \cos\beta\right) & if(\beta + \theta_{1/2}) > 90° \end{cases} \tag{5.30}$$

$$\left(\beta - \theta_{1/2}\right) \leq \tan^{-1}\left(\tan\theta_z \cos\gamma_s\right) \leq \left(\beta + \theta_{1/2}\right) \tag{5.31}$$

F is a control function. It has a value of 1 if the beam radiation is incident on the CPC, and zero if it is not. β is the slope angle the axis of the CPC makes with the zenith, as can be seen in Figure 5.10.

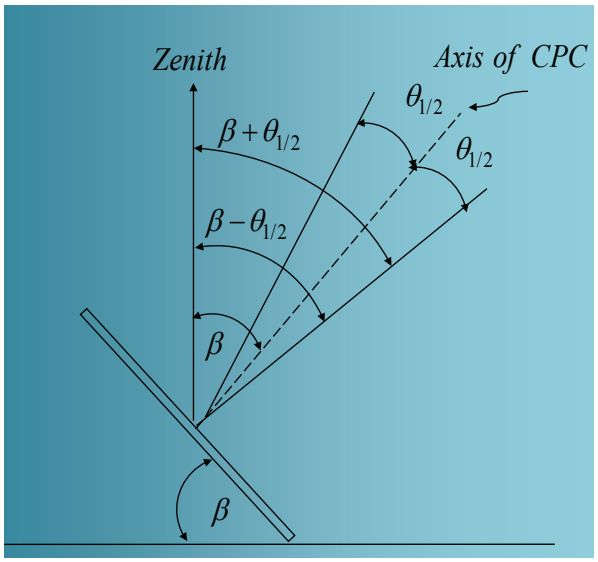

Figure 5.10: Relationship between the acceptance half-angle and the slope angle of a CPC for determining the incidence of beam radiation, redrawn from [10]

Chapter 6

ENERGY BALANCE CALCULATIONS

6.1 Thermal Performance Analysis of CPC Collectors

Calculation of the thermal performance of concentrating collectors can be derived from that of flat-plate collectors. The absorbed radiation per unit area of aperture must be estimated from the radiation available, and from the optical characteristics of both collector and receiver [50]. Thermal losses from receivers must take into account its precise shape and design; and are taken into consideration by deriving a loss coefficient based on receiver area. The temperature gradients along the receiver are taken into account by calculating the flow factor to allow the use of inlet fluid temperatures in energy balance calculations. Ultimately, the collector's efficiency factor and thermal efficiency are obtained through its useful gain [10, 12].

One significant difference between flat-plate and concentrating collectors is the

higher operation temperatures of concentrating collectors. These high temperatures make the loss coefficient be more temperature dependent.

6.2 Loss Coefficient Calculations with Temperature Variation and Collector Efficiency

The loss coefficient can be calculated from the following relationship if Q_{loss}, the receiver area $A_{receiver}$ and the ΔT is known [10]:

$$\begin{aligned}\frac{Q_{loss}}{A_{receiver}} &= h_w\left(T_r - T_a\right) + \varepsilon\sigma T_r^4 - T_{sky}^4 + U_{cond}\left(T_r - T_a\right) \\ &= \left(h_w + h_r + U_{cond}\right)\left(T_r - T_a\right) \\ &= U_L\left(T_r - T_a\right) \\ U_L &= \frac{Q_{loss}}{A_{receiver}\left(T_r - T_a\right)}\end{aligned} \tag{6.1}$$

where T refers to temperature, and the subscripts r and a indicate receiver and ambient, respectively. Thus, for obtaining U_L , all the other factors in equation 6.1 must be known.

Duffie [10] presents a method for obtaining Q_{loss} by iteration. He states that for a collector of certain length, the heat transfer from the receiver (at T_r) to the inside of the cover (at T_{ci}), through the cover (at T_{co}) and then to the surroundings (at T_a and T_{sky}) is given by the following relationships:

$$Q_{loss} = \frac{2\pi k_{eff} L}{\ln\left(\frac{D_{ci}}{D_r}\right)}\left(T_r - T_{ci}\right) + \frac{\pi D_r L\sigma\left(T_r^4 - T_{ci}^4\right)}{\frac{1}{\varepsilon_r} + \frac{1-\varepsilon_c}{\varepsilon_c}\left(\frac{D_r}{D_{ci}}\right)} \tag{6.2}$$

$$Q_{loss} = \frac{2\pi k_c L}{\ln\left(\frac{D_{co}}{D_{ci}}\right)} \left(T_{ci} - T_{co}\right) \tag{6.3}$$

$$Q_{loss} = \pi D_{co} L h_w \left(T_{co} - T_a\right) + \varepsilon_c \pi D_{co} L \sigma \left(T_{co}^4 - T_{sky}^4\right) \tag{6.4}$$

D refers to diameter, L to length, T to temperature and ε to emissivity. The subscripts r, ci, co, and a represent the receiver, inner cover, outside cover, and ambient, respectively. If the annulus is evacuated so that convection is suppressed, k_{eff} can be zero. The outside convective coefficient, h_w, is calculated by simultaneously solving the following equations:

$$\begin{aligned} Nu &= 0.3\,\mathrm{Re}^{0.6} \\ Nu &= \frac{h_w D_{co}}{k} \end{aligned} \tag{6.5}$$

where k is the thermal conductivity, and R_e is the Reynolds number that can be calculated from:

$$\mathrm{R_e} = \frac{\rho V D}{\mu} \tag{6.6}$$

ρ is the density of the medium, V is the wind velocity, and μ is the dynamic viscosity.

The procedure for solving the preceding equations by iteration is carried out by estimating T_{co}, then calculating Q_{loss} from 6.4 and substituting this value in 6.3 to find an estimate of T_{ci}, then 6.2 checks the guess of T_{co}, comparing the calculated Q_{loss} from 6.4 and 6.2.

The loss coefficient variation with temperature can be found by calculating it within the range of the operating temperatures expected in the system, as it will be seen in Chapter 7.

After obtaining the loss coefficient, the overall heat transfer coefficient, U_o, can be calculated, provided that the receiver's thermal conductivity (k_r) and inner (D_i) and outer (D_o) diameters are known, along with the heat transfer coefficient inside the tube (h_{fi}).

$$U_o = \left[U_L^{-1} + \frac{D_o}{h_{fi} D_i} + \left(\frac{D_o}{2k_r} \ln \left(\frac{D_o}{D_i} \right) \right) \right]^{-1} \tag{6.7}$$

The collector's efficiency and flow factors are determined from equations 6.1 and 6.7, respectively:

$$\begin{aligned} F' &= \frac{U_o}{U_L} \\ &= \frac{U_L^{-1}}{U_L^{-1} + \frac{D_o}{h_{fi} D_i} + \left(\frac{D_o}{2k_r} \ln \left(\frac{D_o}{D_i} \right) \right)} \end{aligned} \tag{6.8}$$

$$\begin{aligned} F'' &= \frac{F_R}{F'} \\ &= \frac{mC_pCR}{A_{receiver} U_L F'} \left[1 - \exp \left(- \frac{A_{receiver} U_L F'}{mC_pCR} \right) \right] \end{aligned} \tag{6.9}$$

where $\dot{m}$ is the mass flow rate and C_p is the specific heat of the fluid.

The collector's useful gain is then:

$$Q_u = F_R A_{aper} \left[S - \frac{A_{receiver}}{A_{aper}} U_L \left(T_i - T_a \right) \right] \tag{6.10}$$

where S is the absorbed radiation per unit area of collector aperture.

After having calculated the collector's useful gain, the fluid temperature rise is found from:

$$\Delta T = \frac{Q_u}{\dot{m} C_p} \tag{6.11}$$

and the exit fluid temperature is:

$$T_f = T_i + \Delta T \tag{6.12}$$

thus, the average temperature drop from the receiver surface to the fluid is:

$$T_{ro_{avg}} - T_{f_{avg}} = Q_u \left[\frac{1}{\pi D_{ro} L h_{fi}} + \frac{\ln\left(\frac{D_{ro}}{D_{ri}}\right)}{2\pi k_r L} \right] \tag{6.13}$$

Finally, the collector's thermal efficiency can be stated as:

$$\eta_{col} = \frac{Q_u}{I_t A_{aper}} \tag{6.14}$$

6.3 Fluid Heat Transfer Coefficient and Pressure Drop Calculations in the Absorbers

6.3.1 Fluid Heat Transfer Coefficient

Although fluid properties do change with variations in temperature, it is always advisable to work with average fluid heat transfer coefficient values depending on the temperature range expected in the system [2, 10]. The following equations help determine the fluid heat transfer coefficient. Calculations will be presented in Chapter 7 further on [34].

$$h = \frac{N_u k}{d} \tag{6.15}$$

where, d is the pipe diameter, N_u is the Nusselt Number and can be calculated from the following correlation:

$$N_u = 0.025 R_e^{0.79} P_r^{0.42} p \tag{6.16}$$

Assuming p=1.023, P_r is the Prandtl Number obtained from:

$$P_r = \frac{\mu C_p}{k} \tag{6.17}$$

where, μ, C_p, and k are the fluid's viscosity, its specific heat, and its conductivity, respectively.

6.3.2 Pressure Drop Calculations

Pressure drop calculations are of importance in determining the pumping requirements of the system pump(s) to maintain the flow [51]. The equation for pressure drop employs the dimensionless friction factor, f, and is defined as the pressure drop over a pipe length, L, of one internal pipe diameter, D, divided by the kinetic power of the flow or:

$$\Delta P = f \frac{L}{D} \frac{\rho {V_m}^2}{2} \tag{6.18}$$

where ρ is the density and, V_m, the mean fluid velocity.

For single-phase flow, pipe flow can be laminar, transitional, or fully turbulent. For the laminar flow case, the friction factor is determined from:

$$f = \frac{64}{R_e} \tag{6.19}$$

where R_e can be calculated from:

$$R_e = \frac{V_m D}{v} \tag{6.20}$$

v represents the fluid's kinematic viscosity.

This laminar flow relationship is valid up to around $R_e < 3000$. Once the Reynolds number rises above this, pressure drop becomes dependent on pipe roughness. For the case where the pipe roughness is negligible, the smooth pipe Petukhov correlation is:

$$f = [0.79 \ln R_e - 1.64]^{-2} \tag{6.21}$$

Table 6.1: Roughness values for different pipe materials [4]

Surface	Roughness (10^{-3} m)
Copper, Lead, Brass, Aluminum (new)	0.001 - 0.002
PVC and Plastic Pipes	0.0015 - 0.007
Epoxy, Vinyl Ester and Isophthalic pipe	0.005
Stainless steel	0.015
Steel commercial pipe	0.045 - 0.09
Stretched steel	0.015
Weld steel	0.045
Galvanized steel	0.15
Rusted steel (corrosion)	0.15 - 4
New cast iron	0.25 - 0.8
Worn cast iron	0.8 - 1.5
Rusty cast iron	1.5 - 2.5
Sheet or asphalted cast iron	0.01 - 0.015
Smoothed cement	0.3
Ordinary concrete	0.3 - 1
Coarse concrete	0.3 - 5
Well planed wood	0.18 - 0.9
Ordinary wood	5

The friction coefficient, f, used to calculate pressure loss in rough pipes can be

calculated with the Colebrook equation:

$$f = \frac{1}{-0.86 \ln\left(\frac{r}{3.7d} + \frac{2.51}{R_e f^{0.5}}\right)} \tag{6.22}$$

where, f is the D'Arcy-Weisbach friction coefficient, Re is the Reynolds Number, r is the roughness of the pipe and d, the hydraulic diameter. The Colebrook equation is only valid at turbulent flow conditions and since the friction coefficient is involved on both sides of the equation, it must be solved by iteration until its value stops changing according to a chosen tolerance.

6.4 Thermal Energy Storage (TES) Analysis

As has been explained, thermal energy storage systems greatly improve solar system performance, dispatchability and capacity factor. As can be found in literature, the most advanced thermal energy storage for solar thermal power plants is a two-tank storage system where the heat transfer fluid (HTF) also serves as storage medium. This concept was successfully demonstrated in a commercial trough plant (the 14 MWe SEGS I plant with a 120 MWh_t storage capacity) and a demonstration tower plant (the 10 MWe Solar Two with 105 MWh_t storage capacity) [25].

Solar Two provided all the necessary technological aspects of a storage system of this nature. It ran from 1994 to 1999 and was constructed merely to prove the technology. It was decommissioned later on. It was a very versatile plant. It was originally constructed as a 50 MWe plant with 4 hours of thermal storage using solar salt both as the HTF, and as the storage medium. This plant was also able to provide a 10 MWe output while storing the remaining thermal energy received by the collection system;

the result: A solar thermal power plant that could produce 10 MWe around the clock for 24 hours, supplying energy from the storage system after the sun went down. It provided a challenging feat, but it was able to produce electricity around the clock for a little over a week, once again establishing the technical feasibility of this technology [52].

Storage system analysis basically relies on an energy balance calculation, provided the operating temperatures from the storage fluid are known or can be specified as design parameters. The storage capacity can be obtained from:

$$Q_{sto} = \dot{m} C_p \Delta T_{sto} = \dot{m} C_p (T_{shot} - T_{scold}) \tag{6.23}$$

where $\dot{m}$, C_p, and ΔT_{sto} refer to the mass flow rate, heat capacity, and temperature difference in the storage medium (T_{shot} and T_{scold} being the storage temperature medium in the hot and cold tanks), respectively.

Knowing two of the following parameters: mass flow rate, mass of fluid, or desired storage time, the other parameter can be calculated from the following:

$$t_{storage} = \frac{m}{\dot{m}} \tag{6.24}$$

Chapter 7

PROPOSED SOLAR THERMAL POWER PLANT FOR PR

After having studied and collected information regarding all aspects and components of a STPP and local solar radiation, what has been identified as the most suitable for Puerto Rico consists of the following: A concentrating linear and non-imaging collector array consisting of compound parabolic concentrators, as opposed to the parabolic concentrator most commonly used, steel cylindrical absorbers enclosed in evacuated glass tubes, and molten salt, particularly Solar Salt, as the HTF medium.

The proposed system was selected according to studies made by R. Winston [20, 9, 53], A. Rabl [54, 48, 47, 55, 56, 57] and others, mostly in the late 1970's. The reason investigators and researchers got interested in solar energy in the early 80's was the drive to alternate methods of energy production during the oil embargo and the soaring prices of fossil fuels at that time. Once the oil prices returned to normal in the late 1980's, solar thermal technologies were soon forgotten, until the recent and steep climb in oil prices in the 2000's. STPPs are regaining their place as a clean, renewable, and

affordable method for producing electricity. Because of this, more recent studies can be found with the distinct difference that great advancements in technology are producing far better materials, with much greater performances than those studied in the 70's [58].

Even though further research needs to be done, the proposed system, due to its non-imaging and optic properties, can reach higher concentration ratios than most solar collectors used today. It also does not need a sophisticated control system to track the sun, reducing its cost and complexity. Its non-imaging property greatly benefits this implementation in P.R. due to the fact that CPC's can concentrate and utilize the diffuse component of solar radiation, which is abundant in tropical regions.

From what has been learned through the extent of this research, the use of the non-imaging compound parabolic concentrator for utility range STPP trough has not yet been implemented. As has been discussed before, extensive study must be done to obtain a collector's optical and thermal performance for designing a STPP. The design was divided in several modules:

7.1 Optical and Truncation Analysis

Even though the CPC is capable of attaining high levels of concentration, this comes with a drawback. The smaller the acceptance half-angle, the higher the concentration ratio, but there will be the need to make adjustments in the slope of the CPC even on a daily basis to compensate for the smaller angle. There is also another drawback: the smaller the acceptance half-angle, the deeper the CPC, thus greatly increasing the collector's cost in terms of the quantity of material used. There is no way of optimizing the acceptance half-angle. The designer must select some sort of criterion for choosing

the acceptance half-angle or the level of concentration required.

For this investigation, an acceptance half-angle of 15 ° was chosen. The criterion for selecting this angle was the need for seasonal adjustment of the CPC collector array. As will be shown, with a 15 ° angle, there is the need for only **4 adjustments per year**.

After performing the analysis presented for the CPC, the following parameter values were obtained.

Table 7.1: CPC parameters used for analysis

Acceptance half-angle	15
x	4.7
l	3.86
h	9.08
A_R/A_s	18.6
E_d	0.05
CR	3.86
h/l	2.35
A_{ref}/A_{aper}	4.81
$\langle n \rangle_i$	0.9
$\langle n \rangle_{min}$	0.74
$\langle n \rangle_o$	5.86

This means that for a CPC of 15 ° of acceptance angle, its concentration ratio is **3.86** and the average number of reflections is **0.9**. It will require a total of **4.81 m**^{2} of reflector area for each m^2 of collector aperture, and its height will be **2.35** times its aperture width. Thus, for a CPC trough **1.5 m wide** and **12 m long** with an aperture area of **18.2 m**^{2}, **88 m**^{2} of reflector area will be needed and the trough will be **3.6 m high**.

From the preceding example, the reasons for truncating a CPC become obvious. Several cases will be studied in which the truncated height of the CPC will be 75%, 50% and 25% of the original height and the same analysis will be made. For the purposes of this work, the CPC will be truncated to 50%.

Table 7.2: Truncation effects on CPC parameters

$\bar{h}/h$	**25%**		**50%**		**75%**	
$\bar{x}$	2.45		3.32		4.06	
$\bar{l}$	2.83		3.48		3.78	
$\bar{h}$	2.33		4.49		6.78	
$\bar{A}_R/A_s$	5.05		9.42		14	
$\bar{E}_d$	0.1		0.07		0.06	
CR	2.83		3.48		3.78	
$\bar{h}/\bar{l}$	0.83		1.29		1.79	
$\bar{A}_{ref}/A_{aper}$	1.79		2.71		3.7	
$< n >_i$	0.51		0.69		0.81	
$< n >_{min}$	0.65		0.71		0.74	
$< n >_o$	1.99		3.15		4.42	
aperture area	18.288	m^2	18.288	m^2	18.288	m^2
reflector area	32.66	m^2	49.55	m^2	67.73	m^2
aperture width	1.524	m	1.524	m	1.524	m
height	1.26	m	1.97	m	2.73	m
length	12	m	12	m	12	m

As can be observed, even though the concentration ratio is somewhat lower, truncation of a CPC reduces reflector area and the average number of reflections significantly. This results in lower material costs and higher optical efficiency, as it depends on the average number of reflections. Truncation analyses for other acceptance half-angles were also carried out and graphed.

Table 7.3: Truncation analysis for different acceptance half-angles

	fraction of height	CR	Height/Aperture	Reflector/Aperture	$\langle n \rangle_i$
$\theta_{1/2} = 5\,^\circ$	5	1	0	0	0
$\bar{h}/h$	0.25	8.49	2.16	4.45	0.94
$\bar{h}/h$	0.495	10.39	3.4	6.9	1.12
$\bar{h}/h$	0.75	11.25	4.75	9.61	1.23
$\bar{h}/h$	1	11.47	6.21	12.53	1.31
$\theta_{1/2} = 10\,^\circ$	10	1	0	0	0
$\bar{h}/h$	0.25	4.21	1.17	2.48	0.66
$\bar{h}/h$	0.495	5.19	1.83	3.78	0.84
$\bar{h}/h$	0.75	5.64	2.55	5.22	0.96
$\bar{h}/h$	1	5.76	3.33	6.77	1.04
$\theta_{1/2} = 12\,^\circ$	12	1	0	0	0
$\bar{h}/h$	0.25	3.51	1	2.14	0.59
$\bar{h}/h$	0.495	4.33	1.56	3.25	0.77
$\bar{h}/h$	0.75	4.71	2.18	4.47	0.89
$\bar{h}/h$	1	4.81	2.84	5.8	0.98
$\theta_{1/2} = 15\,^\circ$	15	1	0	0	0
$\bar{h}/h$	0.25	2.83	0.83	1.79	0.51
$\bar{h}/h$	0.495	3.48	1.29	2.71	0.69
$\bar{h}/h$	0.75	3.78	1.8	3.72	0.81
$\bar{h}/h$	1	3.86	2.35	4.81	0.9
$\theta_{1/2} = 25\,^\circ$	25	1	0	0	0
$\bar{h}/h$	0.25	1.79	0.52	1.13	0.34
$\bar{h}/h$	0.495	2.14	0.83	1.77	0.51
$\bar{h}/h$	0.75	2.32	1.16	2.42	0.64
$\bar{h}/h$	1	2.37	1.53	3.14	0.73
$\theta_{1/2} = 36\,^\circ$	36	1	0	0	0
$\bar{h}/h$	0.25	1.37	0.35	0.75	0.24
$\bar{h}/h$	0.495	1.56	0.59	1.24	0.39
$\bar{h}/h$	0.75	1.67	0.83	1.72	0.51
$\bar{h}/h$	1	1.7	1.09	2.24	0.61

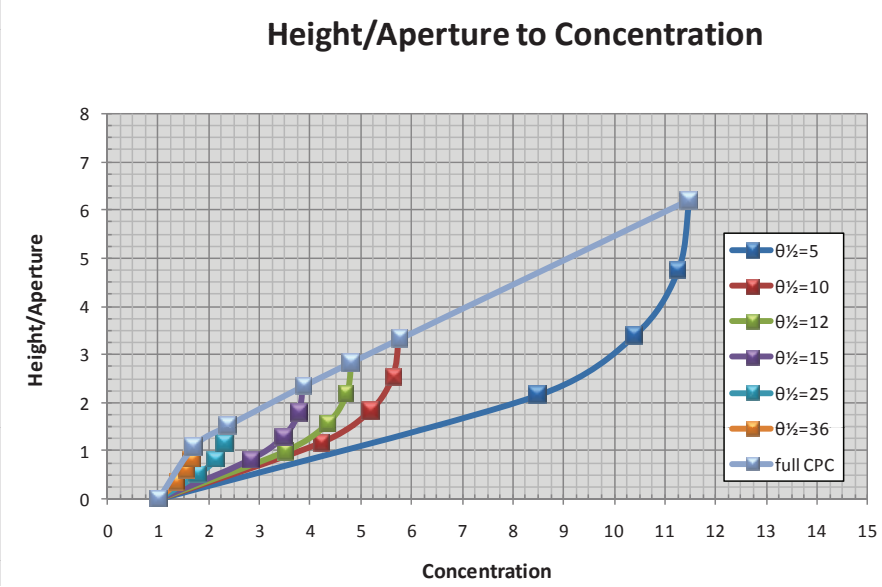

Figure 7.1: Height/aperture parameter vs. concentration for several acceptance half-angles

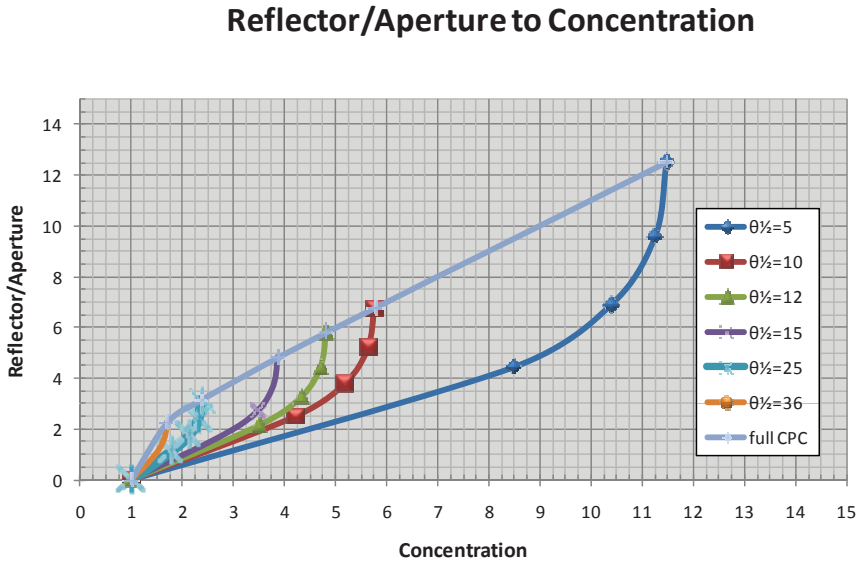

Figure 7.2: Reflector/aperture parameter vs. concentration for several acceptance half-angles

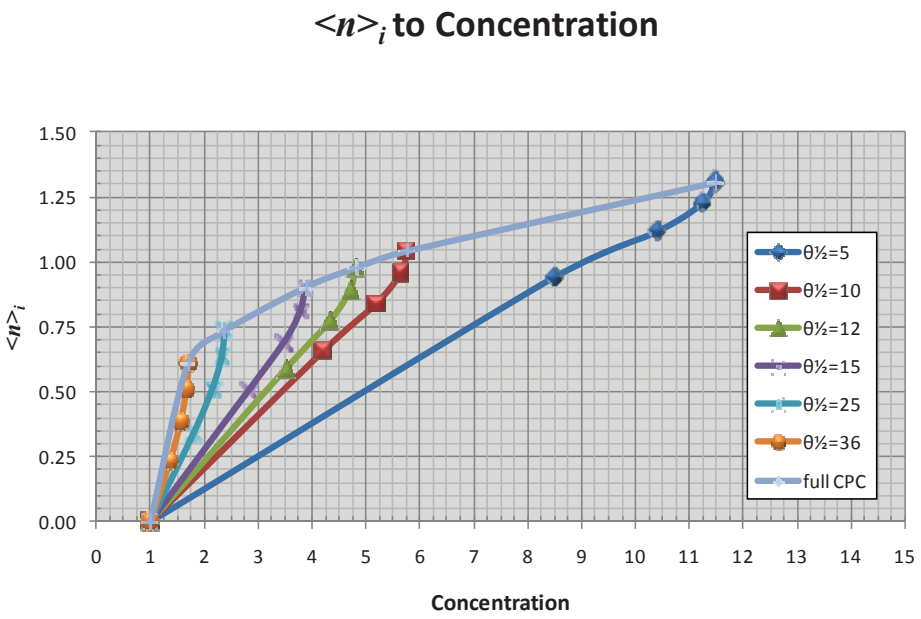

Figure 7.3: Average number of reflections vs. concentration for several acceptance half-angles

7.2 Solar Data and Radiation Absorbed by a CPC

The STPP would be erected in Juana Díaz. This location was selected due to its higher insolation and lower precipitation levels. Even though Cabo Rojo resulted with the highest insolation levels in all of Puerto Rico, it was not considered for the analysis due to the fact that the data were monthly averages. Hourly data for Cabo Rojo was not readily available. Using the data for Juana Díaz, presented in Table 7.4, and assuming typical reflectance and absorptance values (Table 7.5), the slope of the CPC needs to be determined for optimizing the energy collected through the solar window, taking into consideration that the control function, F, can provide information if any substantial beam radiation will in fact be intercepted by the CPC. The analysis resulted in **4 slope angles** each providing a **100% of the solar window availability**. These were: **-8,**

10, 25 and **44**. They are depicted in Figure 7.4.

Table 7.4: Solar data for Juana Díaz

Month\Hour	9	10	11	12	1	2	3	4
January	305.56	489.73	582.43	682.96	739.94	688.57	586.42	404.12
February	353.55	504.01	672.13	770.77	823.81	733.42	643.02	466.36
March	403.66	563.22	714.94	845.91	909.47	845.48	688.42	491.86
April	434.55	575.86	681.37	771.51	833.9	749.3	618.41	456.09
May	460.84	585.01	706.34	788.5	856.77	795.74	669.45	482.4
June	449.28	580.34	650.03	546.56	805.7	757.44	643.48	486.26
July	429.6	565.57	633.6	650.58	796.33	780.34	642.18	448.78
August	387.95	523.98	602.37	654.93	716.02	702.82	560.77	394.16
September	450.23	590.24	741.08	837.57	811.95	740.1	528.99	324.36
October	423.27	552.34	691.35	747.53	778.86	643.65	454.67	287.45
November	392.64	550.82	658.33	728.25	720.15	625.5	479.37	312.74
December	303.25	469.25	550.82	608.97	612.48	575.68	491.09	341.28

Table 7.5: Optical parameters for a CPC

Latitude	18
$\theta_{1/2}$	15
truncation %	50
CR	3.48
$< n >_i$	0.69
ρ	0.89
α	0.94

With these angles, the CPC is provided with a 100% of the solar window availability : a) **-8** from **May through August**; b) **10** for **March, April and September**; c) **24** for **March, September and October**, and d) **44** from **November through February**.

As an example, other slope angles were studied and the results are shown in Figure 7.5. This emphasizes the importance of determining the appropriate slope angles for enhancing the performance of a CPC.

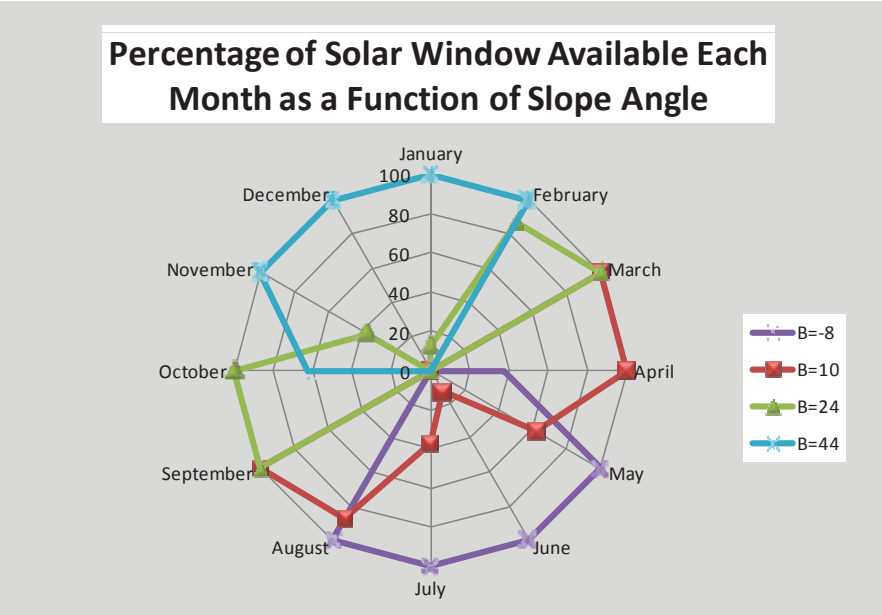

Figure 7.4: Optimized percentage of monthly solar window availability as a function of slope angle

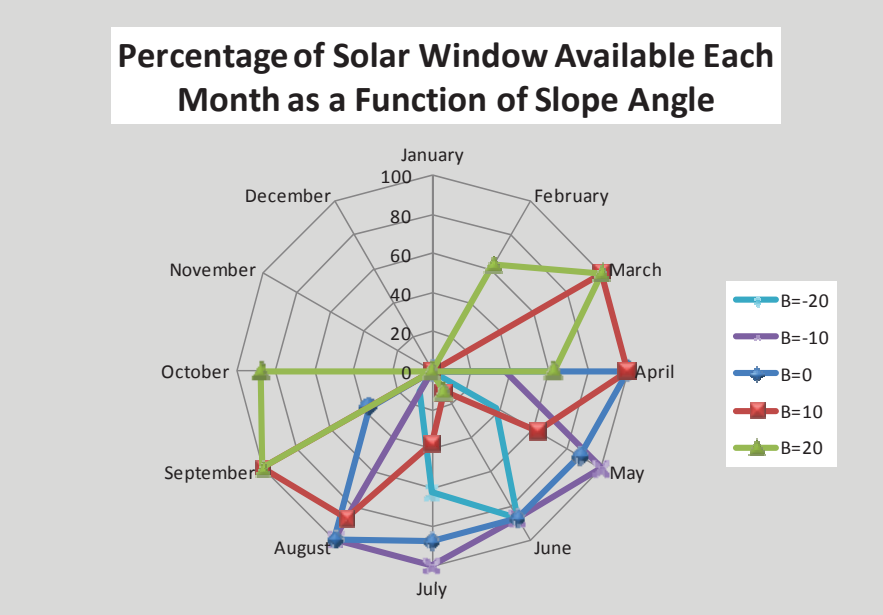

Figure 7.5: Non optimized percentage of monthly solar window availability as a function of slope angle

7.3 Thermal Analysis of a CPC with an Evacuated Receiver

The values presented in Table 7.6 were used for the thermal analysis. These were either calculated or obtained from literature.

The loss coefficient was calculated to be: **6.95 W/m^2** °C. Further analysis provided the data shown in Table 7.7 for an array of CPC collectors arranged in series.

As can be seen in Table 7.7, an array of **80 CPCs in series** provides an outlet fluid temperature of around: 450 °C. The value of **1200 W/m^2** was selected as an average value for radiation absorbed by a CPC. The heat transfer fluid inlet temperature, 140 °C, was fixed due to the fact that solar salt freezes at temperatures below 120 °C. An auxiliary heating system must be considered to avoid the HTF to freeze in the solar collector field if there are considerable solar transients during the day, or at night.

Table 7.6: Thermal analysis parameters

Values used in Thermal Analysis		
Receiver inner diameter	0.115	m
Receiver outer diameter	0.125	m
Thickness of receiver	0.005	m
Operating temperature	350	°C
Emittance of receiver	0.31	
Emittance of collector	0.88	
Thermal conductivity glass	1.4	
Glass cover outer diameter	0.148	m
Glass thickness	4	mm
Glass cover inner diameter	0.14	m
Length	1	m
Wind speed	3	m/s
Sky temperature	2	°C
Air temperature	10	°C
Conductivity of steel	16	W/m °C
Collector width	1.524	m
Collector length	12	m
Required Power Output	30	MW
Turbine Operating Temp	420	°C
Turbine Operating Pressure	10000	kPa
Turbine mass flow	41.5	kg/s
Condenser Temperature	106	°C
S lower	600	W/m^2
Fluid temp entering absorber	140	°C
Mass flow per collector	2	kg/s
Specific Heat (water)	4.18	kJ/kg °C
Specific Heat (salt)	1.56	kJ/kg °C
heat transfer coefficient	6605	W/m^2 °C

Table 7.7: Analysis of the number of collectors needed in series

Collector	$T_{fluid_{in}}$ (°C)	Useful gain (W)	ΔT (°C)	$T_{fluid_{out}}$ (°C)	T_{drop}	$T_{avg_{receiver}}$ (°C)
Q1	140	17613.9	5.65	145.6	1.78	144.6
Q2	145.6	17430	5.59	151.2	1.76	150.2
Q3	151.2	17248	5.53	156.8	1.75	155.7
Q4	156.8	17067.8	5.47	162.2	1.73	161.2
Q5	162.2	16889.6	5.41	167.6	1.71	166.6
Q6	167.6	16713.2	5.36	173	1.69	172
Q7	173	16538.7	5.3	178.3	1.67	177.3
Q8	178.3	16366	5.25	183.5	1.66	182.6
Q9	183.5	16195.1	5.19	188.7	1.64	187.8
Q10	188.7	16025.9	5.14	193.9	1.62	192.9
Q11	193.9	15858.6	5.08	199	1.61	198
Q12	199	15693	5.03	204	1.59	203.1
Q13	204	15529.1	4.98	209	1.57	208
Q14	209	15366.9	4.93	213.9	1.56	213
Q15	213.9	15206.5	4.87	218.8	1.54	217.9
Q16	218.8	15047.7	4.82	223.6	1.52	222.7
Q17	223.6	14890.5	4.77	228.4	1.51	227.5
Q18	228.4	14735	4.72	233.1	1.49	232.2
Q19	233.1	14581.1	4.67	237.8	1.48	236.9
Q20	237.8	14428.9	4.62	242.4	1.46	241.5
Q21	242.4	14278.2	4.58	247	1.45	246.1
Q22	247	14129.1	4.53	251.5	1.43	250.7
Q23	251.5	13981.5	4.48	256	1.42	255.1
Q24	256	13835.5	4.43	260.4	1.4	259.6
Q25	260.4	13691	4.39	264.8	1.39	264
Q26	264.8	13548.1	4.34	269.1	1.37	268.3
Q27	269.1	13406.6	4.3	273.4	1.36	272.6
Q28	273.4	13266.6	4.25	277.7	1.34	276.9
Q29	277.7	13128	4.21	281.9	1.33	281.1
Q30	281.9	12990.9	4.16	286.1	1.32	285.3

Continued on next page ...

Collector	$T_{fluid_{in}}$ (°C)	Useful gain (W)	ΔT (°C)	$T_{fluid_{out}}$ (°C)	T_{drop}	$T_{avg_{receiver}}$ (°C)
Q31	286.1	12855.3	4.12	290.2	1.3	289.4
Q32	290.2	12721	4.08	294.2	1.29	293.5
Q33	294.2	12588.2	4.03	298.3	1.27	297.5
Q34	298.3	12456.7	3.99	302.3	1.26	301.5
Q35	302.3	12326.7	3.95	306.2	1.25	305.5
Q36	306.2	12197.9	3.91	310.1	1.23	309.4
Q37	310.1	12070.5	3.87	314	1.22	313.3
Q38	314	11944.5	3.83	317.8	1.21	317.1
Q39	317.8	11819.8	3.79	321.6	1.2	320.9
Q40	321.6	11696.3	3.75	325.4	1.18	324.7
Q41	325.4	11574.2	3.71	329.1	1.17	328.4
Q42	329.1	11453.3	3.67	332.8	1.16	332.1
Q43	332.8	11333.7	3.63	336.4	1.15	335.7
Q44	336.4	11215.4	3.59	340	1.14	339.3
Q45	340	11098.2	3.56	343.5	1.12	342.9
Q46	343.5	10982.3	3.52	347.1	1.11	346.4
Q47	347.1	10867.6	3.48	350.5	1.1	349.9
Q48	350.5	10754.2	3.45	354	1.09	353.4
Q49	354	10641.8	3.41	357.4	1.08	356.8
Q50	357.4	10530.7	3.38	360.8	1.07	360.2
Q51	360.8	10420.7	3.34	364.1	1.06	363.5
Q52	364.1	10311.9	3.31	367.4	1.04	366.8
Q53	367.4	10204.2	3.27	370.7	1.03	370.1
Q54	370.7	10097.7	3.24	373.9	1.02	373.3
Q55	373.9	9992.2	3.2	377.1	1.01	376.5
Q56	377.1	9887.9	3.17	380.3	1	379.7
Q57	380.3	9784.6	3.14	383.4	0.99	382.9
Q58	383.4	9682.4	3.1	386.5	0.98	386
Q59	386.5	9581.3	3.07	389.6	0.97	389
Q60	389.6	9481.3	3.04	392.6	0.96	392.1

Continued on next page ...

Collector	$T_{fluid_{in}}$ (°C)	Useful gain (W)	ΔT (°C)	$T_{fluid_{out}}$ (°C)	T_{drop}	$T_{avg_{receiver}}$ (°C)
Q61	392.6	9382.3	3.01	395.7	0.95	395.1
Q62	395.7	9284.3	2.98	398.6	0.94	398.1
Q63	398.6	9187.3	2.94	401.6	0.93	401
Q64	401.6	9091.4	2.91	404.5	0.92	404
Q65	404.5	8996.4	2.88	407.4	0.91	406.8
Q66	407.4	8902.5	2.85	410.2	0.9	409.7
Q67	410.2	8809.5	2.82	413	0.89	412.5
Q68	413	8717.5	2.79	415.8	0.88	415.3
Q69	415.8	8626.5	2.76	418.6	0.87	418.1
Q70	418.6	8536.4	2.74	421.3	0.86	420.8
Q71	421.3	8447.3	2.71	424	0.86	423.6
Q72	424	8359	2.68	426.7	0.85	426.2
Q73	426.7	8271.8	2.65	429.4	0.84	428.9
Q74	429.4	8185.4	2.62	432	0.83	431.5
Q75	432	8099.9	2.6	434.6	0.82	434.1
Q76	434.6	8015.3	2.57	437.2	0.81	436.7
Q77	437.2	7931.6	2.54	439.7	0.8	439.2
Q78	439.7	7848.8	2.52	442.2	0.79	441.8
Q79	442.2	7766.8	2.49	444.7	0.79	444.3
Q80	444.7	7685.7	2.46	447.2	0.78	446.7

7.4 Power Block Analysis

The power block analysis was carried out on a simple Rankine cycle. Typical power plants use reheat or recirculation in the cycle for improving system efficiency. Literature suggests that it is the plant designers' job to evaluate the system and then specify design parameters for the power plant components to be manufactured [37]. Due to this fact, the following parameters were selected for the power block analysis:

Table 7.8: Power block parameters used for the analysis

Power Block Data		
Turbine inlet temp	420	°C
Turbine inlet pressure	10000	kPa
Condenser drop pressure	125	kPa
Mass flow rate	41.5	kg/s

7.5 Solar Array

After having completed the Optical, Thermal and Power Block analysis, the solar array would consist of 80 series collectors (**1.52 m wide, 12 m long with a height of 1.97 m and a reflector area of 49.6 m^2**) and 150 parallel rows to account for the HTF mass flow needed to produce the necessary steam mass flow at the design temperature. An **300 kg/s** mass flow was chosen for the HTF although, it can be adjusted for controlling the HTF outlet temperature to the power block segment, thus maintaining the steam's temperature to the turbine inlet.

With this information, an approximate array and land area can be calculated.

Table 7.9: Collector array and land area calculations

	Area Calculations	
aperture area	219456	m^2
reflector area	594643	m^2
reflector land area	55.86	acres
Total land area	139.64	acres

The total land area is usually three times that of the reflector land area. This is due to the fact that space is needed for access roads, to avoid shadowing effects, to allow for tracking movements, and to provide maintenance to the collector field. A total land area of **2.5 times** the reflector land area was used in the analysis, since no tracking system is used.

7.6 Heat Transfer Coefficient and the Loss Coefficient's Variation with Temperature

Even though the procedure for calculating the fluid's heat transfer coefficient was discussed, the analysis was conducted using the manufacturer's data provided. Tables 7.10 and 7.11 summarize the Solar Salt's composition and its fluid properties, respectively.

An analysis was performed to determine the loss coefficient variation with temperature. The data used in the analysis was presented in Table 7.6. Figure 7.6 represents the loss coefficient variation with temperature.

Even though the loss coefficient's variation with temperature can be seen as sig-

Table 7.10: Components of Hitec Solar Salt

Component	Minimum, %	Maximum, %
$NaNO_3$	59	61
KNO_3	39	41
NaCI		0.3
Na_2SO_4		0.3
CaO		0.03
MgO		0.03
SiO_2		0.02
AI_2O_3		0.025
Fe_2O_3		0.025
Insolubles		0.06
Na_2CO_3		0.15

Table 7.11: Manufacturer's data on Hitec Solar Salt

Solid State		
Bulk Density (lb/ft^3) –(kg/m^3)	70-80	1121.3-1281.5
Melting Point (°F)– (°C)	431	221.7
Specific Heat (BTU/lb °F)–(J/kg K)	0.29	1214.2
Liquid State		
Specific Heat, average (BTU/lb °F)–(J/kg K)	0.37	1549.1
Density (lb/ft^3)–(kg/m^3)	112	1794.1
Viscosity (cp)–(kg/m s)	2.1	0.000214
Thermal Conductivity (BTU/hr ft, °F)–(W/ m K)	0.31	0.5365
Heat Transfer Coefficient (BTU/hr ft^2, F)–(W/m^2 K)	1164	6605.1

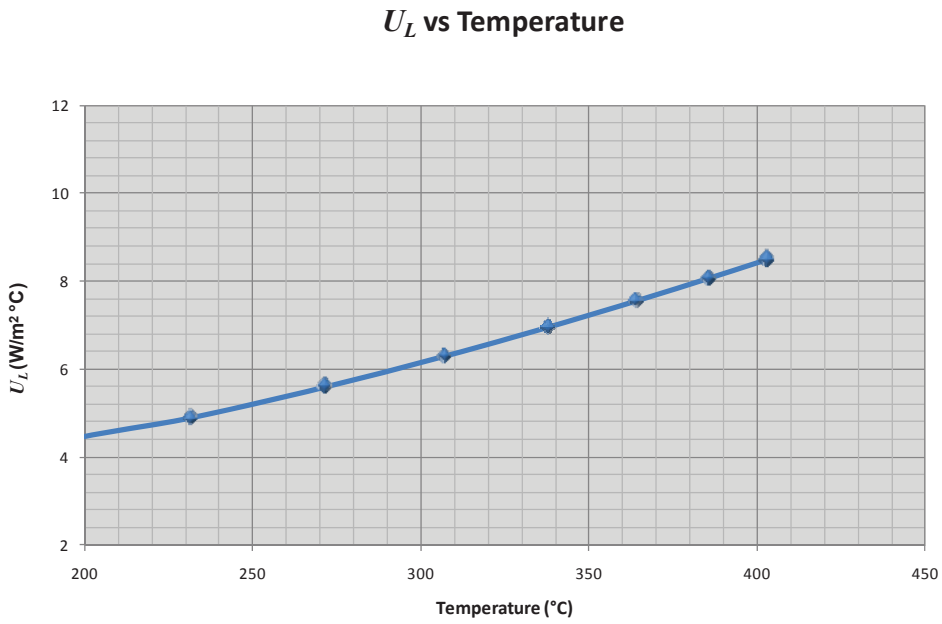

Figure 7.6: Graph representing the loss coefficient variation with temperature

nificant, studies suggest using an average loss coefficient value for an average system temperature. The loss coefficient is part of the collector's useful gain equation, recalling this equation which is presented below, the variation of the loss coefficient has very little effect on the useful gain, and hence on the exit fluid temperature.

$$Q_u = F_R A_{aper} \left[S - \frac{A_{receiver}}{A_{aper}} U_L \left(T_i - T_a \right) \right] \tag{7.1}$$

As has been calculated, the absorbed radiation, S, is a rather large number (around 700-1500 W/m^2), whereas the ratio of areas, the inverse of the concentration ratio CR, is a small fractional value. The inverse of CR times U_L and the temperature difference is still a small value compared to the absorbed radiation.

The following table summarizes the useful gain and exit fluid temperature that

resulted from accounting for the loss coefficient variation with temperature.

Table 7.12: Loss coefficient variation with temperature

Collector	T_{in} (°C)	T_{in} (K)	Loss coeff. U_L	Q_u (W)	ΔT(°C)	$T_{fluid_{out}}$ (°C)
Q0-8	140	413	3.01	149115.9	47.8	187.8
Q8-16	187.8	460.8	4.27	136207.4	43.7	231.4
Q16-24	231.4	504.4	4.9	124484.4	39.9	271.3
Q24-32	271.3	544.3	5.61	110864.9	35.5	306.9
Q32-40	306.9	579.9	6.31	96206.74	30.8	337.7
Q40-48	337.7	610.7	6.97	81380.37	26.1	363.8
Q48-56	363.8	636.8	7.56	67221.47	21.5	385.3
Q56-64	385.3	658.3	8.07	54359.24	17.4	402.8
Q64-72	402.8	675.8	8.5	43168.14	13.8	416.6
Q72-80	416.6	689.6	8.85	33771.1	10.8	427.4

Table 7.13 presents the same analysis using the U_L value calculated for the operating temperature (350 °C).

Table 7.13: Calculations without accounting for the loss coefficient variation with temperature

Collector	T_{in} (°C)	T_{in} (K)	Loss coeff. U_L	Q_u (W)	ΔT(°C)	$T_{fluid_{out}}$ (°C)
Q0-8	140	413	6.95	132370.9	42.4	182.4
Q8-16	182.4	455.4	6.95	121470.3	38.9	221.4
Q16-24	221.4	494.4	6.95	111467.4	35.7	257.1
Q24-32	257.1	530.1	6.95	102288.3	32.8	289.9
Q32-40	289.9	562.9	6.95	93864.98	30.1	320
Q40-48	320	593	6.95	86135.35	27.6	347.6
Q48-56	347.6	620.6	6.95	79042.24	25.3	372.9
Q56-64	372.9	645.9	6.95	72533.23	23.2	396.1
Q64-72	396.1	669.1	6.95	66560.23	21.3	417.5
Q72-80	417.5	690.5	6.95	61079.1	19.6	437.1

As can be seen, the exit fluid temperature differs by only 9.6 °C. The use of an average value greatly simplifies the analysis since the loss coefficient calculation is found by iteration and must be calculated for each case.

7.7 Pressure Drop Calculations

Using the pressure drop calculation method described yielded the following result: A drop of **0.0007829 MPa/m**. Each collector loop was estimated to be **960 m long**, hence, the total pressure drop is: **0.7516 MPa**. This computation is only relevant for determining the power input to the system's pump or pumps.

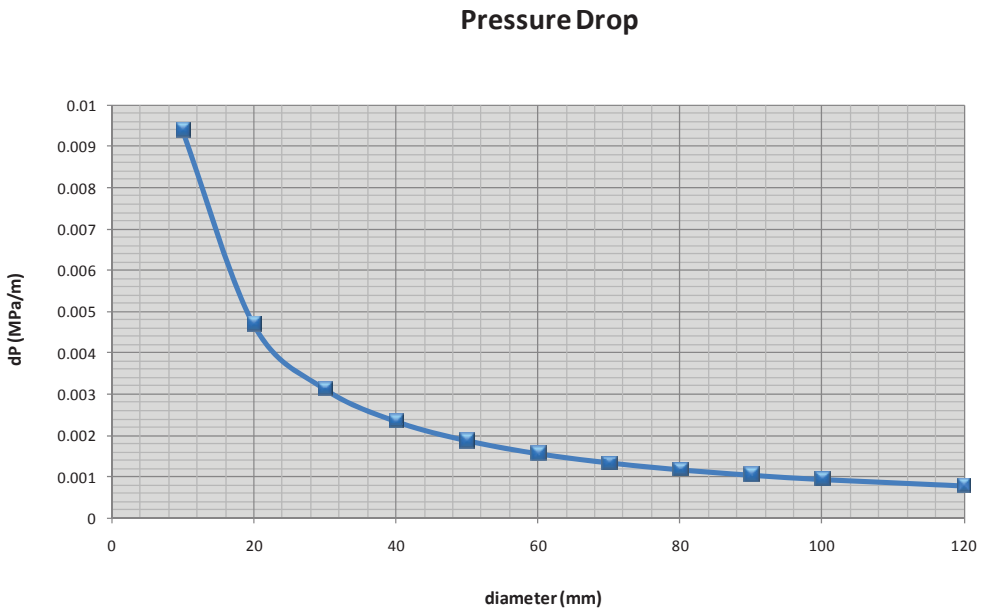

Figure 7.7: Pressure drop vs. pipe diameter

7.8 Heat Exchanger (HX) Calculations

Even though the heat exchanging process requires several stages, the analysis was conducted as though there was a single heat exchanging device. An energy balance calculation following the effectiveness-NTU method yielded the results in Table 7.15:

Table 7.14: 'Hot' and 'cold' fluid properties

Fluid and HX Properties		
Cold	water	
$\dot{m}_c$	41.5	kg/s
T_{ci}	106	°C
C_p	4,181	J/kg
Hot	salt	
$\dot{m}_h$	300	Kg/s
T_{hi}	420	°C
C_p	1,560	J/kg
UA_{HX}	505,000	W/K

Table 7.15: Energy balance results for HX analysis

Energy Balance		
$C*$	0.371	
NTU	2.911	
e	0.893	
Q_{max}	54,469,580	W
Q	48,636,087	W

7.9 Economic Analysis and the Levelized Electricity Cost

The most important aspects concerning the cost of electricity generation is to consider the structure of the investment, its financing, and its fuel costs, if any. It is necessary to be conscious of the financial strategy that will be applied, the time of construction, and investment cost, including capital repayment. These factors are kept implicitly in mind in the applicable interest rate for the lifetime of the project. The levelized electricity cost of production quantifies the unitary cost of the product (or kWh) generated during the power plant's lifetime; and allows the immediate comparison with the cost of other alternative technologies [59, 60].

The *levelized electricity cost* (LEC) considers the cost of generating electricity for a particular system by making an economic assessment of the cost of the electricity generating system including all the costs over its lifetime. A net present value calculation is performed and solved in such a way that for the value of the LEC chosen, the project's net present value becomes zero. In other words, the LEC is the minimum price at which energy must be sold for an energy project to break even [59]. It can be defined as:

$$LEC = \frac{\sum_{t=1}^{n} \frac{CI_t + O\&M_t + F_t}{(1+i)^t}}{\sum_{t=1}^{n} \frac{E_t}{(1+i)^t}} \tag{7.2}$$

where, CI_t is the capital investment expenditure, $O\&M_t$ is operation and maintenance cost, F_t is fuel cost and E_t is the electricity produced, all in the year t. i and n represent the interest rate and life of the system, respectively. Typically, LECs are calculated over 20 to 40 year lifetimes, and are given in the units of currency per kilowatt-hour.

As to have an idea of how much this type of system could cost, data from SunLab [31] was used to estimate the initial capital cost of this type of system and an estimated operation and maintenance cost. The U.S. Department of Energy (DOE) administers the Concentrating Solar Power Program through two of its national laboratories: Sandia National Laboratories and the National Renewable Energy Laboratory (NREL). To increase the efficiency of each of the laboratories, the DOE combined the concentrating solar power departments of each into a single business unit called SunLab.

Even though the proposed system is not exactly the same as the ones described in these studies, these numbers represent the most accurate data available in term of component costs. The data in Table 7.16 was used in the analysis. The electricity that the system can produce will be estimated by means of a simulation model that is presented in the next chapter.

Table 7.16: SunLab cost data used in the analysis

Costs	Base-line	SunLab		
Project:	SEGS VI	Near Term	Mid Term	Mid Term
In Service	1989	2004	2007	2010
Support Structure ($/m^2)	67	61	57	54
Heat Collection Elements ($/m^2)	43	43	34	28
Mirrors ($/m^2)	43	43	36	28
Power Block/Balance of Plant ($/kWe)	747	581	581	525
Thermal Storage ($/kWh)	NA	27.1	12.7	11.7
Operation and maintenance ($/kWh)	0.024	0.0228	0.0171	0.0135
Miscellaneous 32% of the cost of Support Structure, Heat Collection Elements and Mirrors				
Total Plant Cost ($/kWe)	3,008	4,856	3,408	3,416

SunLab data provides costs for the year 2004, the year the study was conducted, and forecasted costs for mid-term (2007 through 2015) and long term periods (2015 through 2020). As stated, the SunLab model can provide a cost estimate that closely follows the industry expectations for research and development advances in component and subsystem improvements. This plan was designed to incorporate the use of thermal storage starting in 2004, and also the commercialization of the U.S. trough industry [31]. It is important to acknowledge that since the SEGS plants were erected in late 1980's and early 1990's, there have not been any new developments until 2004, when studies were undertaken once again. There have also been one sole supplier of collectors and HCE for the SEGS plants ever since. It is expected that since trough plant development is undertaken, new companies arise, providing competition and, consequently, a reduction in system costs.

Chapter 8

SIMULINK MODEL FOR STPP SIMULATION

After having performed the preceding analysis, a simulation model was developed so that the transient effects of solar energy could be observed throughout a whole day. Even though average radiation values are commonly used for analysis, these usually are data measured for locations which are known for having some of the best solar resources on the planet, thus the use of average values makes perfect sense. The issue arises when the location under study has decent solar resource considering average values, but it is known to lie on a tropical region where there is considerable solar radiation scattering due to atmospheric conditions such as: clouds, rain and/or dust.

The only way to study these conditions would be to make use of solar radiation measured over a shorter time span. As can be found in literature [61, 62, 63, 64, 65, 66, 67], several of the simulation studies that have been performed rely on parabolic troughs, costly software packages and on prototype system measurements usually conducted where solar radiation is the highest in the world. This model will show how system per-

formance is affected during solar transients in tropical regions, taking into account solar variability throughout the day. The system model will be built in SIMULINK® and run from the MATLAB® platform. Several parts of the system will be implemented in MATLAB® for simplicity. The model will include several modules in SIMULINK® such as: a CPC collector row, a collector useful gain calculation, power block analysis, and a plots module to observe the results.

The heat exchanger analysis and the calculations for the power block stage regarding the superheating and mixture stages of steam production will be implemented in MATLAB® and the results will be imported into the SIMULINK® model through the "from workspace" block. The calculations made for the power block where performed by X Steam for MATLAB®, by Magnus Holmgren [68].

X Steam for MATLAB® is an implementation of the IAPWS (International Association for the Properties of Water and Steam) IF97 standard formulation equations. It provides accurate thermo hydraulic data for water, steam or mixtures of the two.

The parameters used for the simulation model are presented in Table 8.1. Some of these were calculated through thermal or optical analysis. Others were selected as system parameters or taken from literature.

8.1 System Simulation Blocks

The CPC collector row is modeled as a subsystem depicted in Figure 8.1 that depends on its components' design parameters. These were discussed in Chapters 4 and 7. With this subsystem's outputs, along with the measured solar radiation and the absorber's optical parameters, namely transmittance and absorptance, the absorbed

Table 8.1: Parameters employed in the SIMULINK® system model

SIMULINK® Parameters			
Parameter	Variable Name	Value	Units
number of collectors	collectors	70	
collector length	clength	12	m
collector width	cwidth	1.524	m
receiver diameter	rec_diam	0.125	m
receiver thickness	rec_thick	0.005	m
glass cover diameter	g_diam	0.148	m
absorptance	alpha	0.94	
transmissivity	tau	0.9227	
number of internal reflections	ni	0.69	
heat transfer coefficient	hfi	6605	$W/m^2\,°C$
loss coefficient	UL	6.95	$W/m^2\,°C$
conductivity steel	ksteel	16	$W/m\,°C$
row mass flow	m_row	2	kg/s
HTF mass flow	mh	300	kg/s
steam mass flow	mc	41.5	kg/s
ambient temperature	Tair	25	C
initial HTF temperature	Tinitial	140	°C
maximum HTF temperature	Tmax	420	°C
condensate initial temperature	Tic	106	°C
HTF specific heat	Cph	1560	J/kgK
HTF density	rho_f	1794	kg/m^3
hx overall htc-area product	UA	505000	W/K

radiation for the CPC can be obtained (Figure 8.2).

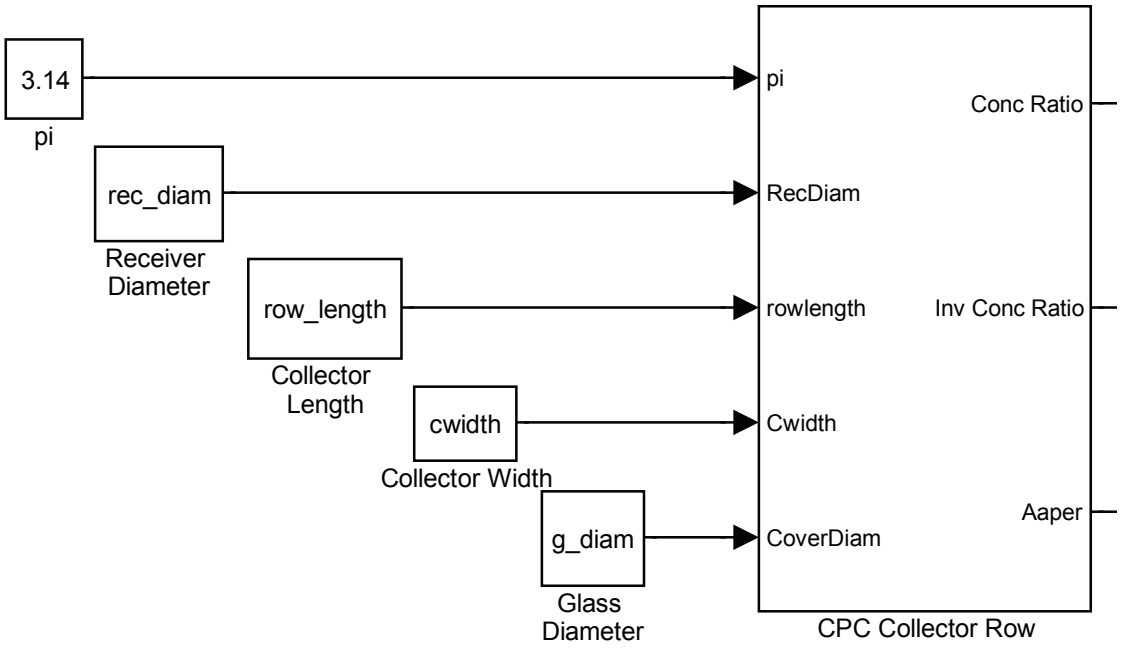

Figure 8.1: CPC Collector Row subsystem

This absorbed radiation is in turn, fed into the CPC Useful Gain subsystem (Figure 8.3) to perform the CPC's energy balance which outputs the HTF temperature leaving the collector field.

The subsystems that model the power block analysis are presented in Figure 8.4.

8.2 Simulation Model Validation

Model validation is possibly the most important step in model building and simulation. It can demonstrate that the results obtained from simulation are accurate enough to be considered acceptable. Taking this into account, the model constructed for the STPP simulation described was modified to a certain degree to try and simulate the

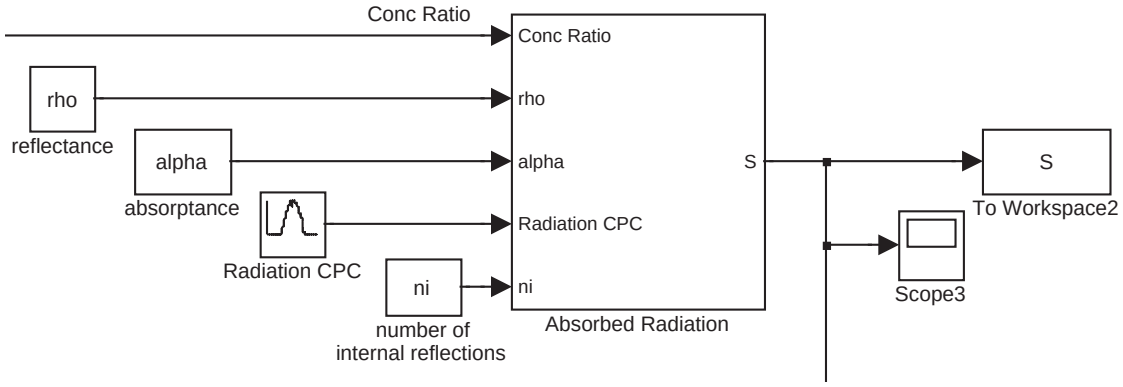

Figure 8.2: Absorbed Radiation subsystem

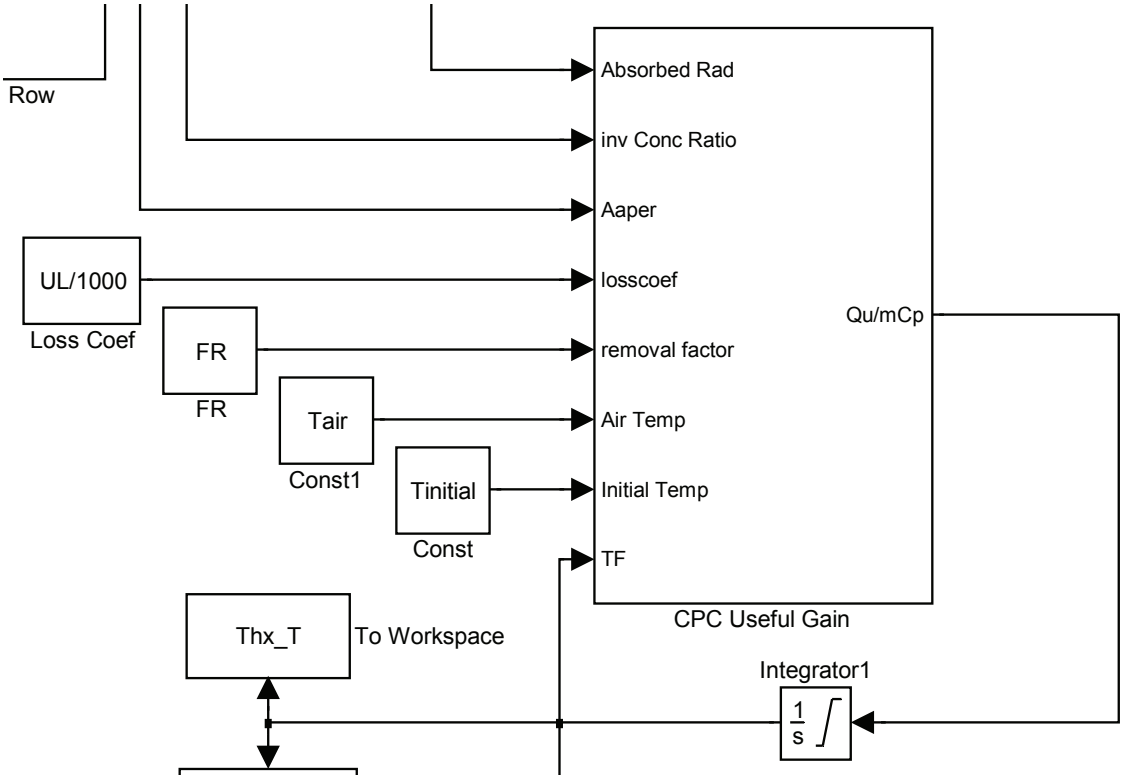

Figure 8.3: CPC Useful Gain subsystem

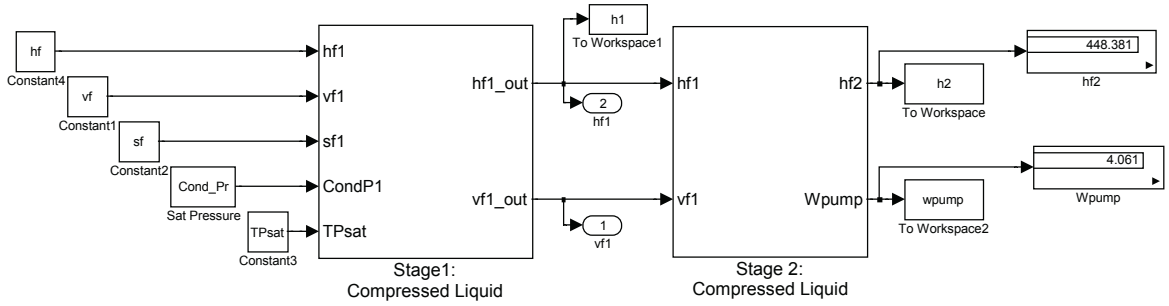

(a) Power block stages 1 and 2

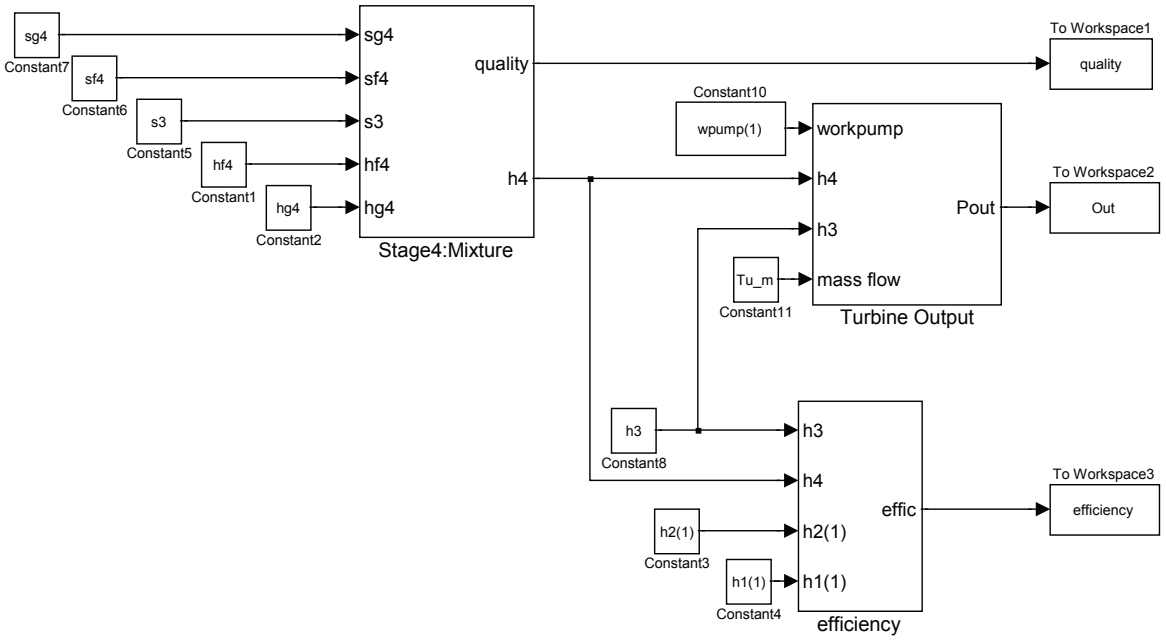

(b) Power block stage 4

Figure 8.4: Power Block subsystems

operation of a SEGS plant, in particular, the SEGS VI.

Solar radiation and measured plant data were taken from [67, 69]. This work provides data for 5 days in 1998 and 4 days in 2005 for the purpose of model validation, as for determining the cause of the plant's performance reduction over the 7 year period. A sunny (June 20, 1998) and a cloudy day (April 27, 2005) were selected from these days for the purpose of model validation. The model parameters where described previously. The ones mentioned below are the ones that were adjusted in accordance with the SEGS VI plant. The table below provides a brief description of the SEGS plants' operation from I to IX.

Table 8.2: SEGS Plant System Data (Data from NREL).

Plant	Location	Year	Output (MWe)	Solar Field Outlet, °C	Solar Field Area, m^2	Turbine Effic., %	Power Cycle	Ability to Dispatch
SEGS IX	Harper Lake	1991	80	390	483,960	37.6	100 bar, reheat	HTF heater
SEGS VIII	Harper Lake	1990	80	390	464,340	37.6	100 bar, reheat	HTF heater
SEGS VII	Kramer Junction	1989	30	390	194,280	37.5	100 bar, reheat	Gas boiler
SEGS VI	Kramer Junction	1989	30	390	188,000	37.5	100 bar, reheat	Gas boiler
SEGS V	Kramer Junction	1988	30	349	250,500	30.6	40 bar, steam	Gas boiler
SEGS IV	Kramer Junction	1987	30	349	230,300	30.6	40 bar, steam	Gas boiler
SEGS III	Kramer Junction	1987	30	349	230,300	30.6	40 bar, steam	Gas boiler
SEGS II	Daggett	1986	30	316	190,338	29.4	40 bar, steam	Gas boiler
SEGS I	Daggett	1985	13.8	307	82,960	31.5	40 bar, steam	3-hrs TES

The SEGS VI plant, in particular, has the following characteristics: It is a 30 MW net output, solar electric generating station (SEGS) with solar steam generation and solar superheating, operating a 100 bar (10 MPa) reheat power cycle. It is equipped with Luz LS-2 collectors and an auxiliary natural gas boiler to provide backup capabil-

ity during low and non-solar hours. Its operational dispatch consists of solar operation during sunny hours. Natural gas backup is operated to augment solar during summer peak from noon to 6 p.m. as necessary and during mid-peak hours.

It is important to acknowledge that even though both plants (the SEGS and the one modeled in this study) are STPP's, they differ in many aspects such as: type of radiation collected, type of collector, HTF, and power block elements. Since there are so many discrepancies in both systems, measured and modeled data were not meant to coincide. The study wanted to observe system performance by comparing the model results with the CPC collector to those obtained from the parabolic collector SEGS plant.

Results for a sunny day:

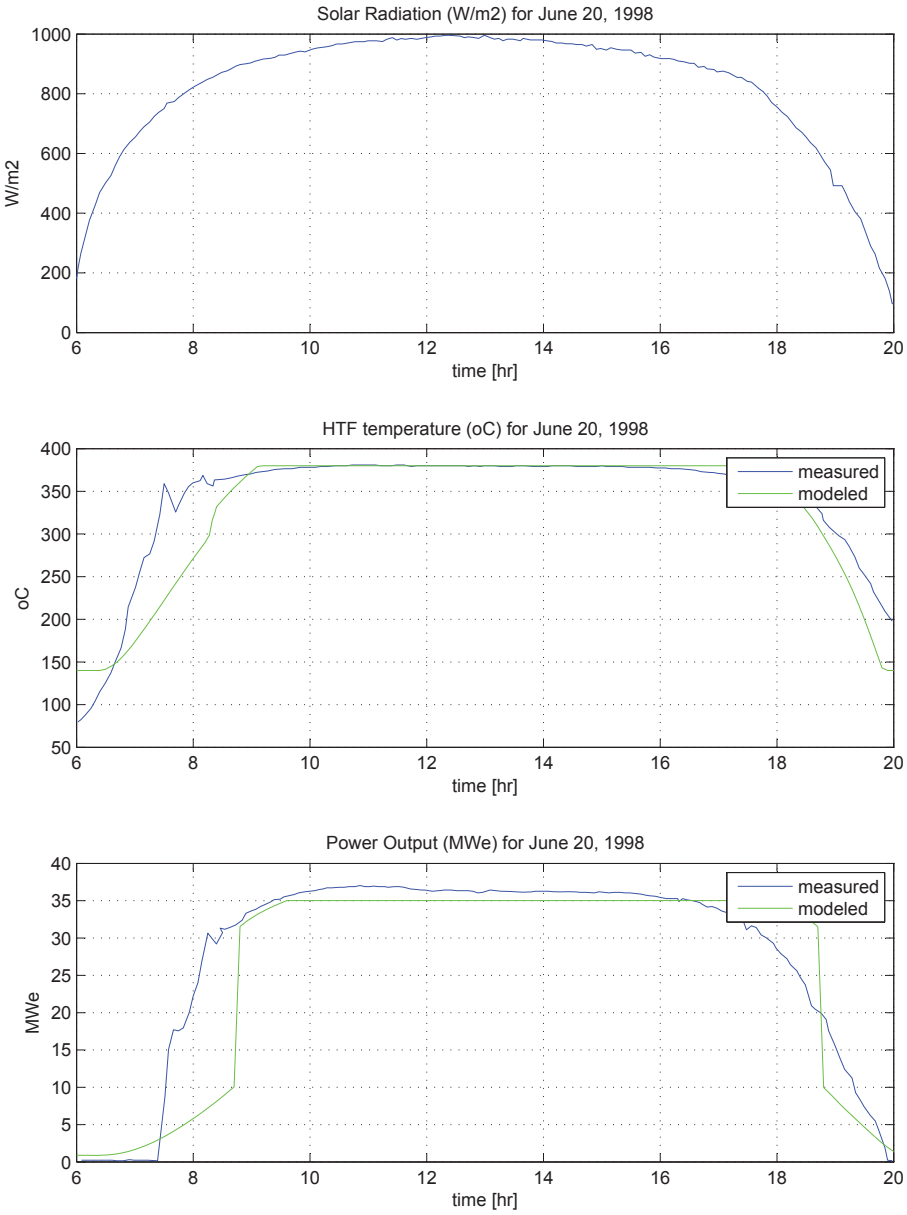

Figure 8.5: Solar Radiation, Heat Transfer Fluid Temperature and Power Output for a Sunny Day

Results for a cloudy day:

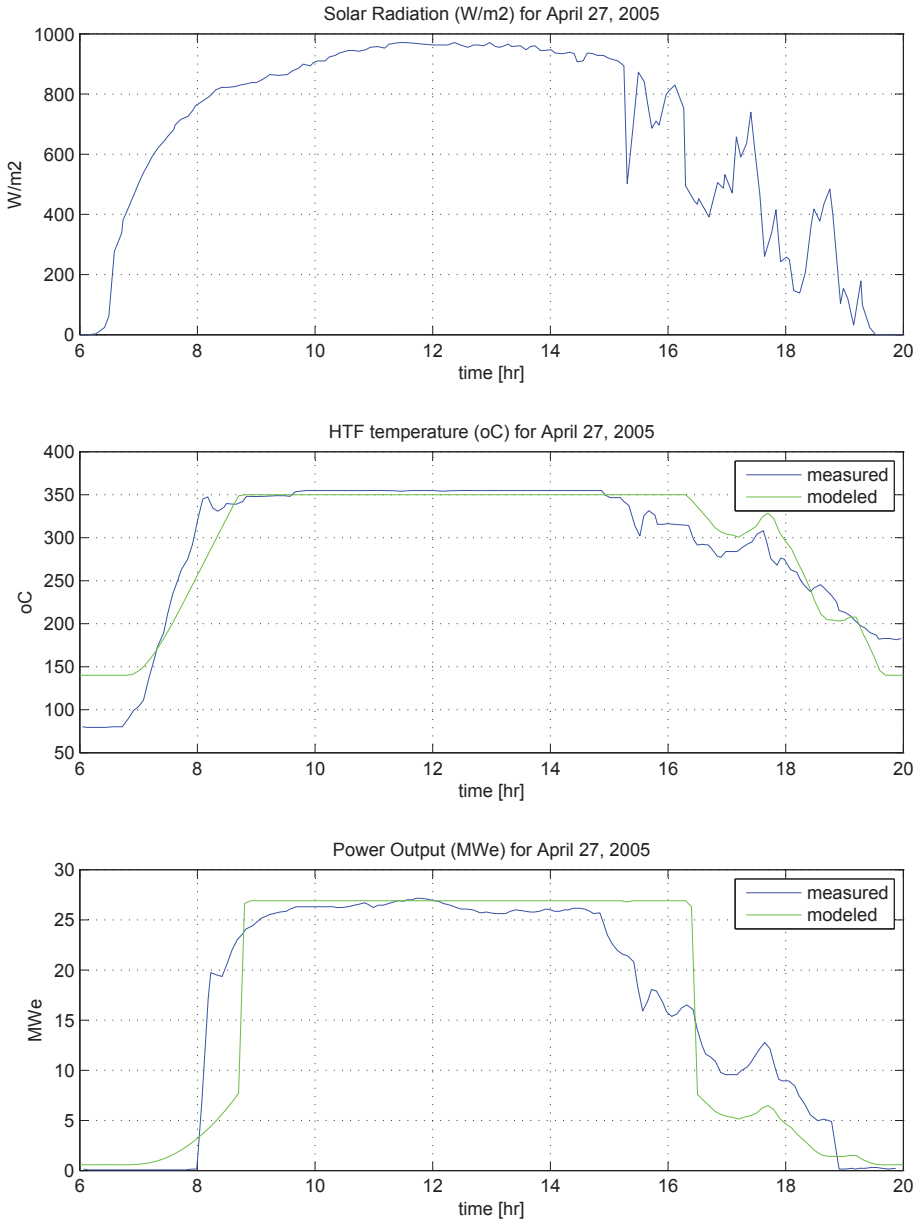

Figure 8.6: Solar Radiation, Heat Transfer Fluid Temperature and Power Output for a Cloudy Day

After running the simulations with solar data from Kramer Junction, and the data compared with the measured data from the SEGS, the results were more than satisfactory. Even though both systems differ significantly, they had a common factor: the heat collection element (HCE). As it turns out, the thermal response of the absorbing element in each collector system behaves similarly. The collector system provides its own optical and thermal properties, but it is the HCE that ultimately absorbs the solar energy, transmitting it to the HTF.

8.3 Simulation Model Limitations

8.3.1 Solar Field Model

The solar field model is efficient at attaining a reasonable steady-state, mathematical representation to an ever complex dynamic thermal system. It is meant to be used for preliminary calculations of the performance of a STPP and it in no way substitutes the use of more sophisticated modelling software (like TRNSYS). Most of the system calculations were made in Microsoft Excel and the values used in the simulation. Calculations were made regarding solar radiation utilization, system pressure drop to account for piping losses, as well as the system's loss coefficient variation with temperature, but were not included in the model. Literary review showed that these calculations can be negligible, since system components are usually designed and optimized to minimize losses [69].

Several parameters were held constant during the simulation. These were: HTF's mass flow rate, heat capacity and heat transfer coefficient; the collectors' loss coefficient (wind velocity and ambient temperature), the steam's mass flow rate, as well as the power cycle's operating and condensing pressure.

The solar field model assumes steady-state operation, therefore, it does not account for thermal capacitance. Without accounting for thermal capacitance, the model predicts somewhat hotter temperatures at the solar field outlet. This does create discrepancies at start-up, when the solar field is warming up, and at shut-down, when the field is cooling down. Thermal capacitance, namely the collectors' time constant has been studied and documented [70], the only drawback regarding this simulation is that it requires measurements from a system in operation. The time constant test is usually

performed under the ANSI / ASHRAE Standard 93. Time constant is a function of fluid temperature increase or decay, and equals the time required for equation 8.1 to change from 0 to 0.632, when heating or from 1 to 0.368, when cooling [71].

$$\frac{T_f out@t - T_f in}{T_f out\ initial - T_f in} \tag{8.1}$$

where,

$T_f out@t$ is the fluid temperature at the receiver outlet at time t , °C

$T_f in$ is the fluid temperature at the inlet to the receiver, °C

$T_f out\ initial$ is the initial fluid temperature at the receiver outlet, °C

8.3.2 Power Cycle Model

The power cycle in the SEGS VI plant is a traditional Rankine cycle. The heat transfer fluid, VP-1, is delivered to two parallel heat exchanger trains to the power cycle to generate dry steam at 371 C and 10 MPa. These are the rated power conditions for the cycle. According to [69] each train is composed of 4 heat exchangers: a reheater placed in parallel with a superheater, steam generator, and a preheater that are arranged in series.

After the superheated steam state is achieved, the steam enters a high pressure turbine, expanding and producing work. It is then reheated and directed into a second expansion phase in a low pressure turbine. Two extractions are taken from the high pressure turbine for preheating feedwater in the two mentioned feedwater heaters, whereas four steam extractions are taken from the low pressure turbine. The four steam extractions are directed to a deaerator and three additional feedwater heaters. The output from the low pressure turbine is condensed with circulating water in a

surface condenser, which in turn, is cooled using an induced draft cooling tower. The condensed steam is pumped to 1.5 MPa so it can go through the three low pressure feedwater heaters and into the deaerator. It is pumped again at the outlet of the deaerator to around 12.5 MPa and is directed to the two high pressure feedwater heaters before returning to the preheater to complete the cycle [69].

Although the power cycle modeled is also a traditional Rankine cycle, components were lumped into four main components as described before: pump, boiler, turbine and condenser. This simplification was made due to the fact that molten salt thermophysical properties or temperature-dependent correlations were not available. This is the reason why the properties pertaining to the HTF were taken as average constant values throughout the system. Due to this fact, the model's power output might be overestimated.

8.3.3 Condenser Model

In many studies encountered during literary review, the condenser system is treated apart from the power block. This is done because it requires careful analysis since the majority of these STPP are located in desert areas where there is no water readily available. Hopefully, this will not be the case in Puerto Rico.

8.4 Simulation Results

Solar data for an entire year was fed to the model. The model predicted a power output of around 54,232 MWh for 2003. Although an entire year was modeled, only several days were considered for studying system performance throughout the year. These were chosen based on atmospheric conditions: a sunny day, a partly cloudy day,

a mostly cloudy day and a rainy day. These where: March 20 and October 24, 2002; and January 28, June 26 and July 1, 2003. In the following figures, atmospheric conditions regarding temperature, wind velocity and precipitation were plotted, as well as the solar radiation for each particular day. Using this data, system performance could be observed by evaluating the results obtained from the simulation model constructed. The model is capable of plotting: Solar radiation, HTF temperature exiting the collector field, the steam temperature leaving the HX and the respective power output of the system. It is important to acknowledge that several system parameters were considered constant, such as: the HTF and steam's mass flows, number of collectors per row, mass flow of HTF per row, HTF inlet temperature, condensate water temperature and pressure, and the turbine's operating pressure. These parameters are carefully monitored in STPP such as: the SEGS. They provide a means of system control.

If the system is experiencing a clear day, radiation could be high enough as to damage system components, e.g., receivers, if the HTF temperature is higher than the system components' thermal limits. A means of control can be implemented by bypassing the HTF flow through the collector row by defocusing several collectors in a row to avoid the HTF temperature to continue rising or by increasing the HTF's mass flow through the collector row.

8.4.1 Simulation results for March 20, 2002

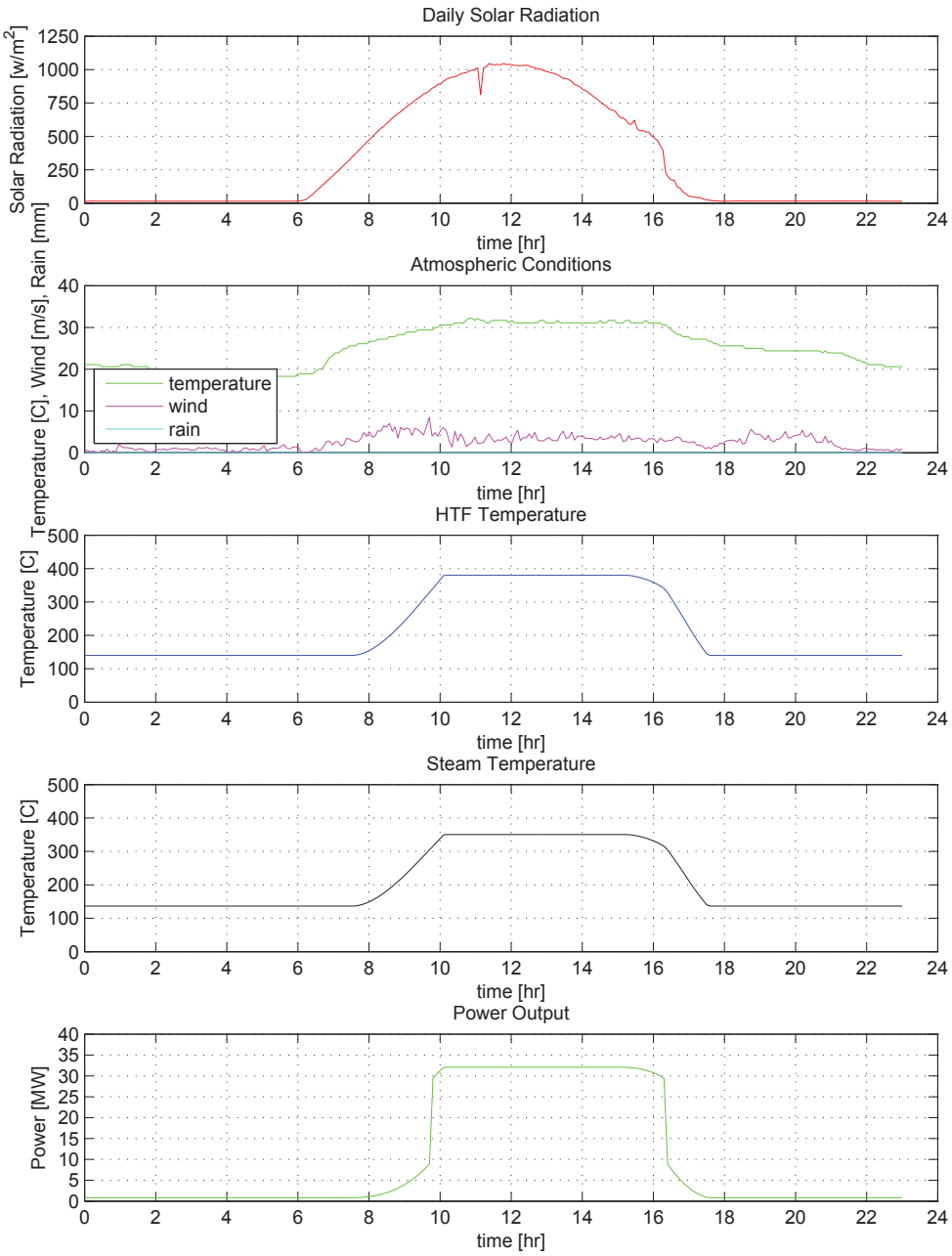

Figure 8.7: Measured Solar Radiation, Ambient Temperature, Wind Velocity, Precipitation, HTF Temperature, Steam Temperature and Power Output for March 20, 2002

8.4.2 Simulation results for October 24, 2002

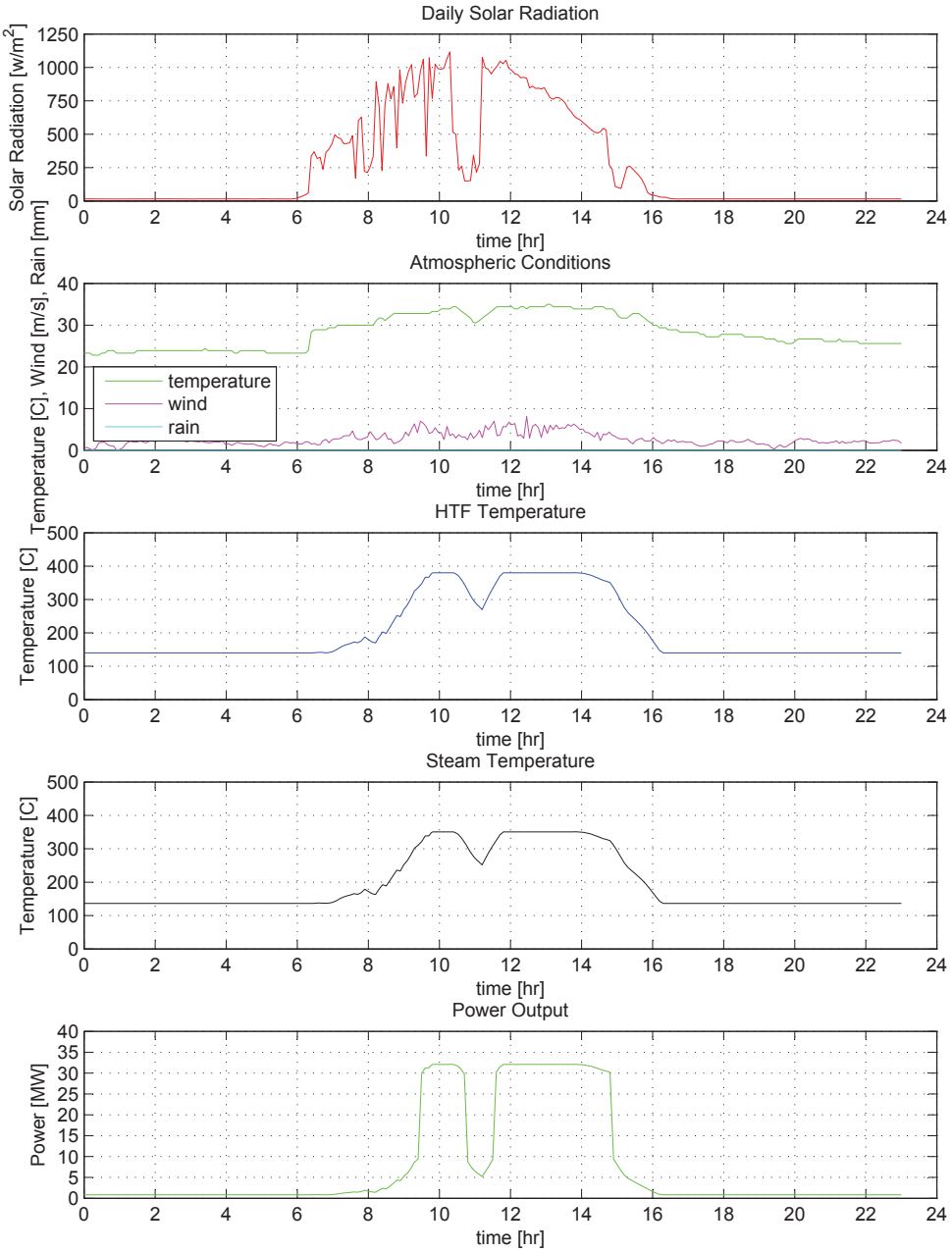

Figure 8.8: Measured Solar Radiation, Ambient Temperature, Wind Velocity, Precipitation, HTF Temperature, Steam Temperature and Power Output for October 24, 2002

8.4.3 Simulation results for January 28, 2003

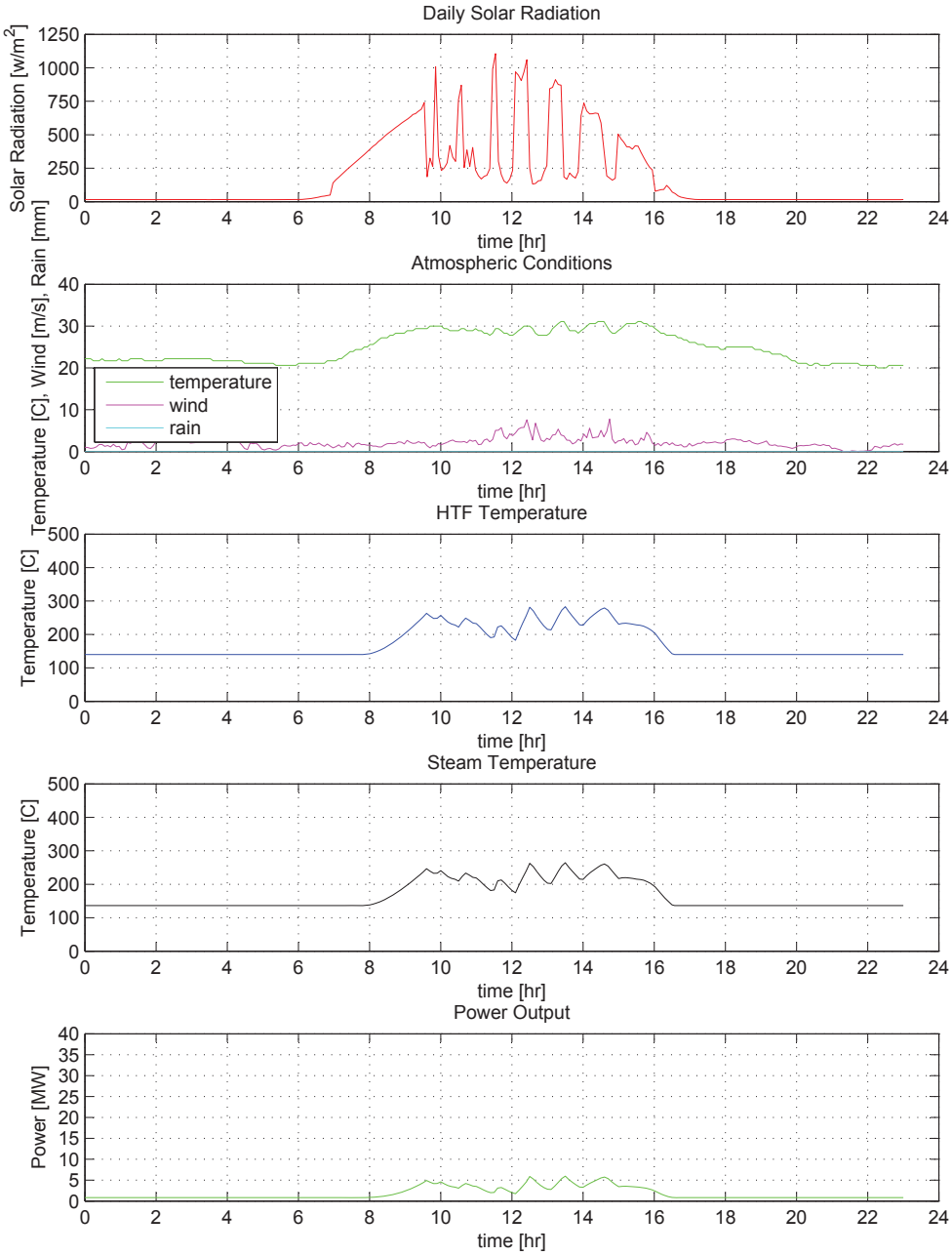

Figure 8.9: Measured Solar Radiation, Ambient Temperature, Wind Velocity, Precipitation, HTF Temperature, Steam Temperature and Power Output for January 28, 2003

8.4.4 Simulation results for June 26, 2003

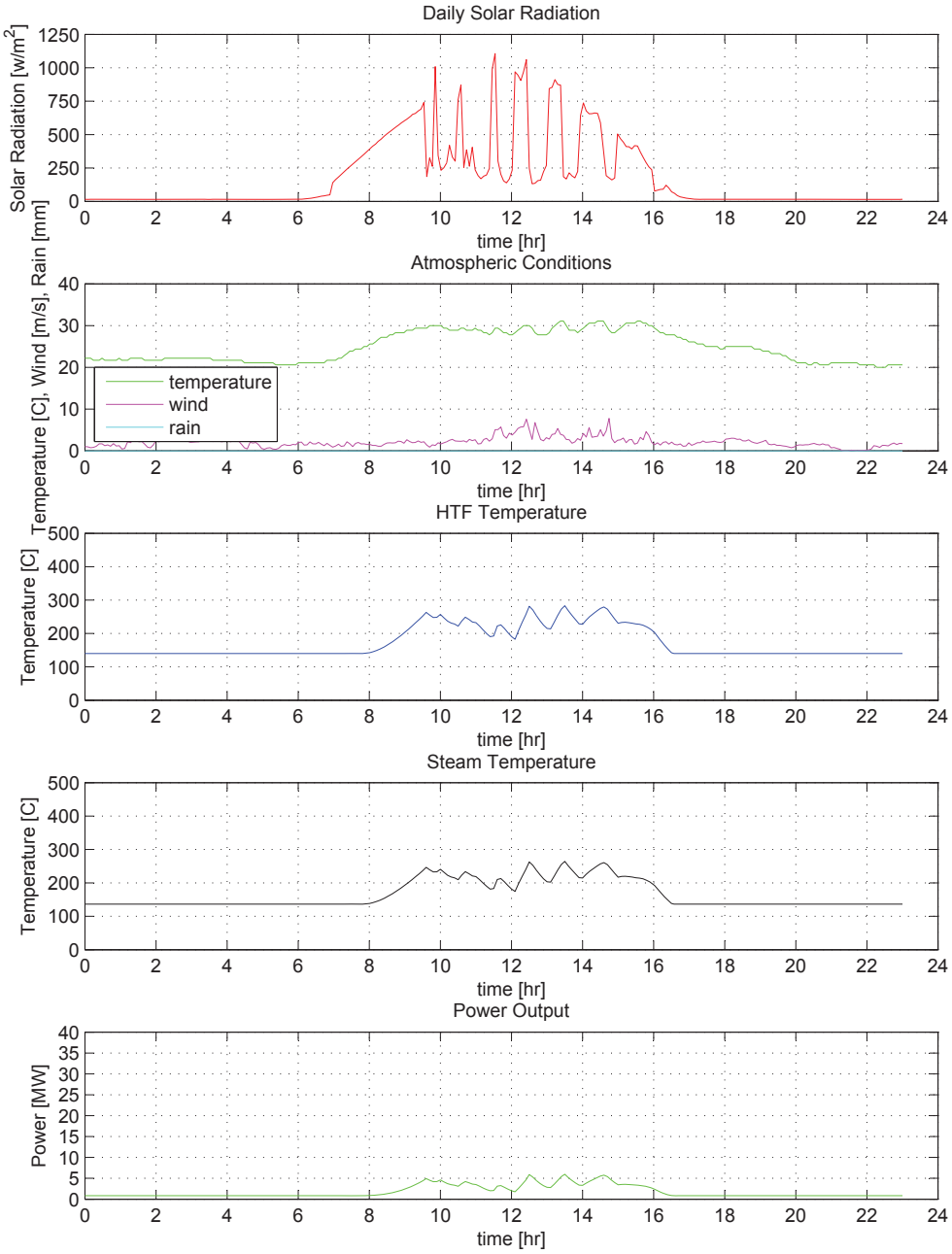

Figure 8.10: Measured Solar Radiation, Ambient Temperature, Wind Velocity, Precipitation, HTF Temperature, Steam Temperature and Power Output for June 26, 2003

8.4.5 Simulation results for July 1, 2003

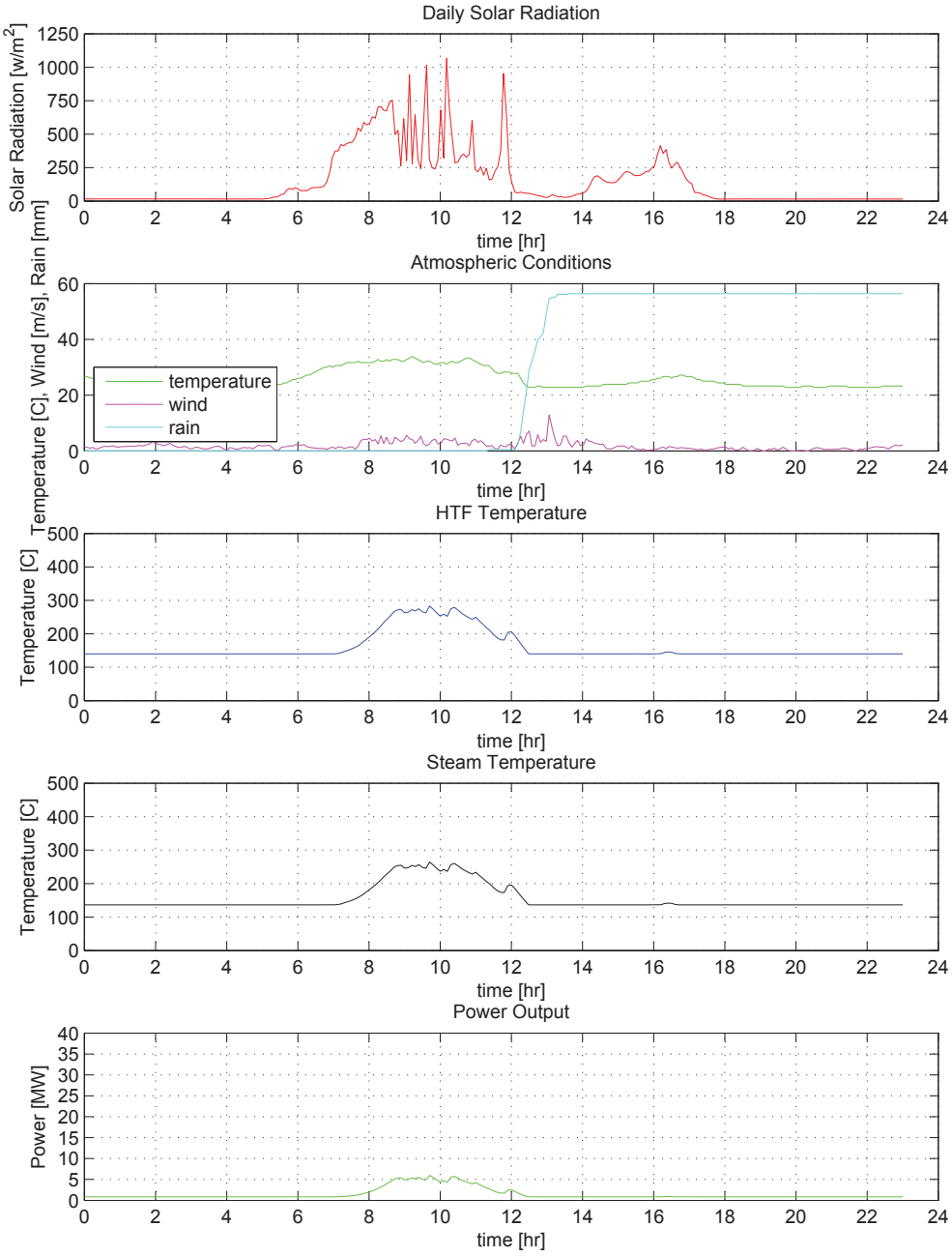

Figure 8.11: Measured Solar Radiation, Ambient Temperature, Wind Velocity, Precipitation, HTF Temperature, Steam Temperature and Power Output for July 1, 2003

As can be seen from the plotted results, the fairer and clearer the day (March 20, 2002 and June 26, 2003), the more solar radiation is obtained and an optimal system performance is observed. When there are solar transients due to clouds, it can be seen that the system has some drops in overall system temperature and thus, in power output. If these transients occur for brief periods of time, e.g., 5 to 10 minute intervals (October 24, 2002), the system is able to return to steady power production once solar radiation is restored.

If these solar transients are prolonged for lengthy periods, e.g., an hour or two, (January 28, 2003) then system performance is greatly reduced and the system may not recover. However, if there are solar transients due to prolonged periods of rain, as can be observed on July 1, 2003, the system produces an almost zero power output once it starts raining.

Juana Díaz, a municipality that lies in the south of Puerto Rico, had a population of around 50,531 and 16,490 houses for 2000, according to the 2000 Census. This indicates that Juana Díaz has 1.33% of the total population (3,808,610) and 1.31% of the total households (1,261,325) in the island. With this data, an estimated system electricity production of 54.2 M kWh per year and the island's net electricity consumption of 22.3 B kWh for 2003, the average household consumption can be estimated in 17,649 kWh per year.

Further analysis indicates that the estimated electricity production for the system would be 0.24% of the island's net electricity consumption, meaning that it could power up 18.6% of the households in Juana Díaz, or around 3,000 homes.

Using the power output obtained from the simulation model, and the component costs from SunLab, overall system costs were estimated. Analysis with the SunLab data for 2004, 2007, and 2010 are presented in Tables 8.3, 8.4 and 8.5 respectively.

Table 8.3: Summary of costs using the 2004 forecast data from SunLabb

Summary of Costs 2004:		
Support Structure Cost	$61	/m^2
Total Support Structure Cost	$36,273,208	
Heat Collection Elements Cost	$43	/m^2 field
Total Receiver Cost	$25,569,638	
Mirror Cost	43	/m^2
Reflector Area	49.6	m^2/collector
Collectors	12000	
Total Cost	$25,569,638	
Power Block & Balance of Plant Cost	$581	/kWe
Capacity	30000	kWe
Total Cost	$17,430,000	
Miscellaneous Cost		
Total Cost	$27,971,995	
Land	$20,000	/acre
Total	$2,792,772	
Solar Collection System		
Cost	234	/m^2
Aperture Area	219456	m^2
Total Cost	$51,352,704	
TOTAL	$186,959,955	
$/kWe	$18,696.00	
O&M Cost	0.0228	/kWhe
Annual Production	54,232	MWhe
Total Annual O&M Cost	$1,236,490	

Table 8.4: Summary of costs using the 2007 forecast data from SunLab

Summary of Costs 2007:		
Support Structure Cost	$57	/m^2
Total Support Structure Cost	$33,894,637	
Heat Collection Elements Cost	$34	/m^2 field
Total Receiver Cost	$20,217,853	
Mirror Cost	36	/m^2
Reflector Area	49.6	m^2/collector
Collectors	12000	
Total Cost	$21,407,139	
Power Block & Balance of Plant Cost	$581	/kWe
Capacity	30000	kWe
Total Cost	$17,430,000	
Miscellaneous Cost		
Total Cost	$24,166,281	
Land Cost	$20,000	/acre
Total	$2,792,772	
Solar Collection System		
Cost	234	/m^2
Aperture Area	219456	m^2
Total Cost	$51,352,704	
TOTAL	$171,261,386	
$/kWe	$5,708.71	
O&M Cost	0.0171	/kWhe
Annual Production	54,232	MWhe
Total Annual O&M Cost	$927,367	

Table 8.5: Summary of costs using the 2010 forecast data from SunLab

Summary of Costs 2010:		
Support Structure Cost	$54	/m^2
Total Support Structure Cost	$32,110,708	
Heat Collection Elements Cost	$28	/m^2 field
Total Receiver Cost	$16,649,997	
Mirror Cost	28	/m^2
Reflector Area	49.6	m^2/collector
Collectors	12000	
Total Cost	$16,649,997	
Power Block & Balance of Plant Cost	$525	/kWe
Capacity	30000	kWe
Total Cost	$15,750,000	
Miscellaneous Cost		
Total Cost	$20,931,425	
Land Cost	$20,000	/acre
Total	$2,792,772	
Solar Collection System		
Cost	161	/m^2
Aperture Area	219456	m^2
Total Cost	$35,332,416	
TOTAL	$140,217,315	
$/kWe	$4,673.91	
O&M Cost	0.0135	/kWhe
Annual Production	99,761.1	MWhe
Total Annual O&M Cost	$732,132	

After having obtained an estimated system cost and electricity production, a levelized electricity cost analysis is performed. The analysis was conducted assuming a life of **30 years** and interest rates of **8%**, **5%** and **3%**. The results are presented below.

Table 8.6: Levelized Electricity Cost Analysis

		2004	
Rate	8%	5%	3%
O\&M PV	$13,920,132	$19,007,876	$24,235,742
System Cost PV	$200,880,087	$205,967,830	$211,195,696
cents/kWhe	12.35	12.66	12.98
		2007	
Rate	8%	5%	3%
O\&M PV	$10,440,099	$14,255,907	$18,176,806
System Cost PV	$181,701,485	$185,517,293	$189,438,192
cents/kWhe	11.17	11.40	11.64
		2010	
Rate	8%	5%	3%
O\&M PV	$8,242,183	$11,254,663	$14,350,110
System Cost PV	$148,459,498	$151,471,978	$154,567,425
cents/kWhe	9.12	9.31	9.50

The calculated LECs range from **9.12 to 12.98 cents per kilowatt-hour**. Even though it would make sense to study the LECs resulting from the 2010 data, it is important to acknowledge that these were published in 2004 with the assumption that these "cost estimates would follow the industry expectations for research and development advances in component and subsystem improvements" [31]. The study also assumes that the U.S. trough industry was going to pursue a commercialization plan, favoring implementation of SEGS-type plants in the near-term. At this point in time, 2010, this implementation has not occurred. The 2004 data is thought to be the most accurate one in terms of system cost since it was based on actual data; the 2007 and 2010 values were based on forecasted system costs.

Chapter 9

CONCLUSIONS AND FUTURE WORK

This thesis has presented an innovative approach to electricity production by solar means. All the pertinent optical and thermal analysis for a CPC collector was approached, as well as, an energy balance and Rankine cycle analysis to determine the plant's energy output. The steady-state analysis determined that at first glance, a solar thermal power plant could be **viable** for Puerto Rico, but there is much study to be done.

One of the main challenges a solar system faces is the **ability to dispatch electric power**. This can be effectively solved by introducing a **Thermal Energy Storage system**, or any sort of **hybridization** for that matter. The fact that the system could be 'over' designed to operate for long hours after sunset is a viable alternative to the intermittence of the solar resource. An oversized storage system can be a considerable cost, but it allows for true dispatchability and a higher system capacity factor. It also reduces the cost per kilowatt-hour of the system accounting for the system's lifetime.

As could be seen on Chapter 8, during transient solar conditions, a TES system would not be a viable alternative in P.R. If there is not enough radiation for power production, there neither would be enough thermal energy available for storage. Taking into consideration local atmospheric conditions, fossil fuel hybridization would certainly be the most economic and effective means of attending solar transients.

As was seen, data is available in monthly and hourly averages, both providing insight in system performance. However, using monthly averages**using average values** greatly simplifies computations and complexity, but gives a **vague overall system performance**. Transient solar data, on the other hand, gives the opportunity to study system performance since it relies on real-time behavior. It can provide a means of: introducing control systems for monitoring and adjusting system parameters, and for analyzing TES or hybridization systems more accurately, since there is a more precise knowledge of thermal energy input to the system.

The simulation results showed that transient periods of 5-10 minutes pose no real threat to system performance. However, if there are transient periods of heavy cloud cover or rain lasting longer than an hour or so, system performance is greatly reduced. Unfortunately, these conditions are somewhat normal for almost all of P.R.

In terms of the calculated LEC, the STPP does not seem viable since it is higher than the avoided energy costs the Puerto Rico Energy Power Authority claim they have. The results: around **9.12 - 12.98 cents per kilowatt-hour**. This, however, does not pose a guarantee of the system power output. The LEC is based solely on the present value of the capital system cost and the expected energy output throughout its lifetime. The parabolic trough plant LEC was around **9.9 - 10.3 cents per kilowatt-hour in**

2004 and was expected to be around **6.8 - 7.6 cents per kilowatt-hour in 2007**.

In terms of the optic and the collector performance analysis, the study shows the suitability of a CPC trough for electricity generation in the same way that a Parabolic Trough is used. Since Puerto Rico lies on a tropical region, the level of diffuse radiation is rather high and the fact that the CPC (unlike parabolic troughs) can utilize this type of radiation greatly improves system efficiency and utilization.

This study foresaw the production of steam in the collector field for Direct Steam Generation, but solar salt was used as HTF instead because research is still underway to determine the best ways to store energy for Direct Steam Generation (DSG) Solar Thermal Power Plants. It is said that if a DSG system could be successfully implemented, higher operating temperatures could be achieved, and the system costs could be reduced significantly.

Even though solar energy seems like a somewhat expensive and technically challenging means of electricity production, it could help alleviate the energy crisis Puerto Rico is facing, if implemented effectively. Tariffs for Summer 2008 showed an all-time record high of around **30 cents per kilowatt-hour** charged to consumers. And with the sky-rocketing prices of crude oil, this tendency in higher tariffs will continue into the future.

Even though a high risk investment of an average of **$180 M for a 30 MW** solar power plant may seem far fetched, it will certainly give the opportunity for this and other systems of this type to provide a means of reducing Puerto Rico's dependency on foreign oil. Not to mention the savings, in fuel and in greenhouse gasses not

entering the atmosphere, which a Solar Thermal Power Plant can provide. Since the island does not have any noteworthy fossil fuel energy resources, billions of dollars leave the island for the purchase of crude every year. Part of this hefty sum of money could very well stay here and be used for **developing a 'Solar Industry'** in the island, generating several hundreds, if not thousands of new job and business opportunities in the renewable solar energy field.

There is not enough determination in Puerto Rico (and the world) to pursue a more renewable future. Puerto Rico's installed capacity for producing electricity is around **5.3 GW**, which means that a **30 MW solar plant** would only represent a merely **0.57% of the island's installed capacity**. It is quite obvious that, at this point in time and with the available technological resources, there is no way renewable energy systems could provide us with the energy independence we seek. Puerto Rico needs a complete restructure of the AEE that will give way to a more truly diversified electric system, at a fraction of the actual cost to the consumer.

Aside from wind, solar and ocean, there are several other viable alternatives that could minimize our dependence on depleting fossil fuels. Nuclear energy is another renewable energy source that could certainly help alleviate this dependence. Nuclear has a LEC of around **3.08 - 3.61 cents per kilowatt-hour** [59] and also has the ability of supplying essential base-load capacity, which can not be achieved by other renewable energy sources.

After having performed this study, it can be concluded that it required extensive knowledge from different engineering disciplines. Due to this fact, each analysis module (Optical Analysis, Thermal Analysis, Energy Balance, HX Design, Thermal Energy

Storage System Design, Power Block Analysis, Pressure Drop Calculations as well as other Fluid Mechanics aspects) was not conducted in much detail. This type of project could have easily been divided by discipline area and developed in stages by several students, perhaps, as a capstone course. Students and Professors from Mechanical Engineering can obviously make a greater contribution, along with Optical Physics and Materials Engineering students and Professors. The greatest difficulty in developing this investigation lies in the fact that there is just not enough information out there. There are only a couple of facilities that study and develop this type of system and they are not willing to give out information. Several attempts proved unsuccessful when trying to get technical data, material properties, system costs, etc. After receiving help from people like: Dr. Félix E. Fernández from Optics in the Physics Department, Dr. Gustavo Gutiérrez from INME in the Heat Transfer area, and Dr. Fernando Plá from INME in the Solar Thermal and Fluid Dynamics area, the real feat was to be able to combine all these disciplines in unison to design this system, at least theoretically.

There are however many aspects that were either not considered or others that can be improved in future related works. Recommendations for future works include but are not limited to:

- **Collect and process additional solar data**. The solar data used in this study has only been collected for the past 5 years or so. A reliable solar radiation measuring system should be built in Puerto Rico. There are several potential areas that seem to be suitable candidates for harboring solar thermal power plants, but are not taken into consideration due to the fact that there is no solar data available for the regions, whatsoever.

- **Use daily solar data measured in 10 to 15 minute intervals, instead of working with average monthly values for a particular hour**. This will

greatly enhance the calculated electrical power output and introduce a highly dynamic variable into the analysis.

- **Acquire TRANSYS**. This software, which is provided for educational use, is capable of incorporating each and every component encountered in solar thermal systems (e.g., collectors, absorbers, piping, pumps, etc.). It also provides a means for the user to input solar data specific for the region. The purchase of this software, and getting knowledgeable people to work with it, will be indispensable for performing complete and thorough system analyses in the near future.

- **Study in greater details the heat transfer mechanisms taking place** in a Solar Thermal Power Plant for reducing thermal losses that ultimately lead to higher system costs.

- **Consider losses from** the **piping** system **and** the **parasitic** electrical losses in the system.

- **Study the effects of wind** incident on the collector array. These systems are designed to withstand wind speeds of up to 80 mph. This is not a serious problem in the Mojave Desert in California, since they do not have any hurricanes. In Puerto Rico, it can be of interest.

- **Study the effect the plant power output has on the Levelized Electricity Cost**. Studies show that the higher the power output, the more opportunities for economies of scales. This could result in lower LECs.

- **Implement control systems to the simulation model**. This way, Thermal Energy Storage and/or hybridization can be included in the simulation model. This would enhance overall system performance and lead to a higher capacity factor.

- **Study the possibility of constructing a metamodel for the system**. This was approached during the investigation. Neither linear regression nor other non-linear curves provided a good fit to the simulation data obtained. A metamodel could be very useful, since it is basically a mathematical model (or equation) that can characterize the system and give insights on its input(s) and output(s), without having to run the simulation model. This may be achieved in the future by carefully studying the data available and studying any pattern in it, or by using custom equations that can describe the data better and provide a good metamodel.

- And last but certainly not least, **implement a couple of collector rows for verifying** if the **theoretical feasibility** of this type of system holds true in real life. This will provide with the means of measuring real-time system data. Measurements such as: pressures and pressure drops, temperatures and temperature differences, solar radiation and efficiencies, just to name a few. These could be measured and help confirm the viability of this type of project. The power block and the TES system components will not be necessary.

This investigation was conducted with the hope that it could, in the future, provide a means to consider the implementation of this type of system in Puerto Rico, at least experimentally. Sadly, the results did not prove to be too favorable for the development of a STPP in Puerto Rico. Even though there are numerous places in the world were this type of system is very suitable, Puerto Rico is not one of them, in terms of the available resource and financial feasibility. We may have to keep looking for renewable means of producing energy other than solar thermal. However, this could change if federal and/or local incentives or credits are issued that could provide for the implementation of this type of system in Puerto Rico.

Bibliography

[1] NOAA. Puerto Rico Cummulative Rainfall Map.

[2] Y.A. Çengel, R.H. Turner, and J.M. Cimbala. *Fundamentals of Thermal Fluid Sciences*. Mc Graw-Hill, 2008.

[3] D. Kearney, B. Kelly, U. Herrmann, R. Cable, J. Pacheco, R. Mahoney, H. Price, D. Blake, P. Nava, and N. Potrovitza. Engineering aspects of a molten salt heat transfer fluid in a trough solar field. *Energy*, 29:861–870, 2004.

[4] Engineering Toolbox. Roughness and surface coefficients of ventilation ducts. http://www.engineeringtoolbox.com/surface-roughness-ventilation-ducts-d-209.html.

[5] W.B. Stine and R.W. Harrigan. *Solar Energy Systems Design*. John Wiley and Sons, 1985.

[6] M. Peel, B. Finlayson, and T. McMahon. Updated world map of the Köppen-Geiger climate classification. *Hydrol. Earth Syst. Sci.*, 2007.

[7] A.M. López and K.G. Soderstrom. Insolation in Puerto Rico. *Journal of Solar Energy Engineering*, 1983.

[8] FLABEG Solar Int., Workshop on Thermal Storage for Trough Power Systems. *Overview on Thermal Storage Systems*, 2002.

[9]

[10] J. Duffie and W. Beckman. *Solar Engineering of Thermal Processes*. John Wiley and Sons, 2006.

[11] National Renewable Energy Laboratory. *User's Manual National Solar Radiation Data Base 1961-1990*. NREL, 2002.

[12] D.Y. Goswami, F. Kreith, and J.F. Kreider. *Principles of Solar Engineering*. Taylor and Francis Group, 2000.

[13] M. Carter and J.B. Elsner. Monthly rainfall climatology for Puerto Rico. Technical report, CITM, Florida State University, 1997.

[14] A.N. Strahler and A.H. Strahler. *Elements of Physical Geography*. John Wiley and Sons, 1984.

[15] C. Beck, J. Grieser, M. Kottek, F. Rubel, and B. Rudolf. 2006: Characterizing global climate change by means of Köppen Climate Classification. *Klimastatusbericht*, pages 139–149, 2005.

[16] M. Collares-Pereira and A. Rabl. The average distribution of solar radiation correlations between diffuse and hemispherical and between daily and hourly insolation values. *Solar Energy*, 22:155–164, 1979.

[17] Institute of Tropical Forestry, U.S. Department of Agriculture, Puerto Rico. *Weather in the Luquillo Mountains of Puerto Rico*, 1966.

[18] D. T. Sandwell. Biharmonic spline interpolation of geos-3 and seasat altimeter data. *Geophysical Research Letters*, 14:139–142, 1987.

[19] P. Gleckman, J. O'Gallagher, and R. Winston. Concentration of sunlight to solar-surface levels using non-imaging optics. *Nature*, 339(198-200), 1989.

[20] R. Winston. Light collection within the framework of geometrical optic. *J. Opt. Soc. Am.*, 60:245, 1970.

[21] C. Kennedy, K. Terwilliger, and A. Warrick. Optical durability of candidate solar reflector materials. *Journal of Solar Energy Engineering*, 127:262–269, 2004.

[22] C.F. Kutscher, R.L. Davenport, D.A. Dougherty, R.C. Gee, P.M. Masterson, and E. Kenneth. Design approaches for solar industrial process heat systems. *Solar Energy Research Institute*, 1982.

[23] NREL, Parabolic Trough Workshop. *Parabolic Trough Collector Overview*, 2007.

[24] NREL, International Solar Energy Conference. *A Parabolic Trough Solar Power Plant Simulation Model*, 2003.

[25] NREL, Intersociety Energy Conversion Engineering Conference Canada. *Solar Two Performance Evaluation*, 1999.

[26] NREL. *Next Generation Receivers*, 2006.

[27] NREL Parabolic Trough Workshop. *Overview on Direct Steam Generation (DSG) and Experience at the Plataforma Solar de Almería (PSA)*, 2007.

[28] Germany ASME Solar Energy: The Power to Choose. *EuroTrough - Design Issues and Prototype Testing at PSA*, 2001.

[29] NREL Parabolic Trough Thermal Energy Storage Workshop. *Overview on use of a Molten Salt HTF in a Trough Solar Field*, 2003.

[30] NREL. *Engineering Evaluation of a Molten Salt HTF in a Parabolic Trough Solar Field*, 2004.

[31] NREL. *Assessment of Parabolic Trough and Power Tower Solar Technology Cost and Performance Forecasts*, 2003.

[32] W. Duff. A methodology for selecting optimal components for solar thermal energy systems: Application to power generation. *Solar Energy*, 17:245–254, 1975.

[33] F. Incropera and D. DeWitt. *Introduction to Heat Transfer*. Wiley and Sons, 2002.

[34] F.P. Incropera and D.P. DeWitt. *Fundamentals of Heat and Mass Transfer*. John Wiley and Sons, 2002.

[35] Y.A. Çengel. *Introduction to Thermodynamics and Heat Transfer*. McGraw-Hill, 1997.

[36] R.F. Boehm. *Design Analysis of Thermal Systems*. John Wiley and Sons, 1987.

[37] L.F. Drbal. *Power Plant Engineering*. Kluwer Academic Publishers, 2001.

[38] NREL. *Direct Solar Steam in Parabolic Troughs Simulation of Dynamic Behaviour*, 2004.

[39] S.D. Odeh, G. L. Morrison, and M. Behnia. Modelling of parabolic trough direct steam generation solar collectors. *Solar Energy*, 62:395–406, 1998.

[40] Sandia National Laboratories. *10 MW, Solar Thermal Central Receiver Pilot Plant: Thermal Storage Subsystem Evaluation - Final Report*, 1986.

[41] U. Herrman, B. Kelly, and H Price. Two-tank molten salt storage for parabolic trough solar power plants. *Energy*, 29:883–893, 2004.

[42] Solar Energy Research Institute. *Phase-Change Thermal Energy Storage*, 1988.

[43] M.A. Hamdan and F.A. Elwerr. Thermal energy storage using a phase change material. *Solar Energy*, 56:183–189, 1996.

[44] A. Sharma, V.V. Tyagi, C.R. Chen, and D. Buddhi. Review on thermal energy storage with phase change materials and applications. *Renewable and Sustainable Energy Reviews*, 13:318–345, 2009.

[45] A. Karaipekli and A. Sari. Capricmyristic acid/expanded perlite composite as form-stable phase change material for latent heat thermal energy storage. *Renewable Energy*, 33:2599–2605, 2008.

[46] A. Shukla, D. Buddhi, and R.L. Sawhney. Thermal cycling test of few selected inorganic and organic phase change materials. *Renewable Energy*, 33:2606–2614, 2008.

[47] A. Rabl. Optical and thermal properties of compound parabolic concentrators. *Solar Energy*, 18:497–511, 1976.

[48] A. Rabl, J. OGallagher, and R. Winston. Design and test of non-evacuated solar collectors with compound parabolic concentrators. *Solar Energy*, 25:335–351, 1980.

[49] P.C. Eames and B. Norton. Detailed parametric analyses of heat transfer in cpc solar energy collectors. *Solar Energy*, 50:321–338, 1993.

[50] M. Collares-Pereira and A. Rabl. Simple procedure for predicting long term average performance of non-concentrating and of concentrating collectors. *Solar Energy*, 23:235–253, 1979.

[51] W. Yu, D.M. France, M.W. Wambsganss, and J.R. Hull. Two-phase pressure drop, boiling heat transfer, and critical heat flux to water in a small-diameter horizontal tube. *International Journal of Multiphase Flow*, 28:927–941, 2002.

[52] M. McDowell. Solar power tower technology large scale storable and dispatchable solar energy. http://cohesion.rice.edu/CentersAndInst/CNST/emplibrary/McDowell.pdf.

[53] R. Winston. Principles of cylindrical concentrators for solar energy. *Solar Energy*, 17:255–258, 1975.

[54] A. Rabl and R. Winston. Ideal concentrators for finite sources and restricted exit angles. *Applied Optics*, 15:2880–2883, 1976.

[55] A. Rabl. Practical design considerations for cpc solar collectors. *Solar Energy*, 22:373–381, 1979.

[56] A. Rabl. Solar concentrators with maximal concentration for cylindrical absorbers. *Applied Optics*, 15:1871–1873, 1976.

[57] A. Rabl. Yearly average performance of the principal solar collector types. *Solar Energy*, 27:215–233, 1981.

[58] NREL. *Nontechnical Barriers to Solar Energy Use: Review of Recent Literature*, 2006.

[59] International Congress on Advances in Nuclear Power Plants. *Economic Analysis of the Levelized Cost of Electricity Generation*, 2006.

[60] The World Bank. *Cost Reduction Study for Solar Thermal Power Plants*, 1999.

[61] M. Eck and T Hirsch. Dynamics and control of parabolic trough collector loops with direct steam generation. *Solar Energy*, 81:268–279, 2007.

[62] H.J. Hou, Z.F Wang, R.Z. Wang, and P.M. Wang. A new method for the measurement of solar collector time constant. *Renewable Energy*, 30:855–865, 2005.

[63] Y. Kim and T. Seo. Thermal performances comparisons of the glass evacuated tube solar collectors with shapes of absorber tube. *Renewable Energy*, 32:772–795, 2007.

[64] P. Valera, A. Esteban, M. de los Reyes Carrillo, R Osuna, P. Menna, R. Gambi, P. Helm, M. Grottke, M. Geyer, F. Dobon, J. Monedero, A. Lugo, M. Romero, F. Chenlo, M. Alonso, M. Sanchez, J. Artigas, and A. Fresneda. Solar energy: Comparative analysis of solar technologies for electricity production. *Proceedings of 3rd World Conference on Photovoltaic Energy Conversion*, 3:2482–2485, 2003.

[65] Proceedings of Solar Forum 2001, Solar Energy: The Power to Choose. *TRNSYS Modeling of the SEGS VI Parabolic Trough Solar Electric Generating System*, 2001.

[66] Conference Record of the 2006 IEEE 4th World Conference on Photovoltaic Energy Conversion. *Energy Performance Modelling of Stationary and Quasi-Stationary Solar Concentrators Based on Reverse Ray-Tracing Photovoltaic Energy Conversion*, 2006.

[67] T.A. Stuetzle. Automatic Control of the 30 MWe SEGS VI Parabolic Trough Plant. Master's thesis, University of Wisconsin-Madison, 2002.

[68] M. Holmgren. Xsteam for matlab, water and steam properties according to IAPWS IF-97. http://www.x-eng.com.

[69] A.M. Patnode. Simulation and performance evaluation of parabolic trough solar power plants. Master's thesis, University of Wisconsin-Madison, 2006.

[70] Solar collector test report. Technical report, EnerWorks Inc., 2006.

[71] M.J. Brooks, I. Mills, and T.M. Harms. Performance of a parabolic trough solar collector. *Journal of Energy in Southern Africa*, 2006.